UNIVERSITÀ DEGLI STUDI DI CATANIA

DOTTORATO DI RICERCA IN INGEGNERIA FISICA

SEBASTIANA MARIA REGINA PUGLIA

The resonant cross sections of ^{10,11}B(p,α) reactions at astrophysical energies: indirect measurements via the THM

Coordinatore del corso:

Prof. G. Giaquinta

Tutor:

Prof. C. Spitaleri

TESI PER IL CONSEGUIMENTO DEL TITOLO

XXIII CICLO

Per quello che eri,
che sei
e che sarai sempre.
A mio nonno Gaetano.

Contents

Introduction

Over the last 50 years powerful telescopes have enormously extended our view of the Universe, unveiling a wealth of detailed information on a variety of objects, from the oldest stars, which were formed shortly after the big bang, very distant galaxies and globular clusters, to pulsars, black holes and supernova explosions. Although some of the observed phenomena remain mysterious and new phenomena continue to appear, the apparent chaos in the Universe can be resolved into some other ways; it seems that an answer to many questions can be found combining astrophysics and nuclear physics, that merge in the so called nuclear astrophysics.

Many processes and objects in the astrophysical scenario that astrophysics tries to understand are physically inaccessible. Thus, it is important that at least some aspects, e.g. the nuclear ones, are rather well understood. Nuclear astrophysics is the branch of astrophysics which helps in understanding the Universe through the knowledge of the microcosm of the atomic nucleus. One of the most important aspect is represented by the nuclear fusion reactions, which are at the heart of nuclear astrophysics and can be studied in the laboratory. They influence sensitively the energy output and evolutionary timescale of the various stellar object in the nucleosynthesis of the elements in the earliest stages of the Universe and in all the objects formed thereafter. They further control the associated neutrino luminosity and evolution of stars. A good knowledge of the rates of these fusion reactions is thus essential for understanding this broad picture. Among the scenarios studied by nuclear astrophysics great interest is given to the issue of light elements. In fact, in the last years big efforts have been devoted to the study of the light elements abundances, whose importance is strongly related to cosmology as well as to stellar structure and evolution.

Two main processes are involved in the formation of light elements: the primordial nucleosynthesis BBN responsible to the production of D, ^{3}He, ^{4}He and ^{7}Li, and spallation reaction of galactic cosmic ray (GCR) for ^{6}Li, ^{9}Be, ^{10}B and ^{11}B, whereas ^{7}Li can be produced in the stellar nucleosynthesis as well. Big Bang nucleosynthesis probes the Universe to the earliest times, from a fraction of second to hundreds of seconds. Standard Big Bang model has the very powerful feature that the prediction for the light elements production is primarily dependent on one free parameter, the baryon-to-photon ratio η (that is connected to the baryon density of the Universe), this parameter corresponds to the temperature and density of the early universe and allows one to determine the conditions under which nuclear fusion occurs. According to the standard Big Bang model [Malaney & Mathews (1993)] for T$\leq 10^{9}$K it is possible the formation of light nuclei (D, ^{3}He, ^{4}He and ^{7}Li) from the starting chemical species, protons and neutrons. The absence of stable nuclei with A=5 or A=8, together with the increasing of Coulomb barrier for reactions between heavier nuclei substantially stops the cosmological production in correspondence of ^{7}Li in Standard Big Bang Nucleosynthesis.

In order to explain the formation of LiBeB, fifty years ago Burbidge, Fowler and Hoyle [Burbridge *et al.* (1957)] addressed this problem by proposing "x-proces", where 'x' was for 'unknown', responsible for the synthesis of these light elements. In fact, if we consider the solar system abundance curve, LiBeB are extremely underabundant in comparison to their neighbors elements in the periodic table; these low abundances are related to the fragility of these elements in typical stellar burning conditions. It was consequently soon recognized that even the very small quantities of LiBeB present in solar system material could not be produced in stellar nucleosynthesis. Afterwards this x-process, Reeves *et al.* (1970) proposed a spallation scenario for the production of the light elements. The basic process is that high-energy ($\sim$ 150 MeV) protons and neutrons bombarded interstellar nuclei of C,N and O creating lighter isotopes. The cosmic-ray origin of most ^{7}Li and ^{11}B, and essentially all of ^{6}Li ^{9}Be and ^{10}B is nowadays the widely accepted standard scenario. Part of ^{7}Li is produced in stellar environments, while ^{11}B may have a component produced in supernova explosion by neutrino spallation of ^{12}C [Kiener (2009)]. This scenario can reasonably account for the above mentioned elemental and isotopic ratios with our present knowledge

of cosmic-ray propagation in the Galaxy and of the nuclear reactions responsible for LiBeB production and destruction. Besides the importance of these elements for the understanding of primordial nucleosynthesis and spallation processes on the interstellar medium, the study of light elements abundances offers a special opportunity in the understanding of internal stellar structure and mixing mechanism acting in stellar interior. In fact, Li, Be and B abundances can all be used as probes to understand surface mixing down to temperature of about 2.5×10^6 K, 3.5×10^6 K, and 5×10^6 K respectively, where they are destroyed mainly through (p,α) reaction [Stephens *et al.* (1997)]. The degree to which Li, Be and B are depleted from a stellar atmosphere serves as a subtle tracer of internal stellar kinematics.

In last years, there have been several different studies of the light element [Stephens *et al.* (1997), [Boesgaard *et al.* (2004a), [Boesgaard *et al.* (2004b)] in young F and G stars in order to give useful information about mixing processes. Although most previous studies have concentrated on Li alone, because each element survives to a different depth, much more powerful model constraints can be derived when more than one element is considered simultaneously [Deliyannis *et al.* (1995)]. From recent observation it is shown that in F and G stars an evident Li and Be depletion is observed, whereas the B abundance seems almost constant. To explain these behavior several theoretical models have been proposed, these include mass loss [Schramm *et al.* (1990)], microscopic diffusion [Michaud *et al.* (1986)] and various form of slow mixing [Stephens *et al.* (1997), Pinsonneault *et al.* (1990)]. The current observational status is well described if one considers non-standard mixing process induced by stellar rotation [Stephens *et al.* (1997), Boesgaard *et al.* (2005)]. However, due to this process LiBeB are transported into the region where they are mainly destroyed through (p,α) reaction induced at the temperature of the order of 10^6 K, which corresponds to the Gamow energy E_G of a few keV's.

The Gamow energy window are much lower than the Coulomb barrier ($\sim$ MeV) characterizing charged particle induced reactions, thus cross sections exponentially drop in the sub-Coulomb region, making their very difficult. In addition, the electron screening effect, due to the electrons surrounding the interacting ions, prevents one to measure the bare-nucleus cross section. Up to date the only way

to get the ultra-low energy region bare nucleus cross section is by extrapolating the behavior of the higher energy data. This is done by means of the definition of the astrophysical S(E)-factor, which represents essentially the cross section free of Coulomb suppression:

$$S(E) = \sigma(E)Eexp(2\pi\eta) \tag{1}$$

where $\exp(2\pi\eta)$ is the inverse of the Gamow factor, which removes the dominant energy dependence of σ(E) due to the barrier penetrability. Although the S(E)-factor allows for an easier extrapolation, large errors may be introduced due to, for instance, the presence of unexpected resonances or high energy tails of subthreshold resonances. Thus, a number of indirect methods (such as Coulomb Dissociation [Baur & Rebel (1994)], Asymptotic Normalization Coefficient (ANC) [Mukhamedzanov & Tribble (1999)], and Trojan Horse Method (THM) [Baur *et al.* (1986),Cherubini *et al.* (1996), Spitaleri *et al.* (1999)]) have been introduced as alternative approaches for determining the bare-nucleus S(E)-factor. They make use of direct reaction mechanisms, such as transfer processes (stripping and pick-up) and quasi-free reactions respectively. In particular the THM has been successfully applied several times to rearrangement reaction connected with fundamental astrophysical problems [Baur *et al.* (1986), Cherubini *et al.* (1996), Spitaleri *et al.* (1999), Spitaleri *et al.* (2001)]. The method has proven to be particularly suited for extracting low-energy cross section for nuclear reaction having charged particle (or neutron) in the exit channel.

The idea of the THM is to extract the cross section of an astrophysically relevant two-body reaction $A+x\rightarrow\ c+C$, from the quasi-free contribution of a suitable three-body reaction $A+a\rightarrow c+C+s$ where a has a strong $x\oplus s$ cluster structure. Under proper kinematical condition, the particle A interacts only with the cluster x (participant) of the target nucleus a, whereas the cluster s behaves as a spectator to the two-body process. In order to completely determine the kinematical properties of the spectator s, the two ejectiles c and C have to be detected, identified and their energies and angles of emission measured. Since the energy in the entrance channel is higher than the Coulomb barrier between the interacting nuclei, Coulomb suppression and electron screening do not affect the extracted cross section.

The deduced two-body reaction cross section σ^N(E) represents the nuclear part alone, and its absolute value is obtained by normalization to the direct data at energies above the Coulomb barrier. In order to compare the two data sets, it is necessary to correct the σ^N(E) for the penetration function through the Coulomb barrier. The obtained energy dependence should be identical to that derived from direct measurements, except at low energies where their behavior should differ due to the effects of the electron screening on the direct cross section or the above defined astrophysical S(E)-factor. Moreover the THM allows us to obtain an estimation of the screening potential U_e by comparing the bare-nucleus S(E)-factor with the direct screened one at low energies. Thus, THM has to be regarded as a complementary tool in experimental nuclear astrophysics. In the present work the experimental study of the ^{10}B(p,α)^{7}Be and the ^{11}B(p,α)^{8}Be reactions via the THM is reported. The two reactions are the main responsible for Boron destruction in stellar environment.

In particular, the indirect study of the ^{10}B(p,α)^{7}Be is described in chapter 4. The aim of the experiment was to study the astrophysical relevant energy region for the two-body reaction through the THM applied to the ^{2}H(^{10}B,α^7Be)n three-body reaction. The "hot-spot" for the study of this reaction is the presence of the E_x=8.701 MeV ^{11}C resonant level (J=5/2$^+$) at about E_{cm}(^{10}B-p)=10 keV that corresponds to the Gamow peak for this reaction. The experiment was performed at the Laboratori Nazionali del Sud in Catania where the Tandem Van de Graaf accelerator provided at 24.4 MeV ^{10}B beam. All the steps of the data analysis performed through the THM are given in the text. The astrophysical S(E)-factor are deduced in the energy region of interest, just in correspondence of the Gamow peak for this reaction. The results are compared with those from literature [Angulo *et al.* (1993)] that reports only an extrapolation in such energy region. A good agreement shows up between the direct and indirect S(E)-factor in the region where direct data are available, whereas at lower energies, below 20 keV, the THM S-factor confirm the extrapolated from direct data.

In chapter 5 the study of ^{2}H(^{11}B,α^8Be)n three-body reaction to extract the cross section of the ^{11}B(p,α)^{8}Be binary process, is reported. The same analysis procedure shown in the previous chapter is adopted, but in this case the discrimination between two reaction channels which refer to α-particles coming from ^{8}Be

decay in its ground state (α_0) and from its first excited state (α_1) was needed. The S(E)-factor has been extracted and compared with direct data present in literature [Becker *et al.* (1987)], showing also in this case a good agreement. Finally in the last chapter the main conclusion of the present thesis are discussed.

Chapter 1

The light element in the Universe

1.1 The origin of the light elements

The study of the origin of the light element in the Universe begins when in the 1946 George Gamow and his collaborators considered the possibility that all chemical elements might be generated by a long chain of neutron captures in the cooling primordial Universe, but the absence of stable nuclei with mass 5 and 8 constituted a fatal flaw of this scheme. After, in 1957 Hoyle and Burbidge [Burbridge *et al.* (1957)] proposed the idea of a stellar origin for the chemical elements. While their idea was correct for the heavy nuclei, from Carbon to Uranium, it ran into difficulty in accounting for the lighter nuclei, due to their short lifetimes in stellar interior. So other processes were required to explain the formation of the lighter element [Reeves (1994)]. A necessary condition was to find a process in which these nuclei do not remain at high temperature for any length of time, comparable to the time of stellar destruction for this elements ($\sim 10^6$yr).

These processes, are divided mainly into two fundamental, the primordial nucleosynthesis BBN only for D, ^{3}He, ^{4}He, and ^{7}Li, and spallation reactions of galactic cosmic rays (GCR) for ^{6}Li, ^{9}Be, ^{10}B, ^{11}B. It is important, also to remember another source for ^{7}Li, i.e. the synthesis in stars. In fact the observation that there is a class of lithium-rich supergiants shows the stellar processes may be responsible as was suggested by [Cameron & Fowler (1971)], in two stellar sites: during nova explosions and in the envelopes of massive asymptotic giant

branch (AGB) stars. Moreover another theory has been developed to explain the production of light nuclei. It is possible that a potentially interesting source of ^{7}Li and ^{11}B is the ν-process Type II supernovae [Woosley (1990), Timmes *et al.* (1995)]. In the following, the main production processes for the light element will be explained.

1.1.1 Primordial nucleosynthesis

Primordial nucleosynthesis is one of the three observational evidences for the Big-Band model, that includes also, the universal expansion[1] and the Cosmic Microwave Background radiation (CMB) [2]. At 1 s after Big Bang the background radiation has temperature $\sim 1 \times 10^{9}$K. In previous eras radiation is so strong that bound nuclei could not exist. Now bound nuclei can be formed and survive leading to the formation of light elements: H is converted into ^{2}H, ^{3}He, ^{4}He and ^{7}Li. Primordial nucleosynthesis probes the Universe to the earliest times, from a fraction of a second to hundreds of seconds.

As the Universe evolved from its early, hot, dense beginnings (the "Big Bang") to its present, cold, dilute state, it passed through a brief epoch when the temperature (average thermal energy) and density of its nucleon component are such that nuclear reactions building complex nuclei could occur. Because the nucleon content of the Universe is small and because the Universe evolved through this epoch very rapidly, for T$\leq 10^{9}$K it is possible the formation of light nuclei (D, ^{3}He, ^{4}He, and ^{7}Li) from the starting chemical species, protons and neutrons. The absence of stable nuclei with A=5 and A=8, together with the increasing of the Coulomb barrier for reactions between the heavier nuclei substantially stops the

[1] Galaxies are receding from us with a velocity V_{rec}, proportional to distance D. This is summarized by the Hubble law: $V_{rec}=H_0 \times D$ where H_0 is called Hubble parameter. The Hubble law can be considered as a direct consequence of the expansion of the Universe assuming that spatial dimension are all proportional to a scale factor *a(t)* that increase with time.

[2] When recombination of the free electrons with protons occur(the temperature drops below 3000 K) the space is filled with neutral atoms becoming transparent for the first time, the thermalized photons are free to roam the Universe. Because of the expansion, photons are affected by redshift so that their temperature dropped to 2.725 K. This radiation is now in the microwave domain and is called Cosmic Microwave Background radiation.

cosmological production in correspondence of ^{7}Li in Standard Big Bang Nucleosynthesis. For these standard models, in fact, is not expected the formation of ^{6}Li, ^{10,11}B and ^{9}Be [Malaney & Mathews (1993)]. The present cosmic abundances of these elements are in full agreement with the Big Bang hypothesis.
The study of primordial nucleosynthesis aims to predict the abundances of the nuclei generated within the first three minutes of the Universe life, before temperature and density fell down to low values thus rendering further fusion highly unlikely Big Bang Nucleosynthesis begins about three minutes after the Big Bang, when the Universe has cooled down sufficiently to form stable protons and neutrons. These primordial abundances can, in principle, be deduced from astronomical observations of objects that were formed shortly after the Big Bang. Big Bang Nucleosynthesis used to be the only method to determine the baryonic content of the Universe. In particular the key parameter which allows one to describe the effects of BBN is the baryon-to-photon ratio η. This parameter corresponds to the temperature and density of the early universe and allows one to determine the conditions under which nuclear fusion occurs. This one is related to Ω_B , the ratio of the baryon mass density to the critical density:

$$\eta = n_B \setminus n_\gamma \simeq 2.68 \times 10^{-8} \Omega_B h^2 \tag{1.1}$$

In fact, the power of the Big Bang standard model consists that only this free parameter is necessary in order to get all the primordial abundances of elements synthesized immediately after the Big Bang. The parameter η is related to the baryon density of the Universe ρ_B [Copi *et al.* (1995)] through the relation:

$$\rho_B = m_p \eta n_\gamma \tag{1.2}$$

where m_p is the proton mass. If one considers, also, the critical density of the Universe:

$$\rho_c = \frac{3H^2}{8\pi G} \tag{1.3}$$

where G is the gravity constant and H is the Hubble constant in km/sec/Mpc , it is possible to define the adimensional baryonic density of the Universe Ω_B:

$$\Omega_B = \frac{\rho_B}{\rho_c} \tag{1.4}$$

If the number of baryons is high, the nuclei of ^{2}H and protons have a high probability of fusing to form nuclei of ^{4}He; the same for the nuclei of ^{3}He, so the abundance of primordial ^{2}H highly depends on η. Therefore it can fix the cosmological parameter $\Omega_B h^2$ if a measurement or estimate of its primordial abundance is provided. Because the baryon density is the sole parameter in the SBBN, observations of D, ^{3}He, ^{4}He, and ^{7}Li in astrophysical environments not yet affected by subsequent stellar evolution offer a direct way to infer the baryon density of the Universe and to assess whether the SBBN theory correctly describes the first three minutes of the hot early Universe.

Nowadays, there is still disagreement on which is the value of η. An important way to determine the value of η is given by the study of the cosmic microwave background (CMB) that provide an independent method for constraining η through the *Wilkinson Microwave Anisotropy Probe* (WMAP). The first release of results from WMAP makes the CMB the prime cosmic baryometer, owing to the high WMAP precision. A combination of WMAP data with other finer scale CMB experiments [Pearson (2003)] and with astronomical measurements of the power spectrum [Percival (2001)] and Lyman α data [Croft *et al.* (2002), Gnedin & Hamilton (2002)] gives value for Ω_b h^2 $\eta_{10,CMB} = 6.1^{+0.3}_{-0.2}$ [Spergel (2004)], this value fixes the primordial abundances of the light elements in the framework of SBBN. Using the η value and the SBBN predictions is possible to obtain the primordial abundances of light elements. Indeed this parameter is closely related to the values of the primordial abundances. If η increases will increase the baryonic density and therefore the possibility of interaction of various nuclei. At present a good prediction is Ω_b h^2= 0.023 $\pm$0.002 from which $\eta \sim$4-7$\times10^{-10}$ which fairly agrees with the estimates derived from the CMB fluctuations [Chiosi (2009)].

Figure 1.1 represents the comparison, where it is possible, between the predicted and observed values of primordial abundances in terms of η. We will now give an up-to-date review of the light elements abundance in BBN.

1.1.1.1 Deuterium

Deuterium has a very simple chemical evolution history, as it is the first nucleus to appear in Big-Bang nucleosynthesis. Its abundance gave the first indication

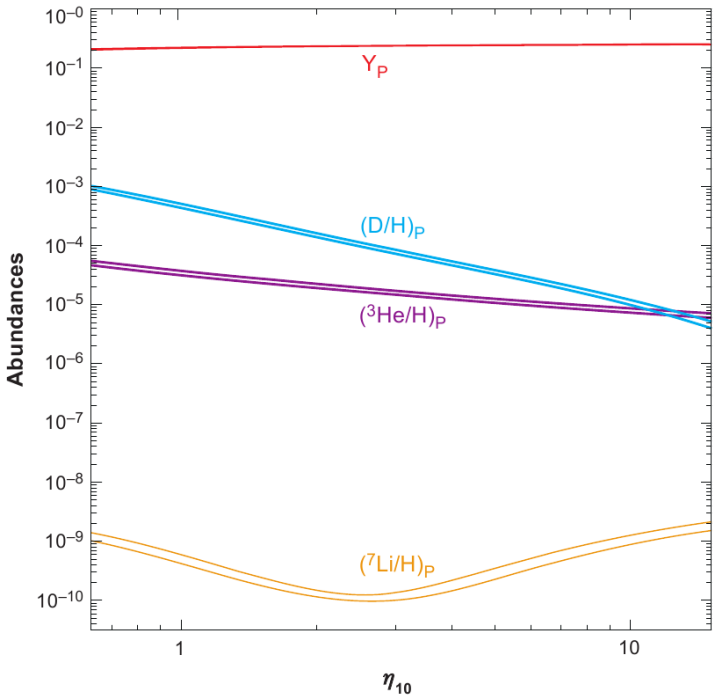

Figure 1.1: The primordial abundances of D, ^{3}He and ^{7}Li (relative to hydrogen number) and ^{4}He mass fraction Y_P as a function of the baryon-to-photon ratio η. The outline boxes represent observational constraints. The vertical band represents the baryon density constraints from WMAP [Cyburt (2005)].

that the Universe is not bound by nucleonic matter [Reeves (1972)]. Moreover, Deuterium is not generated by normal stellar synthesis. The only other source of D is the spallation of ^4He by galactic cosmic rays, which contributes only one part in one thousand of its present abundance. As the most weakly bound of the light nuclides, any deuterium cycled through stars is burned to ^{3}He and beyond during the pre-main sequence, convective (fully mixed) evolutionary stage.
Moreover the Deuterium can only be destroyed after BBN, in particular at the very first stage of star formation. Its primordial abundance has thus to be determined from the observation of cold objects. Clouds at high redshift on the line of sight of even more distant quasars are thought to be the best candidates. Observation of D in high-redshift quasi-stellar object (QSO) absorber provide an

estimate of primordial deuterium abundance in terms of deuterium-to hydrogen ratio D/H= $2.78^{+0.44}_{-0.38}\times10^{-5}$ [Kirkman *et al.* (2003)]. WMAP observation together with SBBN calculations lead to the mean primordial D/H value of 2.6×10^{-5}. In terms of η the first value correspond to η_{10}=5.9±0.5 [Kirkman *et al.* (2003)]; this value results to be very close to the value η_{10}=6.13±0.25 deduced from the WMAP independent determination of the baryon content [Romano *et al.* (2003)].

1.1.1.2 Helium

The helium-3 nucleus is produced in significant quantity both by BBN and by stellar synthesis and it is found primarly in the outer stellar layers, where the temperature is not high enough to complete helium burning all the way to ^4He [Reeves (1972)]. Other processes in novae or other advanced stage of stellar evolution may further generate significant amounts of ^3He. Observations of ^3He, are restricted to the solar system and the Galaxy. Since for the latter there is a clear gradient of metallicity with location, a gradient in ^3He abundance was also expected. However, the data reveal no statistically significant correlation between the ^3He abundance and metallicity or location in the Galaxy, suggesting a very delicate balance between net production and net destruction of ^3He. ^3He is not a very good baryometer, recently has been obtained a small range of $(^3He/\mathrm{H})_p$=(1.1±0.2)×10 $^{-5}$ for a Galactic HII region[1] [Bania *et al.* (2002)], namely a region where the activity should not have contaminated the pristine ^3He abundances significantly.

More precise determinations of $(^3He/\mathrm{H})_p$ do not constrain the value of η_{10} because of the weak dependence of $(^3He/\mathrm{H})_p$ on the baryon density [Romano *et al.* (2003)]. While both D and ^3He are consistent with the SBBN predictions, ^3He is a less sensitive baryometer than D, since $(\mathrm{D/H})_{BBN}\propto {\eta_B}^{-1.6}$, while $(^3\mathrm{He/H})_{BBN}$ $\propto {\eta_B}^{-0.6}$. While the central value of the ^3He-inferred baryon density parameter is in nearly perfect agreement with the WMAP value. Still, ^3He can provide a valuable BBN consistency check [Romano *et al.* (2003)]. For the case of ^{4}He the

[1] An H II region is a large cloud of gas and ionized gas of glowing low density in which star formation has recently taken place. HII regions can be seen out to considerable distances in the universe, and the study of extragalactic H II regions is important in determining the distance and chemical composition of other galaxies

hypothesis about its origin is changed in the last years. The post-BBN evolution of ^{4}He is quite simple. As gas cycles through generations of stars, hydrogen is burned to helium-4 (and beyond), increasing the ^{4}He abundance above its primordial value. However, since the "metals" such as oxygen are produced by short-live, ^4He is synthesized (to a greater or lesser extent) by all stars. Although ^4He is observed in Galactic HII regions, the key data for inferring its primordial abundance are provided by observations of helium and hydrogen emission (recombination) lines from low-metallicity, extragalactic HII regions. The primordial abundance by mass of ^4He (Y_p) is derived by analysis the helium content in low metallicity extragalactic HII regions. Very recently [Peimbert *et al.* (2007)] derived Y_p =0.2477± 0.0029 by studying the helium abundance in HII region.

1.1.1.3 Lithium-7

^7Li has the unique characteristic of owing its abundances to three different mechanism. The BBN contribution dominates the galactic gas abundance in the first billions of years [Reeves (1972)]. When the galactic mass fraction of heavy elements become larger than one part per thousand, a still unidentified stellar source managed to increase the abundance by an extra factor of ten. The observation of lithium abundances in evolved stars of the asymptotic giant branch suggests that these stars play a role in the ^7Li origin. Moreover also spallation processes are responsible for Li formation.

The detection of Li in very metal deficient stars of the galactic halo, usually interpreted as the signature of the primordial abundance of ^{7}Li was discovered by Spite & Spite who interpreted this constant Li abundance as corresponding to the BBN ^7Li production [Spite & M. Spite (1982)]. This interpretation assumes that lithium has not been depleted at the surface of these star so that the presently observed abundance is equal to initial one. The presence of the "Spite plateau" is an indication that depletion has not been very effective.
On the other hand the younger stars ([Fe/H][1]>-1) display a large dispersion in

[1]In astrophysics the metallicity represent a measure of the proportion of "heavy elements" or "metals" that a star contains. This value, denoted as [Fe/H] is calculated by:

$$[Fe/H] = log(N_{Fe}/N_H) - log(N_{Fe}/N_H)_{\odot} \tag{1.5}$$

lithium abundances reflecting the effects of different production and destruction mechanism. Observation [Ryan *et al.* (2000)] have led to a relative primordial abundance of Li/H=$1.23^{+0.68}_{-0.32}\times10^{-10}$ obtained by extrapolation to zero metallicity. Abundances measured at low metallycities are less contaminated by the effect of galactic evolution than interstellar abundances.

1.2 Cosmic Ray Nucleosynthesis

A striking discontinuity in the solar system abundance curve of the elements is the very low abundance of the light element Li, Be and B compared to their neighbors element as seen in Fig 1.2. The LiBeB abundances are lower by about five orders of magnitude which respect to the CNO elements and seven order of magnitude compared to H and He. These low abundances are related to the fragility of these element in typical stellar burning conditions. It was consequently soon recognized that even the very small quantities of LiBeB present in solar system material cloud not be produced in stellar nucleosynthesis. For the first time, fifty years ago Burbidge, Fower and Hoyle [Burbridge *et al.* (1957)] addressed this problem by proposing an unknown process responsible for the synthesis of these light elements. Later, Reeves, Fowler and Hoyle [Reeves *et al.* (1970)] proposed the spallation scenario for the production of the light elements via the interaction of energetic cosmic-ray protons and α particles with heavier nuclei of the interstellar medium. The cosmic-ray origin of most of ^{7}Li and ^{11}B, and essentially all ^{6}Li,^{9}Be and ^{10}B is nowadays the widely accepted standard scenario. Part of ^{7}Li is produced in primordial nucleosynthesis and probably another part is of stellar origin while ^{11}B may have a component produced in supernovae explosion by neutrino spallation of ^{12}C.

The discovery of cosmic rays dates back to the early 20th century when there was clear evidence of an ionizing radiation penetrating from outside Earth's atmosphere [Hesse (1936)]. This radiation can be observed down to sea level and traces of it persist even below hundred meters of rock. It is induced by high-energy particles which interact with air molecules at high altitude and create a cascade

where N_i is the number of atoms for cm ^{3} for hydrogen and for other elements heavier then H.

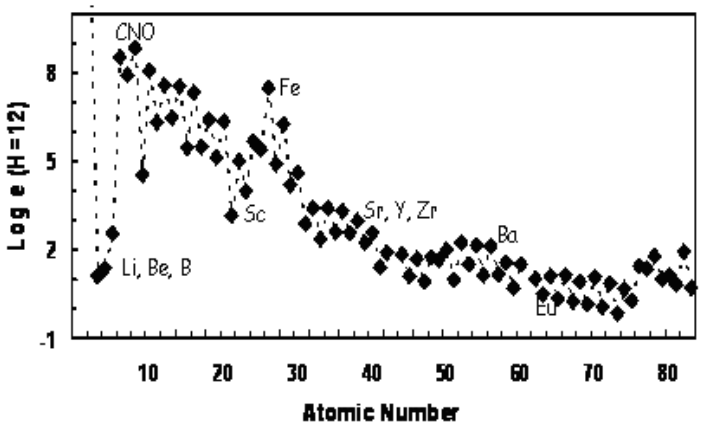

Figure 1.2: Curve of the abundances of elements that are evident the decrease for light elements and the 'iron peak' [Grevesse & Sauval (2001)].

of secondary particles typically starting at 10-20 km above sea level. These cascades, also called "air showers" are composed of an electromagnetic part, mostly electrons, positrons, muons and γ-rays and a hadronic part, primarily nucleons and pions. Several ground-based detection methods have been used for these cascade, extended detector arrays intercepting directly the ionizing particles and telescopes observing the scintillation and/or the Cherenkov light induced by air shower particles. These detection methods work only above $\approx 10^{14}$eV, air showers induced by primarily particles below that energy are to weak for ground-based instruments. Figure 1.3 shows the incoming particle flux as a function of energy. Is possible to observe a regular power-law function from 10^{11} to about 10^{20} eV, while is also evident a slight steepening around 10^{15}eV "Knee".

It is generally believed that the flux at least up to the knee, maybe even up to the ankle is of Galactic origin, while the highest energy cosmic rays are of extragalactic origin [Meneguzzi *et al.* (1971)]. At lower energy a drawback is the influence of the heliosphere on the particle flux. The solar wind carries magnetic turbulence with it, which scatters the cosmic rays penetrating the heliosphere affecting the flux below several GeV per nucleon.

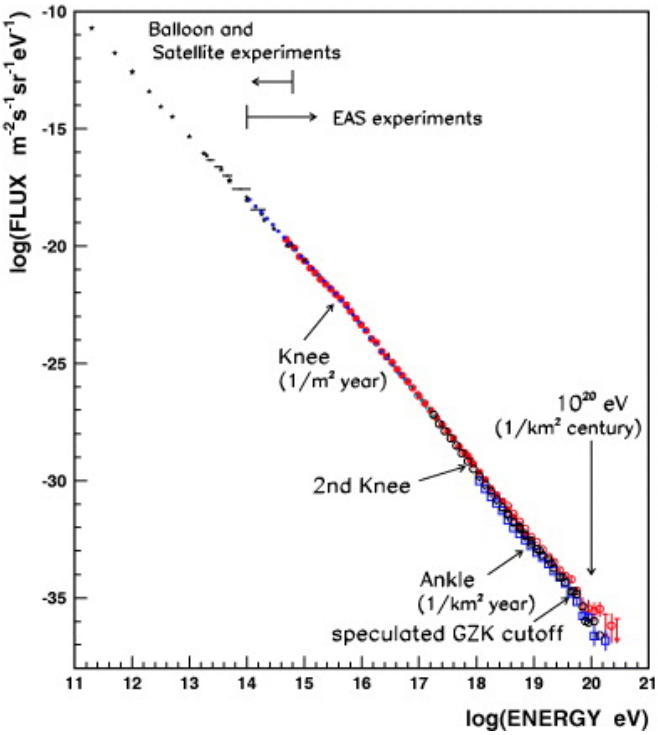

Figure 1.3: A compilation of measurements of the primary cosmic rays energy spectrum. Direct observations with balloon- and satellite-borne detectors are plotted as dots below the knee, around 10^{15} eV. New Tibet results, which cover the energy region below and above the knee, are plotted as blue circles. In the highest energy region, new results from HiRes and Auger are shown as open black circles and open blue squares, respectively. The overall spectrum is expressed by a power law from 10^{11} to 10^{20} eV with only small changes of slope around 10^{15} eV (the knee), 10^{17} eV (the second knee) and 10^{19} eV (the ankle) [Nagano (2009)].

It is so called solar modulation and it must be taken into account when wants to derive the cosmic ray flux outside the heliosphere, the local interstellar flux (LIS) which is needed for the understanding of Galactic cosmic ray propagation and the resulting nucleosynthesis. In Figure 1.4 is shown the evolution of low energy proton flux. The spectrum can be represented at high energies by a power-law spectrum, $\Phi_p(\mathrm{E}) \propto \mathrm{E}^x$ where $\Phi_p(\mathrm{E})$ is the differential flux of nuclear species P at kinetic energy E per nucleon and x= 2.5-2.7.

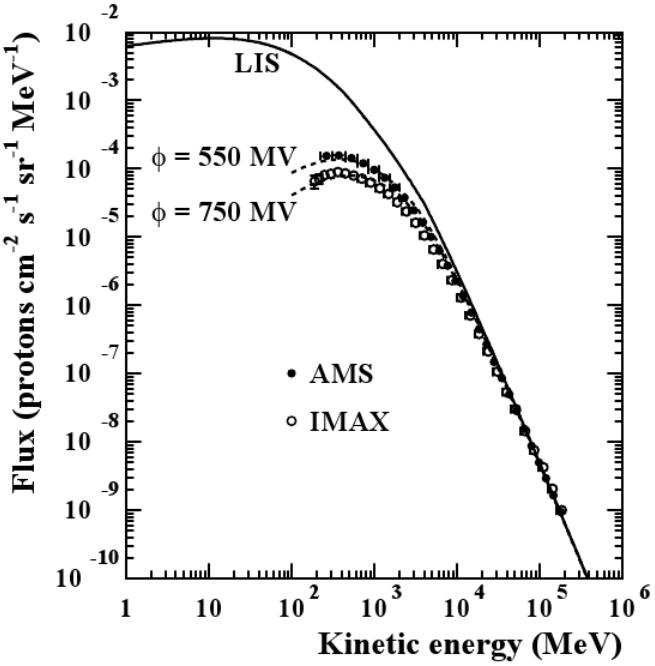

Figure 1.4: Cosmic-ray proton local interstellar spectrum (LIS) solid curve, and solar modulated spectra for two force-field potential (dashed curves). AMS: [Alcaraz *et al.* (2000)], IMAX: [Menn *et al.* (2000)]

The exact composition of primary cosmic rays, outside the Earth's atmosphere, is dependent on which part of the energy spectrum is observed. The flux ratios of different nuclear species and consequently the cosmic ray composition are much less affected by solar modulation, making these observables the primary constraints for the GCR propagation models. The cosmic-ray composition compared to the standard solar system abundances is shown in figure 1.5. The most remarkable differences are for LiBeB and the element just below the iron peak, both presenting much higher relative abundances in the cosmic ray composition. On the other hand both composition are quite similar. Assuming that the source cosmic ray composition at the acceleration sites is not too far from the solar system one, the GCR LiBeB are practically purely secondary particles, produced by spallation of the abundant CNO and Fe GCR isotopes during their propagation to the solar system.

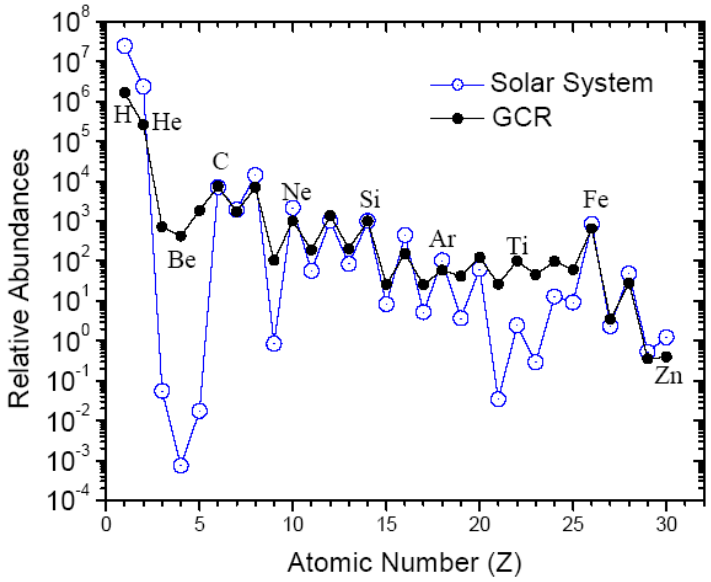

Figure 1.5: Cosmic-ray composition and standard solar system abundance curve.

Regarding the cosmic ray composition, almost 90% of all the incoming cosmic rays are protons, about 9% are helium nuclei (alpha particles) and nearly 1% are electrons [Meneguzzi *et al.* (1971), Reeves *et al.* (1970)]. The ratio of hydrogen to helium nuclei (28 helium by mass) is about the same as the primordial elemental abundance ratio of these elements (24% by mass He) in the Universe. There is not any identification about their astrophysical sites of origin. One hypothesis suggests that some cosmic ray are nuclei ejected by supernovae and another one suggests that the nuclei in the interstellar gas being accelerated to high velocities by the shock waves from later supernovae.

The cosmic-rays and their isotopic abundances are an important channel of information about the galaxies and intergalactic space, since the cosmic rays represent the only accessible sample of matter of extra-solar origin. The LiBeB anomaly is explained by the interaction of cosmic rays with interstellar matter. Shows that the nuclei in question can be easily produced through a process known as spallation[1] in collisions between high energy cosmic-rays nuclei and the nuclei of interstellar matter. These are produced mainly by nuclear interactions, for

[1] The nuclear reaction with several particle in the exit channel are called spallation reactions [Rolfs & Rodney (1988)].

example if we consider the ^{12}C nuclei in the interstellar medium bombarded by cosmic rays, we can write some of the reactions that take place. In this one the ^{12}C nuclei break up into fragments such as LiBeB:

$$\begin{aligned} p + {}^{12}C &\rightarrow {}^{11}B + 2p\,(Q = -16MeV) \\ p + {}^{12}C &\rightarrow {}^{11}B + 2p + n(Q = -27MeV) \\ p + {}^{12}C &\rightarrow {}^{9}Be + 3p + n(Q = -34MeV) \\ p + {}^{12}C &\rightarrow {}^{7}Li + 4p + 2n(Q = -53MeV) \\ p + {}^{12}C &\rightarrow {}^{6}Li + 4p + 3n(Q = -60MeV) \end{aligned} \tag{1.6}$$

Spallation reaction take place in an environment relatively cool and with a very low density and in this environments it is allowed the LiBeB production and their survival after their formation [Reeves *et al.* (1970)]. The relative height negative Q-values of this reactions are easily matched by the high-energy cosmic ray particles. In the simplest model of cosmic-ray nucleosythesis it is important to take into account all possible projectiles and target. In particular, inspection of the abundance distribution suggests that these are primarily p+CNO spallation reactions. In the case of collision between a cosmic ray proton (projectile) and CNO interstellar matter (target) the spallation products LiBeB have low energy and thus an height probability for thermalization and incorporation into the stellar medium [Rolfs & Rodney (1988)]. It is evident that this theory can explain the abundances of ^{6}Li, Be and probably ^{10}B and ^{11}B.

The GCR appears to produce too much ^{10}B and ^{11}B but the agreement is within the observational uncertainty and theory. The process is one of slowest in nature, new stars are eventually formed out of this gas, which reveal by their absorption features the presence of these atoms in their surface layers. This so called 'gallactogenetic' hypothesis has been presented by Reeves *et al.* (1970). In this theory the range in energy spectrum per nucleon of the GCR will be subdivided into three regions: regions I extends up to 5 MeV in which no Li, Be o B are produced, region II is from 5 MeV to 30 MeV where only ^{11}B is produced, and region III is above 30 MeV where all the light elements are produced [Meneguzzi *et al.* (1971)].

1.2.1 Nuclear interaction of Cosmic-rays: LiBeB production

For calculation of total rate injection of decelerated spallation products, crucial importance has the knowledge of the nuclear cross section for formation and destruction of the light nuclei. In fact generally in the simplest model of cosmic-ray nucleosynthesis the production yield per unit time of a nuclide is:

$$\frac{dN_1}{dt} = \sum N_T \int_0^\infty \Phi_P(E)\sigma_{P,T}(E)dE \tag{1.7}$$

where Φ_P(E) is the flux of the high energy cosmic-ray projectiles P inducing the spallation reactions, N_T is the number density of the target nuclei T in the interstellar medium, and $\sigma_{P,T}$(E) is the cross section for production of nuclides in the collision of P and T. For the synthesis of LiBeB, three production process are prevailing:

- spallation reaction induced by GCR protons and α particles on heavier nuclei in the gas and dust of the interstellar medium. Due to their abundances and cross sections,^{12}C,^{14}N, and ^{16}O are the most important target nuclei. After the collision the produced LiBeB nuclei have relatively low energies, (MeV) and are stopped in the interstellar medium usually without further nuclear interactions.

- Spallation reactions in inverse kinematics energetic CNO nuclei interacting with hydrogen and helium nuclei of the interstellar medium. In this case, LiBeB have approximately the same energy per nucleon and may be destroyed in subsequent collisions or leave the galaxy. So, this channel contributes less then reaction in direct kinematics in standard GCR nucleosynthesis.

- Both stable lithium and isotopes are furthermore abundantly produced in collisions of GCR α particles with He. In the standard model most Li is produced by this process.

In all three channels, production of radioactive nuclei contributes to the synthesis of the stable isotopes, ^{6}He and ^{9}Be for Li, ^{9}Li for Be and ^{11}Li,^{10}Be, ^{11}Be, ^{10}C and

^{11}C for B. Summarizing what we know from GCR, the nucleosynthesis of LiBeB is dominated by GCR. They are responsible for the bulk production of all isotopes and the only nucleosynthsis source of ^{6}Li,^{9}Be and ^{10}B. The amount of the different elements is produced in the right absolute scale and right proportion.

1.3 Stellar production

Among the light elements Li, Be and B, ^{7}Li is thought to arise from a variety of processes including Bing Bang nucleosynthesis [Spite & M. Spite (1982)], as explained before, asymptotic giant branch stars[1] (AGB), novae[2] [D'Antona & Matteucci (1991)] and ν-process in TypeII supernovae [3][Woosley (1990)]; the latter may also contribute to ^{11}B production. The mechanism responsible for lithium production has been proposed by Cameron & Fowler (1971): ^{7}Be is produced by fusion of ^{3}He and ^{4}He, and rapidly transported to stellar regions where it can be converted into ^{7}Li. Notice, then, that the lithium production may last only until there is ^{3}He available in the region of burning, and that the production ends when the ^{3}He is all consumed.

There are two main physical situations where this mechanism can produce enough lithium that is important to investigate their role in the galactic production: the first one is the explosive hydrodynamical formation during the outburst

[1]For stars less massive than about nine times the mass of the sun, the last major phase of life is as an Asymptotic Giant Branch (AGB) star. This final phase of hydrogen burning happens after the star has moved from the Main sequence, through the Red Giant Phase and past the Horizontal Branch. At this point they are characterized by an inert carbon-oxygen core, surrounded by two separate nuclear burning layers - an inner layer of Helium and an outer layer of Hydrogen. These layers are in turn surrounded by a strongly convective outer envelope

[2] Is a cataclysmic nuclear explosion caused by the accretion of hydrogen on to the surface of a white dwarf star, which ignites and starts nuclear fusion in a runaway manner

[3]As part of the attempt to understand supernovae, astronomers have classified them according to the absorption lines of different chemical elements that appear in their spectra. The first element for a division is the presence or absence of a line caused by hydrogen. If a supernova's spectrum contains a line of hydrogen (known as the Balmer series in the visual portion of the spectrum) it is classified Type II; otherwise it is Type I. Among those types, there are subdivisions according to the presence of lines from other elements and the shape of the light curve (a graph of the supernova's apparent magnitude as a function of time).

of novae [Arnould & Norgaard (1975), Starrfield *et al.* (1978)], the second one is the hydrostatic, slow formation in the envelops of asymptotic giant branch (AGB) stars, for which it was first proposed.

- AGB: The importance of studying AGBs has received new interest since they have been suggested as possible candidates to explain the lithium enrichment of the interstellar medium. A first, detailed study on this issue can be found in Mazzitelli *et al.* (1999), and in Ventura *et al.* (1999), where it is shown that it is mass loss the key ingredient constraing the evolution of AGB models in terms of lithium production. In envelope models of AGB stars [Scalo *et al.* (1975)], in which the bottom of the convective envelope reaches the H-shell burning region, and the nuclear reaction products are transported to the surface by convection. This is perfect site of lithium production through the Cameron-Fowler mechanism [Iben (1973), Sackmann *et al.* (1999)]. While in the last years [D'Antona & Ventura (2010)], it is observed that the temperature as large as T$\sim$40 MK, is sufficient to produce lithium. These models able to explain the high lithium abundances found in some luminous red giants, and the process took the name of Hot Bottom Burning (HBB). This is a new models of lithium production in AGB stars [D'Antona & Ventura (2010)], this model gives an information about on the possible role of this stars as efficient lithium factories.

- Novae: Another interesting source of ^{7}Li is in the nova outbursts. Arnould & Noergaard(1975) proposed that the Cameron-Fowler mechanism, acting at the nova outburst, would produce lithium abundance proportional to the ^{3}He abundance in the nova envelope. After, is has been shown [Starrfield *et al.* (1978)] that the mechanism could be efficient for outburst temperatures >150 MK, and the fast ejection of the ^{7}Be rich nova shell leads to ^{7}Li production. The nova explosion occurs when a critical hydrogen rich envelope is reached on the white dwarf component of the nova binary, by accretion from its low mass companion. By losing mass, low mass stars expose the stellar region in which the hydrogen burning p-p chain is incomplete, and thus the mass transfer phase, and during the mass transfer itself [D'Antona & Mazzitelli (1982)].

As a result, mainly the novae containing an "old" white dwarf, and therefore an old and ^{3}He-rich low mass companion contribute to the galactic production of lithium. Including the lithium production in the galactic chemical evolution model, novae appear to be a modest lithium producer [Romano *et al.* (1999)].

- SN TypeII: Another potentially interesting source of ^{7}Li is the ν-process in Type II supernovae [Woosley (1990), Woosley & Weaver (1995)]. During supernova explosions, a huge amount of neutrinos are emitted, blowing off surface materials from the proton-neutron star. The neutrino interact with nuclei in supernova ejecta, and the neutrino emission is strong enough to change the compositions, despite the small cross sections for neutrino-nucleus interactions. The neutrino induced reactions mainly affect a kind of proposed nucleosynthetic process that occur during supernova explosions: the synthesis of light elements such as Li and B through the ν-process in the He layer. The production of light elements through the ν-process during supernova explosion was the aim of many studies [Domogatsky *et al.* (1978), Woosley (1990)] that evaluated the roles of ν-process and showed that a large amount of ^{7}Li and ^{11}B is produced during supernova explosion. The problem is the overproduction of ^{11}B from the supernova ν-process in the Galactic chemical evolution models of the light elements [Olive *et al.* (1994)], the overproduction means that the predicted ^{11}B abundance in theoretical calculations is overabundant compared to the observed one. The production of ^{11}B in the supernova ν-process is identified as the most important process for explaining the very precise data of the meteoritic ^{11}B/^{10}B abundance ratio. Several authors studied Galactic Chemical Evolution models of the light element by taking into account of the contribution of the supernova ν-process, and they showed that the amount of ^{11}B is too large by a factor of 2 [Fields *et al.* (2000)] to 5 [Ramaty *et al.* (2000)], while the other light elements are well produced in the appropriate amount. Mass loss of the outer envelope in the supernova evolutionary phase would decrease the efficiency of ^{11}B production in the ν-process during the supernova explosion. The production of ^{7}Li and ^{11}B during supernova explosion depends on the

supernova models. It also depends on the details of the total neutrino luminosity and its time variation. Moreover, the yet uncertain average neutrino energy should strongly affect the ν-spallation cross section of ^{4}He providing seed elements for the production of ^{7}Li and ^{11}B.

1.4 Li, Be and B: observational status.

The easiest of the three elements to observe is Li, and spectroscopic observations of Li have been made in a large array of stars of various age and metallicities and evolutionary phases, as well as in the interstellar gas. Due to the atomic and spectroscopy properties of Be and B, they have been less extensively observed. The major reason for the relatively few Be observation is that Be is observed through the resonance lines of BeII 3130.414 Å and 3131.058 Å, a spectral region not nearly accessible to ground-based telescopes as the LiI. However, information on all the three elements complement each other and can shed light on several issues of astrophysical interest. In the study of light elements, the results are most often presented as plots of the light element abundance as a function of metallicity [Fe/H] or as a function of stellar effective temperature T_{eff} [Boesgaard *et al.* (2001)]. The number of measurements of light elements abundances, and the variety of sites in which these have been performed, have increased in the last years. The primordial abundances cannot be determined without knowing the sources and sinks of the element, and the degree of mixing for stars of different metallicity cannot be determined from the observations unless the contribution of Galactic production is known.

1.4.1 Lithium

Li can be formed by several different processes, as discussed in the first section. The interstellar abundances of ^{7}Li cannot be directly derived from spectroscopic observations, always must to be apply a correction for the ionization of lithium on the ISM, and for its depletion onto interstellar grain. The main results on the abundances of Li were obtained by spectral observations made at wavelengths of 6707.76 Å and 6707.91 Å and corresponding to the ^{7}Li doublet resonant neutral

Li I. Abundance of Li have been plotted against metallicity [Fe/H] for both disk stars and halo stars[1], Figure 1.6 shows a composite diagram obtained by [Ryan *et al.* (2001)] including different lithium abundances determination available at moment.
The horizontal dotted line represents the meteoritic Li abundances A(Li)[2]= 3.31. There are several features of note on this diagram: the apparent plateau in A(Li) at low metallicities is the first property and it is attributed to the production of Li during the Big Bang. Secondly, is possible to observe several stars at low metallicities whit low upper limits on the Li abundances, the upper limits indicate Li depletions, as they are clearly outliers in the plateau distribution, having abundances only half (or less) the plateau value. Moreover, the stars near solar metallicity show an order of magnitude more Li than the plateau and finally is clear that there is a large range in A(Li).

The Li-rich disk stars are preferentially younger and hotter main sequence star, while the disk stars with lower A(Li) are thought to have had their surface Li depleted via mixing of the photosferic material down to temperatures where Li is destroyed. The rise in A(Li) that occurs between [Fe/H]=-0.4 and -0.2 is too steep to be explained by Galactic cosmic ray spallation production of Li. There is an apparent deficit of stars having high Li abundances with [Fe/H] between -1.0 and -0.; this could be due to sampling bias or effective Li depletion from higher initial Li [Romano *et al.* (1999)]. It was noted a different behavior for this element abundances for stars of population I and population II[3].

[1]From direct and dynamical evidence we know that there is an enormous increase in the density of matter toward the center of the Galaxy, which is referred to as the Galactic *nucleus*. Thus our overall picture of the Galaxy is that of massive nucleus embedded in a rather thin disk of stars, dust, and gas. The dust, gas, and young stars in this disk are arranged along spiral arms. The older stars, however, appear to have a more uniform distribution throughout the disk. Finally, the nucleus and the disk are surrounded by globular clusters, as well as by *halo* of very old stars, also concentric with the Galactic center [Mihalas (1968)].

[2]The Li abundances are given as A(Li)=logN(Li/H)+12, and this notation is used also for beryllium and boron abundances.

[3]The stars in the Galaxy could be divided into two distinct *stellar population*. Population I stars are the young, metal rich stars found in spiral arms, strongly concentrated in the Galactic plane, associated with interstellar dust and gas, and which achieve the highest luminosities observed. Population II stars are old, metal poor stars. They are located in the Galactic

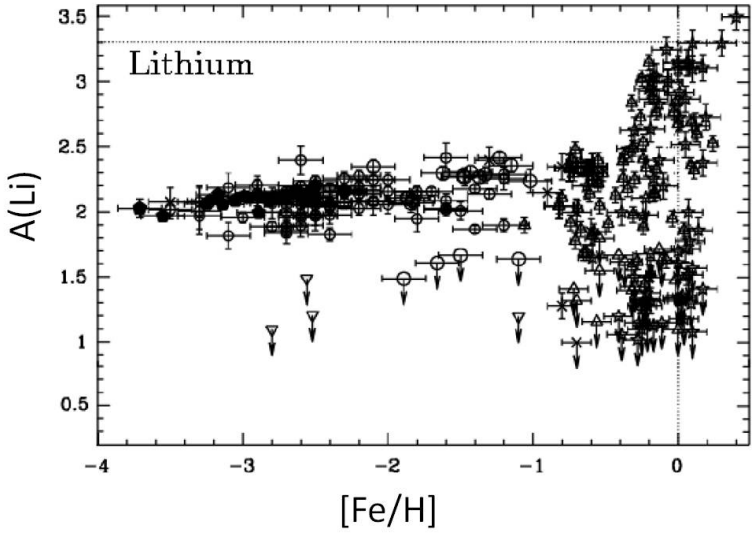

Figure 1.6: Lithium abundances vs. [Fe/H] adapted from Ryan et al.(2001). This sample includes stars hotter than 5600 K. The horizontal dotted line represents the meteoritic Li abundances [Boesgaard *et al.* (2004a)].

The first determinations of the abundance of lithium as a function of T_{eff} in population II stars have revealed the existence of a 'plateau' (as shown in Figure 1.7) centered around the average value of A(Li)=2.05±0.2 corresponding to X_{Li} [1]$= 5.96 \cdot 10^{-10}$ [Spite & M. Spite (1982)]. Over time the comments have improved this value, in particular studies of halo stars it is obtained a value of A(Li)=2.32 ± 0.2, from this extrapolation, we obtain the primordial value of A(Li)=2.22±0.2 [Thorburn *et al.* (1994)]. As a sample of the stars of population I it was considered the Pleyades open cluster. Considering the abundance of lithium in this cluster and plotting the data as a function of T_{eff} of the star observed (Figure 1.8), the trend of lithium abundance with decreasing temperature. Studying the stars of these clusters can be seen also as the surface Li abundance is A(Li)~ 3 corresponds to $10.8 < X_{Li} < 10^{-9}$ [Thorburn & Beers (1993)].

The current value of primordial ^7Li is still controversial, in fact some research favoring the hypothesis that the so-called Spite plateau is truly representative of

nucleus, in a more or less spherical halo around it and in a disk coextending with the Galactic plane, but much thicker than the dust and gas layer [Mihalas (1968)].

[1]The notation X_A is referred to the mass fraction of the element A with respect to hydrogen

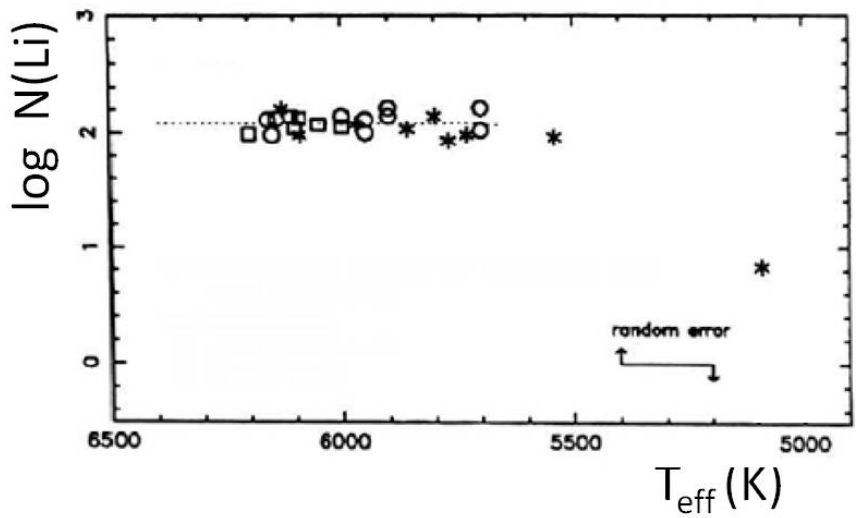

Figure 1.7: Spite plateau in a plot ε(Li) vs.T_{eff} for halo stars with 5800K<Teff <6400 K. Showed an almost constant for lithium (see [Spite *et al.* (1996)]).

the pristine ^7Li content of halo dwarfs, and hence primordial ^7Li abundance [Spite & M. Spite (1982), Spite *et al.* (1996), Bonifacio & Molaro (1997)] while other authors suggesting the existence of non standard depletion process to reproduce the observed plateau value starting from a higher primordial one [Thorburn & Beers (1993), Vauclair & Charbonnel (1995), Pinsonneault *et al.* (1999), Pinsonneault *et al.* (2002)].

Other works [Asplud *et al.* (1986), Bonifacio & Molaro (1997)] shows an increase in the dispersion at low metallicity, the presence of a slope with metallicity, or more precisely of a discontinuity in the Li abundance at [Fe/H]=-2.5 and conclude for a rather low primordial value somewhat around A(Li)=2.1, this value is very close to the initial value of 2.05 proposed by Spite more than 20 years ago. Due to the possible discrepancies in the value caused by T_{eff}, it is possible to find a convergence of the various measures and methods around a common range of values between A(Li) =2.2-2.28. The WMAP determination of the baryon-to-photon ratio implies, through Big Bang nucleosynthesis, a cosmological Li abundance larger, by a factor of 2 to 3, than the Li abundance plateau observed in the oldest Pop II stars [Richard *et al.* (2005)].

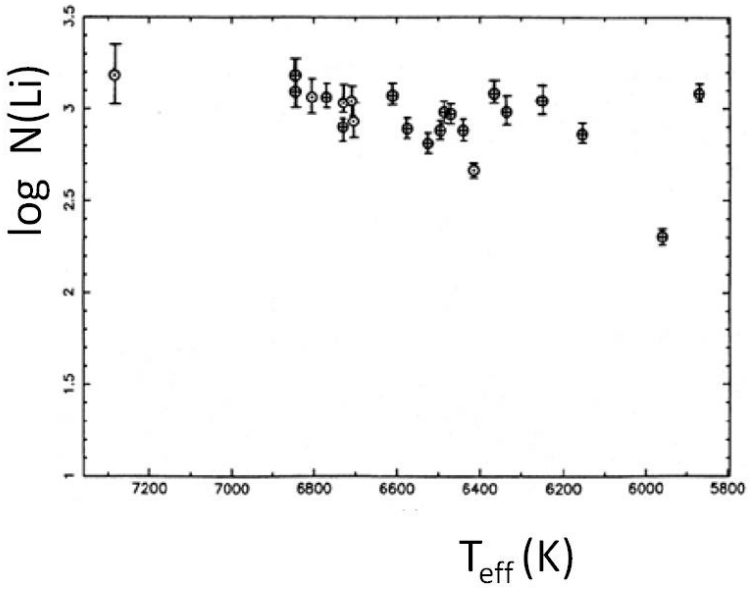

Figure 1.8: Lithium abundance as a function of T_{eff} over system of the Pleiades. For these young clusters there is not strong evidence of the depletion of Li [Assenbaum (1987), Boesgaard & Tripicco (1986)].

A solution of the Li problem may still reside in the ability to reconstruct the complexity of the stellar atmosphere, systematic errors in the T_{eff} able to increase the Li value to match the WMAP value seem unlikely. It is thus possible that a disagreement may be real revealing the presence of unaccounted processes in the BBN. Table 1. shows the values of the abundances of lithium in various astrophysical environments.

Astrophysical environment	A(Li)	Reference
Meteorites	3.3	Anders & Grevesse (1989)
Sun	1.3	Anders & Grevesse (1989)
Interstellar medium	2.3-2.8	White et al.(1986)
Population I stars	~ 3	Thorburn et al (1993)
Population II stars	2.05-2.22	Thorburn et al (1994)

Table 1.1: Li abundances in various astrophysical environments.

1.4.2 Beryllium

The observations made for beryllium show that also for this element is possible to make a similar discussion to the one made for Li [Stephens *et al.* (1997)]. As we saw the dominant mechanism for the production of beryllium is determined by the spallation reactions of Galactic cosmic rays [Reeves *et al.* (1970), Ramaty *et al.* (2000)] although in recent times has noted the possibility of production of beryllium, even in Supernovae II [Boesgaard *et al.* (2004a)]. The Standard Models of Big Bang nucleosynthesis is not able to reproduce the "lowest observed value" of about $N_{Be}/N_H=10^{-14}$ [Primas *et al.* (2000)] for the beryllium abundance giving a value of some $N_{Be}/N_H{}^{theor}=10^{-18}$ [Gilmore *et al.* (1992). This model leads to an enhancement of a factor 10-30 for the predicted primordial abundance [Jedamiz & Rehm (2001)] but there is some problem mainly due to the observational limits. The abundance of beryllium in the stellar atmosphere is detectable through the study of the resonant doublet neutral beryllium BeII at wavelengths 3130.414 Å and 3131.058 Å. Since these lines are in the region near UV the observations are performed both by land and by HST (Hubble Space Telescope).

Figure 1.9 shows the trend of A(Be) as a function of metallicity for halo and disk stars. Data are from a number of different papers [Stephens *et al.* (1997), Boesgaard *et al.* (1999), Boesgaard *et al.* (2000), Boesgaard *et al.* (2001), Boesgaard & King (2002), Primas *et al.* (2000), Santos *et al.* (2002)] but the figure presents a good overview. The increase in A(Be) with [Fe/H] is obvious, and the slope of the relationship from [Fe/H]≈-3.0 to ∼ -1.0 is close to 1.0. At low metallicity there may be a flattening toward a plateau in A(Be). The lowest-metallicity stars are the faintest, so those observations are most difficult and time-consuming; observation are needed of Be in more stars with [Fe/H] <-3.0.

The observations indicate that there may be a real spread in A(Be) at a given [Fe/H] in the halo stars. This could result from differing degrees of efficiency in the formation of Be by spallation in different parts of the Galaxy. For some stars with [Fe/H] >-1.0 there are Be deficiencies, including objects with measured Be abundance down to 2 order of magnitude from the meteoritic A(Be)=1.4. There is a large clustering of data points with A(Be) between 1.0 and 1.4 dex near solar metallicity. It is therefore difficult to disentangle the general increase of A(Be)

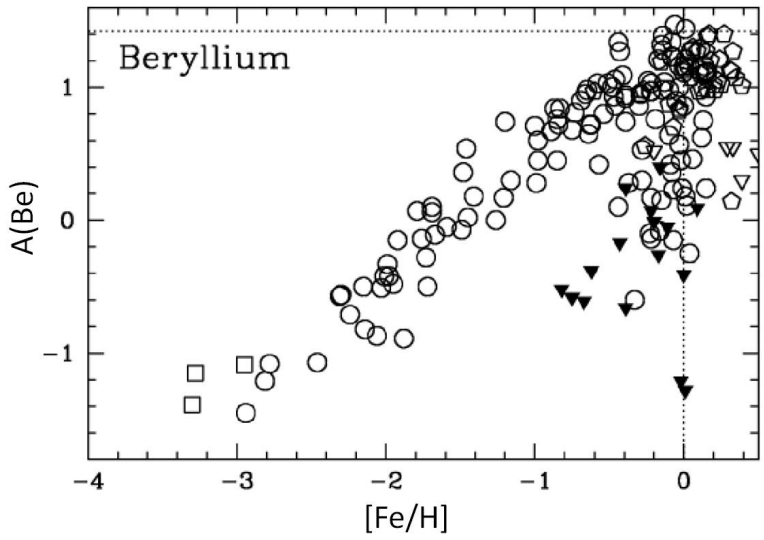

Figure 1.9: Be abundances vs [Fe/H]. Open circles and filled triangles (upper limits) are from Stephens *et al.* (1997), Boesgaard *et al.* (1999), Boesgaard *et al.* (2000), Boesgaard *et al.* (2001). Open squares (low-metallicity stars) are from Primas *et al.* (2000). The open pentagons and triangles (upper limits) are from Santos *et al.* (2002). The horizontal dotted line is the meteoritic Be abundances, A(Be)=1.42 [Anders & Grevesse (1989)].

with [Fe/H] in the disk stars from the spread due to some minor depletion. The upper envelope of data points seems to keep increasing, however, a flatting of the slope or a gentle curvature is possible.

1.4.3 Boron

The determination of the abundances of boron are particularly difficult because the spectral lines used for observation of this element lie in the UV region of the electromagnetic spectrum. For the determination of boron abundances in stars to be exploited, the profile and intensity of the resonant doublet line for the neutral boron BI 2496.771 Å and 2497.723 Å must be measured, while the lines in the NIR are at the wavelengths to 16240.371 and 16244.670 Å [Primas *et al.* (1999)]. Since it is not possible to make observation from the earth of UV spectral regions for the study of boron, the observations were made using high-

resolution spectrograph GHRS (Goddard High Resolution Spectrograph) supplied HST, although in recent years have obtained a higher resolution through the use of HST with STIS (Space Telescope Science Institute) [Boesgaard *et al.* (2004a)].

The observations for determining the abundances of boron have taken a great interest in the implications that would seem to have that element in the understanding of mixing processes in stars of the population I, with masses of the order of one solar mass and in the main sequence [Stephens *et al.* (1997), Boesgaard *et al.* (1998)]. Also for Boron we report the trend of B abundance with metallicity (from BI observations only) Fig 1.10, it is possible to note that there are fewer B data points than Be points, and far fewer than Li. An increase in A(B) with [Fe/H] can be seen in the halo stars which is similar to the trend of Be with metallicity. If the slopes for Be and B are identical, this implies a common origin for the two elements. A shallower slope for B might imply that the ν-process is an important source for B. Moreover as for Be, the stars with [Fe/H] > 0.6 show a spread, possibly resulting from depletion of boron in some of the stars. The points are marked by crosses are stars that are undepleted in Be and thus expected to be undepleted in B.

1.4.4 Light element in Main Sequence Stars: Li, Be B.

Due to the low abundances of the three rare light elements in stellar atmosphere, they are primarily observed in their respective resonance lines as described before. Some features of the stellar internal structure, at various stages of evolution, are revealed by the surface abundances of these light element. Although most previous study have concentrated on Li alone, because each element survives to a different depth, much more powerful model constraints can be derived when more than one element is considered simultaneously; the study of these elements in open clusters, which have a known age and metallicity is of particular interest [Deliyannis *et al.* (1995)].

There is a large amount of information about the Li abundances in F and G dwarfs in both cluster and in field stars. The Li information from clusters of different ages and metallicities is particularly useful in discriminating the mechanism that may lead to the surface depletion of Li.

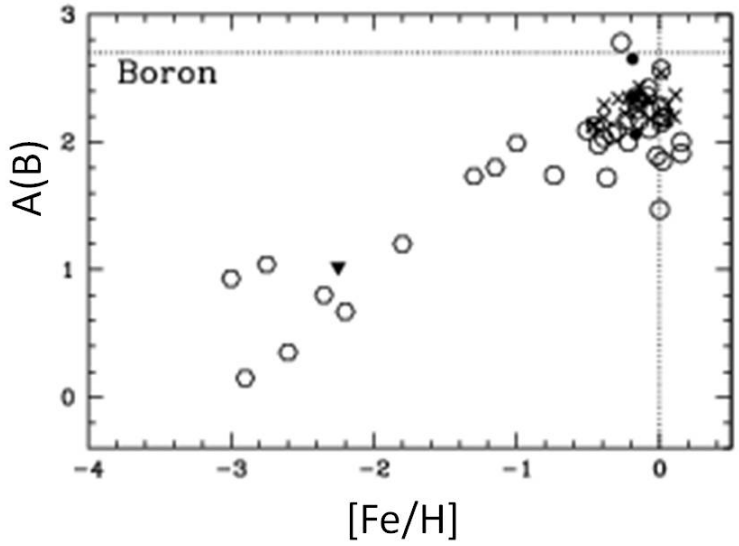

Figure 1.10: Boron abundances from BI vs [fe/H]. The data are from different several papers: the hexagons and the upper limit triangle are from [Duncan *et al.* (1997), Duncan *et al.* (1998),Primas *et al.* (1999), Garca Lopez *et al.* (1998)] ,the crosses are from Boesgaard *et al.* (2004a), the open circles are from [Boesgaard *et al.* (1998)], the solid circles are from [Cunha *et al.* (2000)]. The horizontal dotted line is the meteoritic B abundances A(B)=2.70 [Anders & Grevesse (1989)].

In particular, from the study of Hyades (age $0.8{\cdot}10^9$ years) F stars, [Boesgaard & Tripicco (1986)] it was possible to observe that they have depleted their surface Li-abundances. In figure 1.11 a strong decline is shown , of the values of the abundances of lithium called Li-dip, in the range 6600 $<T_{eff}<$6900 K [Boesgaard & Tripicco (1986)]. As for lithium, for beryllium was also observed a strong decrease of abundances called (Fig 1.12), again, Be-dip and it is observed at the same temperature range of lithium. From this behavior it follows a similar strong correlation between the two elements [Boesgaard & Tripicco (1986)].

The comparison of the Li and Be abundance as a function of T_{eff} can be seen in figure 1.13. The Be scale is shown on the left y-axis and the Li scale is shown on the right y-axis, the scale size is the same, and they are normalized to the meteoritic abundances of Li, A(Li)=3.31 and A(B)=1.42 [Anders & Grevesse (1989), Grevesse & Sauval (1998)].

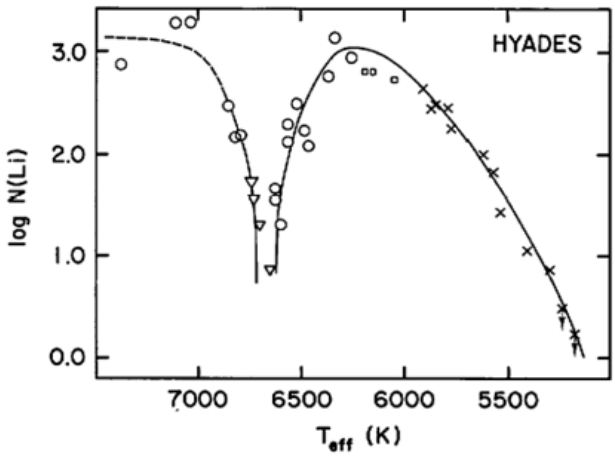

Figure 1.11: Abundance of lithium as a function of T_{eff} for the Hyades: we note the existence of Li-dip in the range 6600K<T_{eff}<6900K .

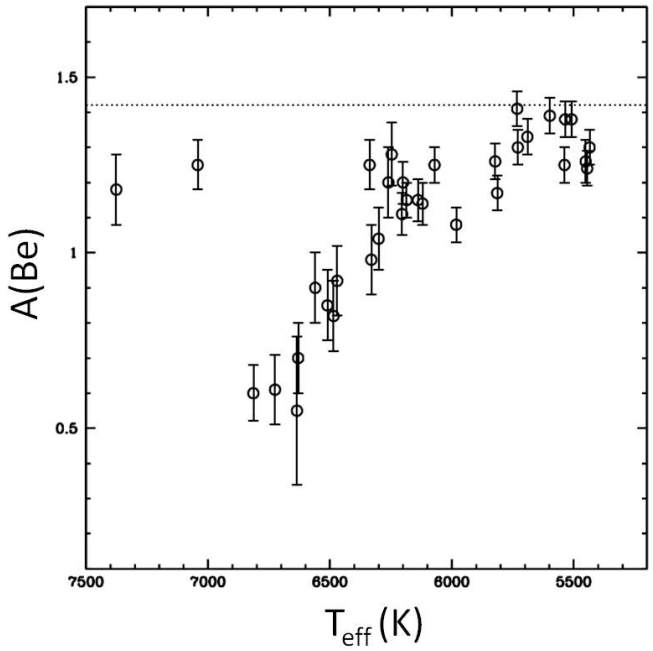

Figure 1.12: Abundance of Be as a function of T_{eff} for the open cluster of Hyades. Note the Be-dip [Boesgaard & King (2002)].

The peak for Li is near 6200 K, and it falls off to both hotter temperatures,

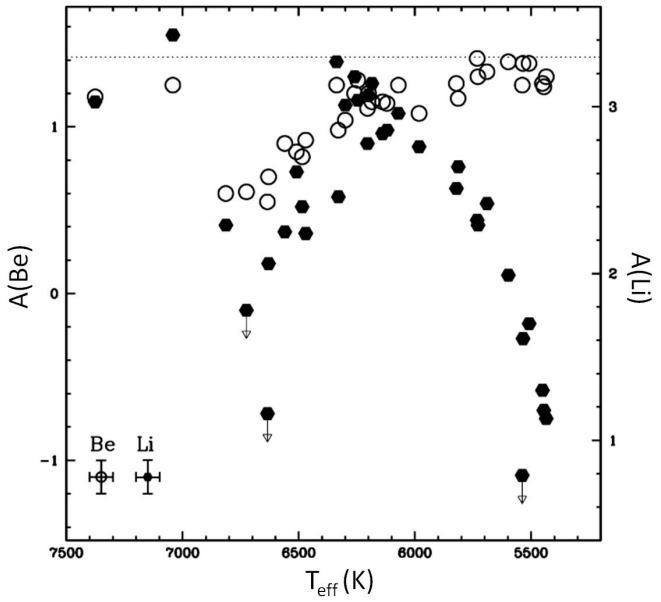

Figure 1.13: Abundances of Li and Be as a function of effective temperature for F and G stars in the Hyades. The circles are the Be data points, while the Li data points are the hexagons [Boesgaard & King (2002)].

the Li gap, and cooler temperatures, the well-known falloff of Li with decreasing temperature in G dwarfs. The Be profile is quite different from that of Li. In the F dwarfs there is a "Be-gap", but is not as deep as the Li gap. In the G dwarfs between 5400 and 5800 K , Be appears to be undepleted, near the meteoritic value. A similar graph is reported in figure 1.14 where is plotted both Li and Be abundances in Praesepe stars on the same scale, coincident with their respective meteoritic abundances.

The vertical shift from the meteoritic value shows the depletion amount of Li and Be. In the case of Praesepe, two hot stars are virtually undepleted in both Li and Be. The other stars are all depleted in Li. Those with severe Li depletions are also Be-depleted. Those with more mild Li depletions have only small Be depletions, if any. For the other stars the Li depletions are systematically larger than the Be depletions; this is consistent with the prediction from theories of slow mixing of the surface material down to the respective temperature of nuclear destruction of Li and Be [Boesgaard & King (2002)]. The major results

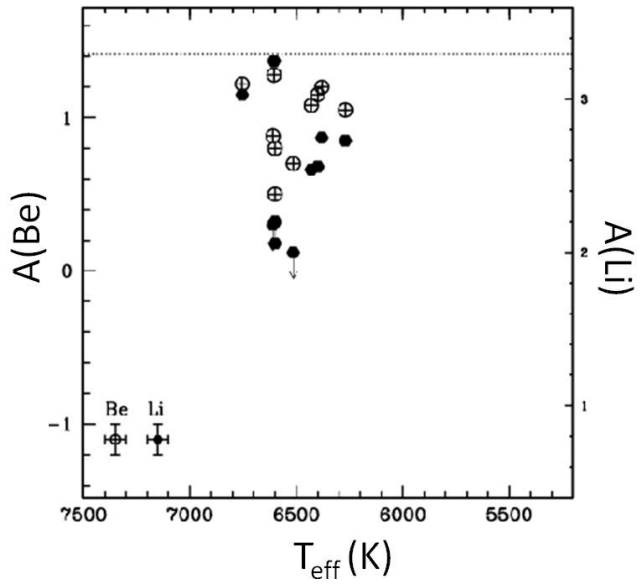

Figure 1.14: Abundances of Li and Be in Praesepe stars on the same vertical scale. The circled crosses represent the Be abundances and the filled hexagons represent the Li abundances [Boesgaard *et al.* (2004a)].

from the studies to the correlation between A(Li) and A(Be) are:

1. A Be-dip similar to the Li dip, was discovered in the mid-F stars and in the Hyades cluster, but not in the younger Pleiades cluster;

2. Be is undepleted in the G stars in all the clusters, whereas Li has undergone major depletion in the G stars;

3. the Li and Be abundances are correlated in the temperature range 5850-6650 K, which corresponds to the temperature range from the Li plateau to the bottom of the Li dip in the Hyades.

Other young and intermediate age clusters have been investigated for the presence of a Be dip and to check Be in G dwarfs [Boesgaard *et al.* (2003)], it was observed looking at younger Pleiades and αPer clusters that there is no evidence of a Be-dip in this clusters which are 50-50 Myr old (Figure 1.15). This indicates that the Li-Be dip is a phenomenon that occurs on the main sequence, after $\sim$100 Myr old, and not during the pre-main sequence evolution.

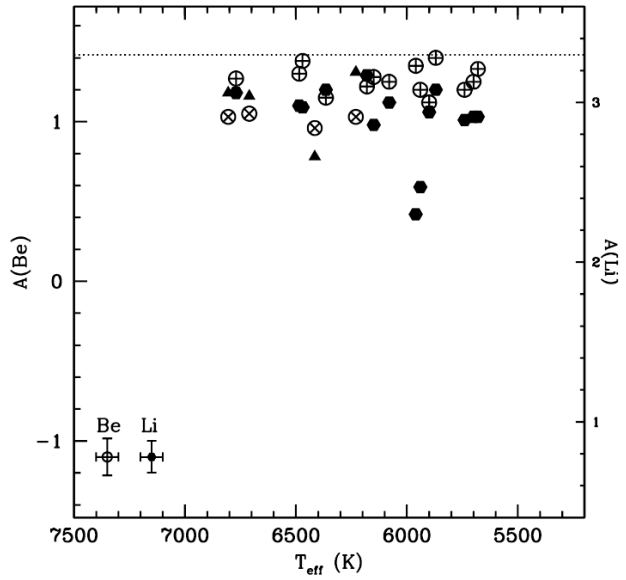

Figure 1.15: Li and Be abundances in the Pleiades and αPer samples. The hexagons shown the Pleiades Li results and encircled is the Be results [Boesgaard *et al.* (2004a)].

In order to establish whether B participates in this depletion and correlation as well, it is necessary to know the amount of B present in the Galactic disk in order to understand whether, and how much, depletion of B has occurred in main sequence stars. In addition, such information is important for the study of the chemical evolution of B, in both the Galactic halo and disk. Moreover the inclusion of B in these light element studies allows to: probe deeper into stars, search for B-depletions in individual stars and look for a Be-B correlation, which could occur in the same temperature regime and be similar to the Li-Be correlation. Boron is more resistant than either Li or Be. the complementary information from B observations can thus potentially provide additional, very powerful constraints. In order to study B in the Galactic disk [Boesgaard *et al.* (2004a)] used HST + STIS to obtain spectra of the BI line at 2497 Å in stars which had no depletion of Be Figure 1.16.

Since the be abundance is undiminished in these stars, the B abundances would be unaffected by depletion also. Both B and Be increase slowly with Fe such that as Fe increase by a factor 4, Be and B increase by a factor 1.7 the

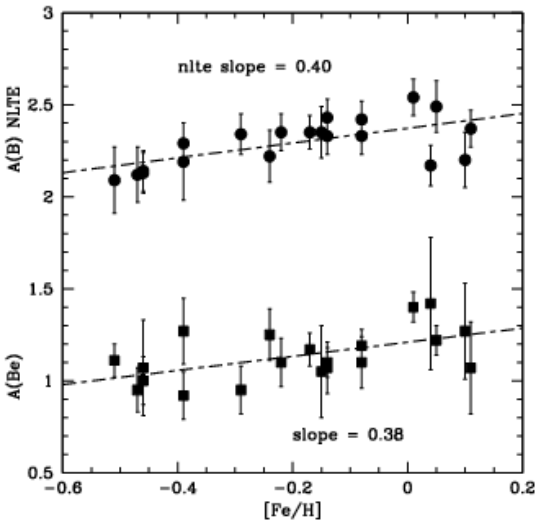

Figure 1.16: The B and Be abundances in the sample of stars with undepleted Be. There is a slope to the relationship with [Fe/H] of about 0.4 for both Be and B.

ratio of B/Be was found to be 15, with no trend with metallicity. This ratio is consistent with the prediction of spallation reactions as a source of Galactic Be and B.

1.5 Correlation among the light element Li, Be and B.

The simultaneous study of the three elements is very useful, in order to investigate the correlation between the abundances of these elements the cluster and field star data on Li and Be can be assembled [Boesgaard *et al.* (2004b)]. In fact, as already explained, although Li has been extensively observed in main-sequence field and cluster stars, there are relatively fewer observations of Be. The major goal is to examine the correlated depletion of Li and Be in the temperature range of 5900-6650 K. It possible to separate the temperature range corresponding to the cool side of the Li-Be dip, 6300- 6650 K, where Li and Be are increasing as the temperature decrease, and 5900-6300 K corresponding to the cooler group of early

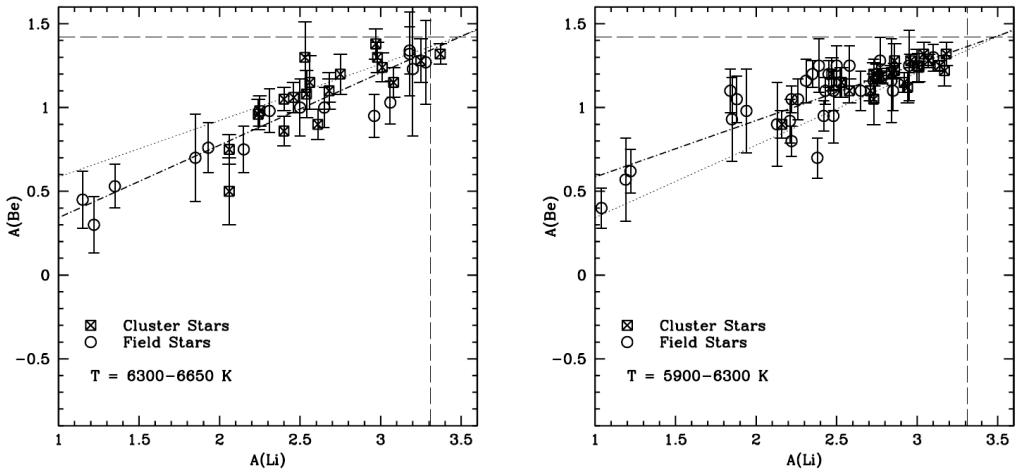

Figure 1.17: Abundances of Li and Be in two temperature ranges: 6300<T_{eff}<6650K where the decay reaches 0.43±0.04 and 5900<T_{eff}<6300 K where it reaches 0.34±0.03. The horizontal and vertical dashed lines correspond to the meteoritic Be and Li abundances respectively [Boesgaard *et al.* (2004a)].

G stars near the Hyades Li peak, 5900-6300 K. An example of their relationship is shown in Figure 1.17 [Boesgaard *et al.* (2004a)] where in the left panel it is shown the Li and Be abundances in the hotter stars which corresponds to the cool side of the Li-Be dip, while in the right panel there are the Li and Be abundances in the cooler stars 5900-6300 K. Moreover in the figure 1.18 A(Be) against A(Li) is plotted for stars from different young clusters in all the temperature range of interest 5900-6650 K.

A major result of these studies is the correlation between A(Li) and A(Be) in a specific temperature region; the stars that fall within 5900-6650 K show a relation that has a slope of 0.43±0.05, in the sample of stars that is considered the stars actively depleting both Li and Be, this is the meaning of the slope in the figure. So is evident that the abundances of Li and Be are found to be correlated in such stars with Li being more depleted than Be. For this stars the relationship is A(Be)=0.382(±0.030), A(Li)=0.105(±0.078) [Boesgaard *et al.* (2004a)]. When Li has decreased by a factor of 10, Be has decreased by only a

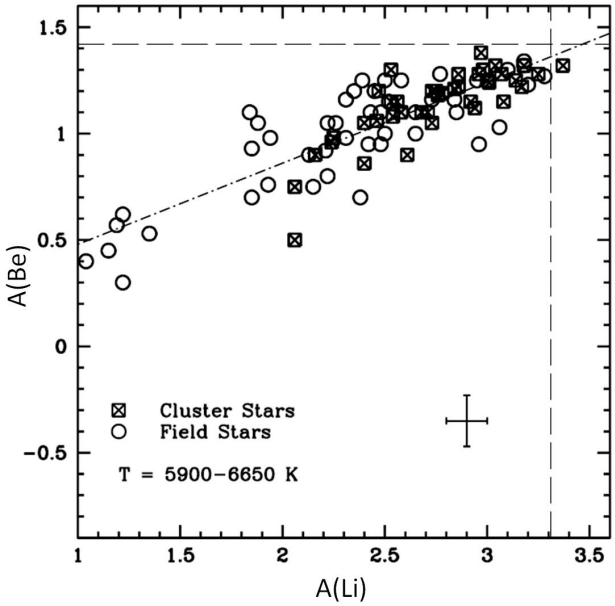

Figure 1.18: Li-Be correlation for hot stars from different clusters in the temperature range between 5900-6650 K. The horizontal and vertical dashed lines represent the meteoritic Be and Li [Boesgaard *et al.* (2004a)].

factor 2.4. This relationship is very well matched by the predictions of models with rotationally-induced mixing (see next section). Moreover it is also important the Li/Be ratio studied in the young clusters in particular very interesting is the study of the Hyades [Boesgaard *et al.* (2001)]. In recent years there has been a interesting correlation between Boron and Beryllium similar to the Lithium-Beryllium correlation first discovered by [Deliyannis *et al.* (1998)] and advanced by additional observations of [Boesgaard *et al.* (2001)]. In order to examine this correlation the observation was restricted to the temperature range 5900-6650 K as was done for the Li-Be correlation [Boesgaard *et al.* (2004a)].

The HST/STIS observation study of B focused on stars with large Be depletions to try to find stars that were depleted in B, Fig 1.19 shows the interesting correlation of Be and B similar to the Li-Be correlation.

The relationship between B and Be is A(B)=0.175($\pm$0.058), A(Be)=2.237($\pm$0.055) [Boesgaard *et al.* (2004a)] the slope is shallower than that between Li and Be correlation because the B preservation region is larger. This can provide clues about

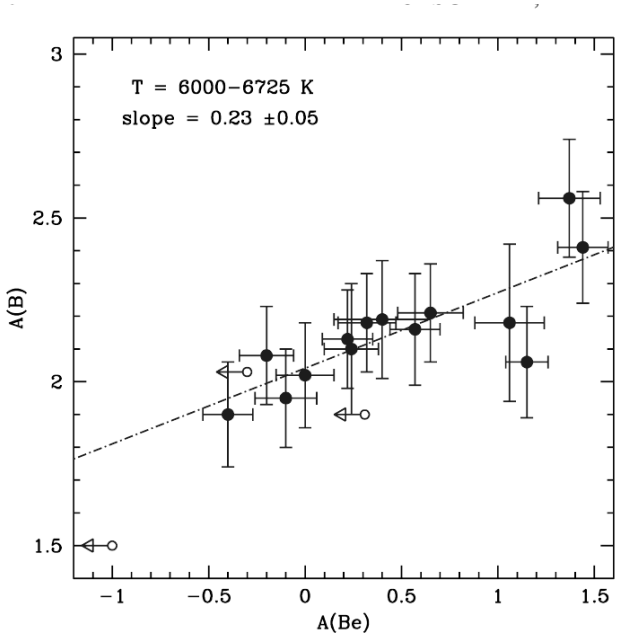

Figure 1.19: Correlation between the abundances of Be and B for a sample of stars, we note that this correlation is similar to the Li-Be. Most of stars have moderate to severe Be depletions and show accompanying mild to moderate B depletions [Boesgaard *et al.* (2005)].

how the mixing changes with depth. The B atoms have to be circulated to greater depths to be destroyed and therefore B is the less susceptible to destruction. Predictions for B depletion have not yet been made, but it seems likely that rotational mixing will be a key ingredient in the small Be depletions. Also in this case the B/Be ratio is very interesting, considering the stars that has their surface Be abundances assumed to be undepleted, the severity of depletion is expected to decrease from Li to Be to B. Thus, the B to Be ratio should be the ratio present in the stars natal cloud, and a such, it holds clues to the origin of Be and B. The results obtained for the B/Be ratio are consistent with the production of Be and B by spallation induced by relativistic GCRs. Theoretical production yields of Be and B from spallation for a variety of composition and energy spectra of cosmic rays and composition of the interstellar medium are presented by [Ramaty *et al.* (1997), Lemoine *et al.* (1998)].

For example, for solar composition it is find B/Be =15±5, near the mean

ratio obtained for the stars with different metallicity 14.5^{+7}_{-5}. So except for the discrepancy between the solar system's $^{11}B/^{10}B$ ratio (=4.02) and the prediction for spallation by relativistic particles ($\simeq$2.5) synthesis of B and Be may be ascribed to spallation [Lambert *et al.* (1998)].

1.5.1 Boron in lithium and beryllium deficient F stars.

It is very interesting to define and interpret the deficiencies of Li, Be and B. To define a deficiency, the initial abundance must be inferred for each star, this inference is normally made from the meteoritic abundance. Solar photospheric abundances are inappropriate as reference values because Li and possibly Be have been depleted, and the B abundance is poorly determined being based on the strong and blended BI 2496.8 Å line [Boesgaard *et al.* (1998)]. Lithium is so highly prone to alteration of its surface abundances that it is difficult to determine how the initial Li abundance varies with metallicity. If the maximum Li abundance at a given [Fe/H] is identified as the initial Li abundance for that [Fe/H], the initial Li abundance increases with increasing metallicity. Moreover the Li plateau abundances in young open cluster, which are presumably minimally depleted are also in agreement with the meteoritic abundance.

Regarding Be, extensive data on Be abundances in main sequence F and G stars have been provided by [Boesgaard (1976)]. The Be abundance at [Fe/H]=-1 is less than the meteoritic value [Be/H]=-0.5 [Boesgaard *et al.* (1998)]. Near [Fe/H]=0, Be abundance increase only very slightly with [Fe/H]. Moreover, the Be abundances of disk stars vary from star to star with an approximate amplitude of 0.8 dex at [Fe/H]=0 for stars that have not significantly depleted their Li. If this reflects a real variation of the initial Be abundance, there is clearly no point in making the much smaller adjustment to the adopted initial Be abundance for our stars spread over a small range in [Fe/H]. There is no correlation between the B abundance and variables such as effective temperature, [Fe/H], and the Li and Be abundances. In particular, the B abundance is unchanged as Li and Be are depleted.

1.6 Depletion of Li Be B

Evaluation of Boron abundances, when combined with our current knowledge of Li and Be, can improve the understanding of nucleosynthesis of the light element and their depletion mechanism in stars. In fact it is useful to represent the three together in order to understand the major difference and similarity between these elements. Moreover, the "trio" of light element, Lithium Beryllium and Boron, offers a special opportunity to discern the structure and processes occurring beneath the surface of stars. It has long been recognized that the light elements can be used to constrain the amount of mixing that takes place in stellar radiative zones. The three dominant isotopes of each of these element are susceptible to destruction in stellar interior by nuclear fusion reactions;some of these reactions are of the type (p,α),(p,γ),(α,n) and (α,γ).

The destruction of these elements take place at different depths inside stars corresponding at relatively low temperatures near 2.5×10^6 K for Li, 3.5×10^6 K for Be and 5×10^6 K for B, so they can survive only in the convection zone and outermost layers of the radiative core in main-sequence stars of solar mass. Thus, observations of the surface abundances of these elements provide information about mixing in the outer portion of the stellar radiative interior. If differential rotation in this region gives rise to instabilities and hence to turbulent mixing, then these observations may also provide information on the internal rotation of solar-type stars Considering one-solar mass star, as illustrated in Figure 1.20, only the outer shell of 2.5% by mass contains Li, only the outer 5% contains Be while the outer 18% has B. It consists of an outer layer directly observable in contact with a convective envelope chemically homogeneous.

Figure 1.21 shows the expected profiles of light-elements abundances in a solar model, in which only nuclear reactions have altered the abundances. The aforementioned extreme sensitivity of the light elements to proton capture reactions cross section translates into step like abundance profiles, with the abundances going from undepleted to zero over a very narrow temperature interval. These temperatures occur at depths of $r/R_\odot$ 0.54, and 0.4, respectively. Clearly, a near-normal beryllium abundance and a lithium depletion by a factor of 200 (see, e.g. [Anders & Grevesse (1989)]) impose a limit on the spatial extent of the region

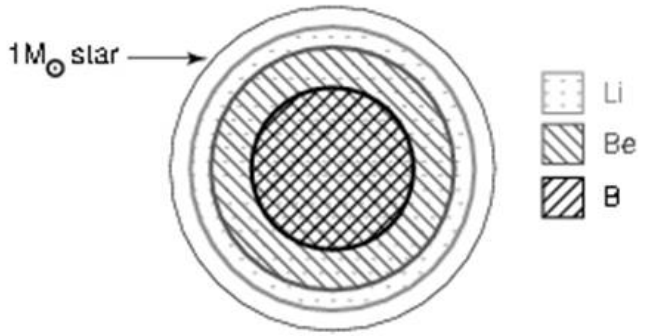

Figure 1.20: One-solar mass model showing the region were all the Li has been destroyed, a smaller sphere where there is no Be , and a still smaller one that is devoid of B [Boesgaard *et al.* (2004a)].

below the solar convective envelope in which mixing acts efficiently. From the bottom of the convection zone, mixing must be efficient down a distance of at least 0.1 $R_\odot$ but not more than 0.15-0.2 $R_\odot$. Alternatively, the mixing region must include material within at least 1 scale height of the base of the envelope, but less than 2. This represents an extremely stringent constraint on any global mixing mechanism operating in the upper portion of the solar radiative interior; the timescale over which mixing occurs must increase rapidly with depth.

The light elements can be circulated by various mixing mechanism to the stellar interior down to the temperatures where they are fused into other nuclear products. Among the most common proposed mechanism are convection, microscopic diffusion, instabilities related to rotation, turbulence, gravity waves, and meridional circulation. In addition, sufficient surface mass loss can rid a star of the surface layer where the light element had been preserved. The surface zones in which each element is preserved have different dimension; the amount of each element remaining on the stellar surface indicates how deep the mixing has been. A presentation of the results is given in Fig 1.22 to highlight how B differs so remarkably from Li and Be. The stars are ranked by their Be abundances. Deficiencies are calculated relative to meteoritic abundances for Li and Be, the deficiencies are plotted against the progressive number of the stars. The steady growth of the Be deficiency whit ranking is not matched by a B deficiency. In fact

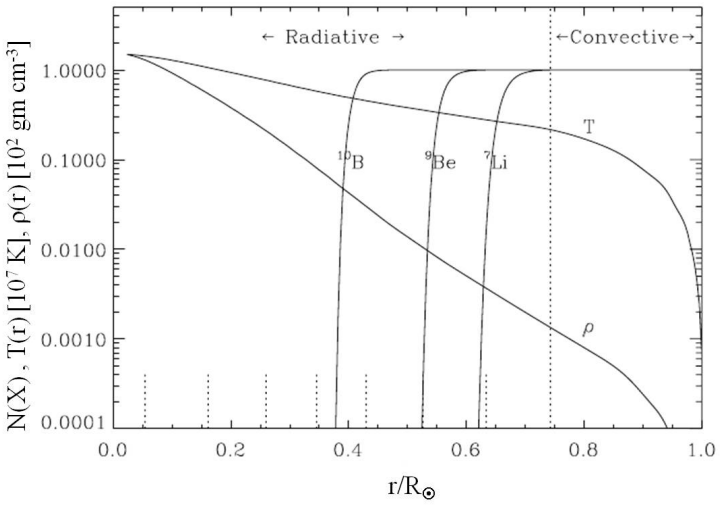

Figure 1.21: Expected variations with depth of the abundances of lithium, beryllium and boron in a solar model, in the absence of any kind of mixing in the radiative interior. All abundances are normalized to their value on the ZAMS. The extreme temperature sensitivity of the (p,α) nuclear reactions responsible for the depletion of the light elements leads to step like abundance profiles. The base of the convective envelope is located at r/R$_{\odot}$ where the temperature is T 2×10^{6} K. The dotted tick marks along the lower x-axis are separated by one density scale height, working downward from the base of the convective envelope [Barnes *et al.* (1999)].

it possible to observe a strong depletion for lithium, a very less evident depletion for Beryllium and a trend approximately constant for Boron. The constancy of the Boron abundances in most of the stars is rather striking in view of the large variations in Li and Be, which range from nearly normal (meteoritic) to severely underabundant. Whatever mechanism is responsible for these large Li and Be depletions has apparently left B unaffected.

1.6.1 Combustion of light element

When a star contracts from interstellar space and the central temperature increases, the first thermonuclear reactions to set in are those which destroy deuterium. The ratio of abundances of deuterium and hydrogen in the earth and

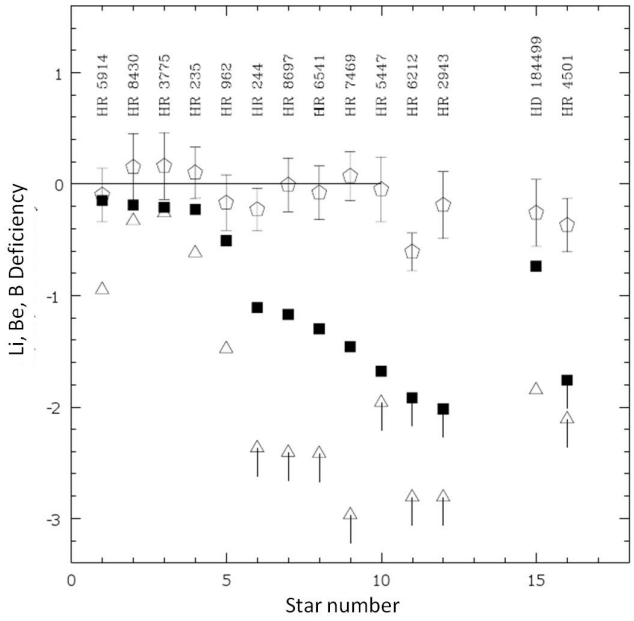

Figure 1.22: Deficiency of Li, Be and B plotted in order of Be deficiency. The open pentagons are B deficiencies, the filled squares are Be deficiencies, and the open triangles are Li deficiencies [Deliyannis *et al.* (1998), Boesgaard *et al.* (2004a)].

meteorites about 1.5×10^{-4}; hence the deuterium does not provide one of the major source of energy for the stars. Nevertheless, the energy obtained from the deuterium reactions is comparable to the energy obtained from the gravitational contraction of the star, and the deuterium consumption stage must have a profound influence on the details of the stellar model in the contraction stage. Deuterium can be destroyed both by direct proton capture and in reactions with other deuterium nuclei, for example in a red dwarf star on the main sequence, the deuterium will be destroyed a temperature of about 0.5×10^6, in the sun it was destroyed at a temperature of about 1×10^6 and in a very hot main sequence star of population I the destruction will occur at a temperature of about 2×10^{-4}.

The D(p,γ) He^3 reaction predominates except in the hottest stars, and even in hottest stars the D-D reactions provide effective competition only at the beginning of the deuterium destruction when the deuterium concentration has nearly its initial value. Nevertheless some neutrons and some triton will be produced by D-D reactions.

Nuclear reactions	Temperature(keV)
^{6}Li(p, α)^{3}He	$>2\times10^{6}$
^{7}Li(p, α)^{4}He	$>2\times10^{6}$
^{9}Be(p, α)^{6}Li	3.5×10^{6}
^{10}B(p,α)^{7}Be	5.3×10^{6}
^{11}B(p,α)^{8}8e	5.3×10^{6}

Table 1.2: Mainly nuclear reactions responsible to the destruction of LiBeB in stellar interior.

After the exhaustion of deuterium, a star will continue contracting and its central temperature will continue rising. In succession the element lithium, beryllium and boron will be destroyed. As largely described before, these elements are mainly burning through (p,α) reaction at temperature of the order of 10^{6} K through the reaction summarized in table, this temperature are reached from a stellar object during the first stage of evolution, before that the main energy source, the so called pp-chain [Castellani (1981)]. Moreover, because of the low value for the p+p$\rightarrow$D+e^{+}+ν cross section (10^{-20} barn), that represent the first step of the pp-chain, the channel is largely inhibit respect to the burning reaction involving Li, Be and B: once that the temperature will be greater than $\sim6\times10^{6}$, the number of reactions that process two proton in a deuteron will be increased and the pp-chains reactions will be efficient.

The abundances of these element are so small that the energy produced during their destruction are so small compared to the energy released in the gravitational contraction or from deuterium fusion. Nevertheless, the above discussion on the light element shows as these element are of crucial importance in the development of a deeper understanding of some process acting inside the stars.

Figure 1.23 shows the main channels of the combustion of three elements. The interest of these combustions lies mainly in the fact that they allow to probe the history of the convective envelope of a stellar structure.

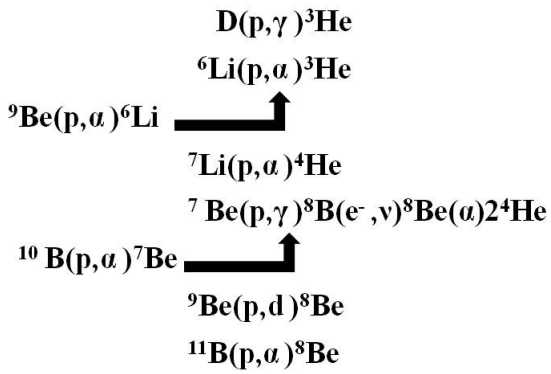

Figure 1.23: Main channels of the combustion of light elements, [Castellani (1981)]; these elements does not influence the production of energy in the stars but can be used to extract information about the stellar structure.

Indeed, the greater the depth reached by a convective envelope, the higher the temperature at the base of the convective zone where the elements are exposed in continuous mixing, therefore expected that with increasing temperatures in the order disappear from the atmosphere D, Li, Be, B.

1.6.2 Depletion models

The light element LiBeB, are useful probes of the regions beneath the surface convection zone in cool, main sequence stars. The degree to which Li, Be and B are depleted from a stellar atmosphere serves as a subtle tracer of internal stellar kinematics. Physical processes may either remove the fragile "trio" from contact with the surface convection zone or destroy them outright. Standard stellar evolution models, which ignore complications such as magnetic fields, mass loss, rotation etc., suggest lithium survives only in the outermost layers of a typical F dwarf [Pinsonneault *et al.* (1990)]. At greater depths, thermal protons easily destroy it. However, the bottom of the surface convection zone in main sequence F star is far too shallow to drag Li beneath this "destruction depth".

Superficial Li abundances in an ordinary F dwarf should therefore resemble its "Li of formation", but some F stars exhibit a significant Li deficiency with respect to an assumed initial abundance. In particular, a Li abundance gap, appears to form and strengthen during the main-sequence lifetime of galactic cluster and

field stars [Michaud & Charbonneau (1991)]. Subsequent to the discovery of the Li gap and the realization that the standard model may lack some fundamental physical principles [Boesgaard & Tripicco (1986)], several possible explanations for the dip were been made [Michaud *et al.* (1986), Garca Lopez & Spruit (1991), Schramm *et al.* (1990), Charbonnel *et al.* (1988), Pinsonneault *et al.* (1990), Vauclair (1988)]. Beryllium, like Li, is a fragile atom easily destroyed by nuclear reaction in the interiors of F and G stars. The fragility of Be makes is a useful probe of the dynamics linking the surface convection zone and the depth of nuclear destruction because the physical processes acting to deplete Li in cool stars may also affect superficial Be concentrations.

In order to study the depletion of the light element the attention is focused on F and G stars. F and G dwarfs possess certain structural similarities. The observable surface of layers are in contact with the chemically homogeneous and rapidly mixed convective envelope. Between this surface convection zone (SCZ) and the depths of nuclear destruction lies a stable of radiative layers that acts as light element reservoir. Communication between the SCZ and the interior layers, via bulk material flows, may result in surface abundances changes. Standard stellar evolutionary models of low-mass main-sequence stars, however have a SCZ completely decoupled from the depths of nuclear destruction [Bodenheimer (1965) D'Antona & Mazzitelli (1984)].

These models do not predict significant light element deficiencies apart from some pre-main-sequence Li burning. However, the base of the SCZ in G stars occupies a large fraction of the Li preservation region; thus, these cool dwarfs may suffer Li depletion associated with convective mixing. In contrast, the Be preservation region is much larger than the depth of the convective envelope in G stars, so Be burning at the base of the SCZ is not predicted. Although some Li burning associated with convective mixing may occur in the coolest of the stars, explaining the observed Li and Be underabundances in F dwarfs certainly incorporating additional physics onto the canonical model.

While measurements of Li alone may be used to discriminate between scenarios more powerful constraints become available when more than one light element is considered simultaneously. Beryllium and Boron because they are more resistant than Li in stellar interiors, serve as a tracer of the bulk motion occurring

at depths beneath the radius of Li destruction. Therefore Be and B observations can, lift the model degeneracy and assist in isolating the physical mechanism responsible for light element deficiencies [Deliyannis *et al.* (1995)]. In the following the fundamental type of mechanism proposed as the cause of the observational trend for Li Be and B will be describe [Boesgaard *et al.* (1998) Stephens *et al.* (1997)].

1.6.2.1 Standard model: convective transport.

The energy produced by thermonuclear reactions in stars is produced in their deep interior because only there are the pressures and temperatures high enough to sustain thermonuclear reactions. However, most of the luminous energy of stars is radiated from the thin region at the surface that we call the photosphere. Energy in a star is transported to the surface through one of two mechanisms: radiative diffusion and convection. A third mechanism, thermal conduction, is unimportant in stars. For most stars, both radiative diffusion and convection are at work. For instance, in a star smaller than the Sun, energy is transporting through the core by radiative diffusion, but energy is transported through the outer by convection.
In contrast, in a very massive star, energy is transported through the core by convection, and it is transported through the outer layers by radiative transport. These two transport mechanisms have a second important impact on stellar structure: when convection is present, the elements in that layer are uniformly mixed, but when radiative diffusion is present, the elements in a layer become stratified, particularly if nuclear fusion is occurring in this layer. For all three the energy flux is governed by the temperature gradient.

In general, energy flows from hotter places to cooler places. The temperature gradient in a star determines the rate at which radiative diffusion transports energy out of a star. If this gradient becomes steep enough, the plasma in this region becomes unstable to convection. Convection therefore sets a bound on the temperature gradient in a star. Because convection imposes a constraint on the temperature gradient, it imposes a limit on the amount of energy transported by the diffusion of radiation; convection is the dominant mechanism for transporting

energy in convectively-unstable regions. Thus, in convection, masses of relatively hot gas are physically moved from the hotter regions to the cooler regions as cooler gas moves into the hotter regions and energy moves upward, whereas the mass of matter of each level stays the same as time goes by [Rolfs & Rodney (1988)].

1.6.2.2 Mass Loss.

Mass loss is the simplest among the proposed non-standard depletion models. The surface convective zone SCZ in F star models is much shallower than the Li preservation region, which has boundary below which no Li is preserved. A stellar wind slowly removes Li and Be rich material from the surface of F stars which erodes the Li preservation region. Once the SCZ penetrates the nuclear destruction zone NDZ, Li-poor material is mixed into the superficial layers, which dilutes the photospheric Li concentration. However, because the relative depth of the NDZ for Li (2%) and Be (7%) is well separated in F stars, the Li reserve may be depleted by 5- 12 order of magnitude before 'significant' Be deficiencies occur.
Figure 1.24 displays the calculated Li and Be abundances in our solar metallicity sample as a function of effective temperature. This figure also confirms the result of other studies [Deliyannis & Pinsonneault (1993), Garca Lopez *et al.* (1995)] which show that stars cooler than 6000 K may exhibit moderate Be deficiencies. If Be should not be depleted in an atmosphere that contains an observable amount of Li, then mass loss would be hard pressed to account for the observed abundance trends. However, using late G stars to constrain mass-loss models is less robust than the aforementioned F stars data since small Be deficiencies are predicted by some mass-losing solar models [Boothroyd *et al.* (1991)].

Of course, the standard arguments against mass loss still apply. The onset of Li depletion should be fairly rapid once the SCZ intersects the radius of Li destruction. Observation of open cluster suggest that Li depletion is a slow, progressive phenomenon that continues throughout the main sequence lifetime of F and G stars [Michaud & Charbonneau (1991)]. Then any measurable deficiency of Be can occur only after all the Li is already gone, but F stars show that Be

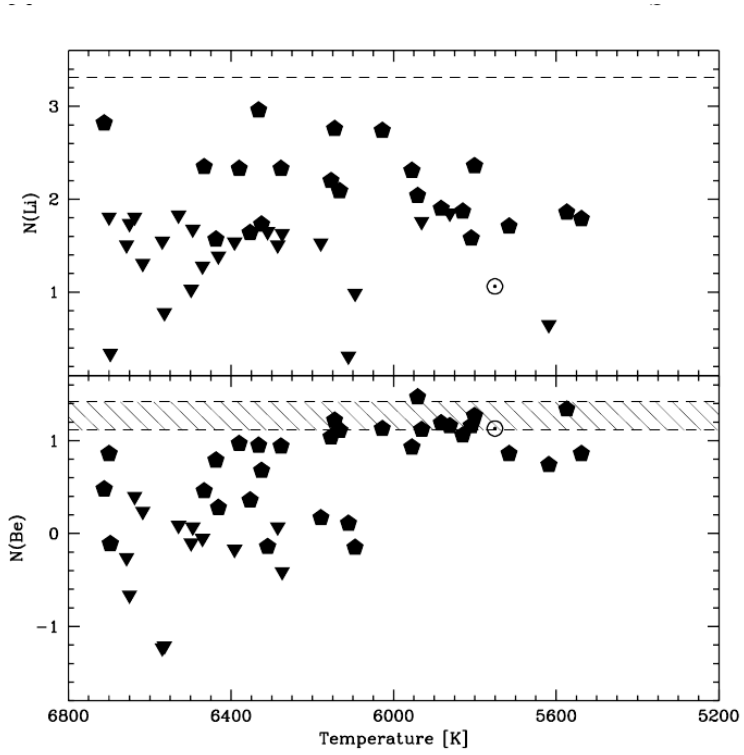

Figure 1.24: Lithium and Beryllium abundances for the solar metallicity sample are plotted vs. Temperature. Pentagons represent detections while inverted triangles denoted abundance upper limits. Shaded region bordered by dashed horizontal lines reveal the plausible range of initial abundance for each element [Stephens *et al.* (1997)].

depletion occurs while Li is still present. Although the B data alone are not consistent with mass loss, the mass loss scenario is strongly argued against Li and Be data [Deliyannis & Pinsonneault (1993), Stephens *et al.* (1997)]. The reasons for this are as follows. In conclusion, evidence for: (1) simultaneously detected, but depleted, Li and Be in F stars, (2) slowly developing Li deficiencies in open clusters, and (3) intrinsic abundances dispersion in open clusters argue against main-sequence mass loss as the cause of Li and Be depletion [Stephens *et al.* (1997)].

1.6.2.3 Microscopic Diffusion

According to model of microscopic diffusion [Michaud *et al.* (1986), Richer & Michaud (1993)], several competing force, which includes gravitational settling, thermal diffusion, and radiative levitation (outwardly directed), can cause the trace elements Li, Be and B to sink or buoy in the radiative regions beneath the surface convective zone. In the absence of turbulence, which can severely retard these diffusive motion, the dominance of one process over the other two may result in a flow of material either into (if either gravitational settling or thermal diffusion dominate) or out of (if radiative acceleration prevails) the surface convective zone.

Consequently light element abundances anomalies may develop. However the relative efficiency of these various diffusive processes is sensitive to the predominant ionization state of the atom under consideration that, in turn, is a function of temperature beneath the SCZ [Michaud & Charbonneau (1991)]. Thus the depth of the SCZ, which increase dramatically from early F to mid G stars, will significantly affect both the direction and rate of light element diffusion. The diffusive properties of both Li and Be are predicted [Richer & Michaud (1993)] in evolving, non rotating models that suffer neither internal turbulence nor superficial mass loss.

These models are not greatly dissimilar with the diffusion theory described by Michaud *et al.* (1986). Above a certain threshold temperature (6900 K for Li, 6700 K for Be), the push of radiative forces on Li and Be at the base of the convective envelope exceeds the local gravity and results in a flow of these elements into the SCZ. Consequently, the radiative buffer zone, the region between the nuclear destruction zone and the base of the surface convection zone, is drained of its light element reserve, while the SCZ light element concentration increase. Therefore, lithium and beryllium abundances concentration in excess of the cosmic level are predicted for late A and early F stars. In stars with progressively smaller T_{eff}, the temperature at the base of the deep convection zone increases rapidly, thus Li and Be become fully ionized. These bare nuclei, with smaller geometrical cross section are incapable of being supported by radiation pressure.

Therefore Li and Be leak out of the SCZ and are no longer in physical contact the surface layers. Superficial light element underabundances consequently develop. Models of microscopic diffusion predict stars cooler than 6200 K contain a SCZ so massive (SCZ mass increase with decreasing T_{eff}) that the timescale required to significantly deplete the convective envelope is comparable to an evolutionary timescale [Michaud *et al.* (1986)]. Thus, the superficial Li and Be concentration in late F and early G stars is expected to remain at or near the cosmic level for as long a these stars remain on the main sequence. So when Li and Be are considered together, the case against diffusion is even stronger. Similarly, the B data are inconsistent with diffusion as discussed in [Boesgaard *et al.* (1998)]. In fact in completely stable radiative layers sufficiently deep in the model stellar interior, Li and Be (and presumably B) diffuse downward via gravitational setting and thermal diffusion at roughly similar rates. At about T_{eff} =6700 K, the base of the SCZ is sufficiently shallow (cool) so that Li retains an electron; Li can thus be radiatively accelerated into the SCZ, enriching the surface abundance. Be retains an electron at a slightly higher temperature, or near the base of a deeper convection zone, so Be enrichment is predicted to begin at about 6600K. Like Li, Be and B also rise initially and then plummets according to the theory. Presumably this pattern repeats for B, so B enrichment might begin above roughly 6500 K. Below 6500 K, all three elements should show similar depletions. The surface Li abundance is depleted faster than the surface Be abundance [Deliyannis & Pinsonneault (1993)], and even thought Li and Be vary by orders of magnitude, B is constant. Boron abundances remain nearly constant even above T_{eff} =6500 K, where large variations in B might be expected. Thus, when considered together with Li and/or Be data, the B data also argue against diffusion as the dominant mechanism.

1.6.2.4 Slow Mixing

Various type of slow mixing have been proposed as the origin of the Li gap. These include wave-driven mixing [Garca Lopez & Spruit (1991)] and mixing related to rotation, such as meridional circulation and instabilities triggered by differential rotation with depth [Charbonnel & Vauclair (1998), Pinsonneault

et al. (1990); Zahn (1992); Charbonnel *et al.* (1994)]. The efficiency of wave mixing would increase with shallower SCZs, creating the cool side of the Li gap, and decrease with still shallower convection zones, creating the hot side. Rotation, a fundamental property of most stars, greatly complicates the calculation of stellar structure and evolution. Turbulence resulting from shear flow instabilities, a consequence of meridional circulation, was explored as a possible cause of Li deficiencies in main-sequence F stars [Vauclair (1988)]. However, various models have merged a prescription of turbulent mixing with realistic models of evolving stars [Pinsonneault *et al.* (1989), Pinsonneault *et al.* (1990), Charbonnel *et al.* (1992),Charbonnel *et al.* (1994)].

The rotation scenarios produce the cool side as a result of the increase in rotation with mass. The hot side is more challenging, since rotation rates continue to increase. The Charbonnel *et al.* (1988) scenario relies on upward radiative levitation plus finely tuned mass loss to counter the surface mixing, though it is not clear that this scenario is still viable in view of the improved diffusion calculations [Richer & Michaud (1993)]. The scenario of Vauclair (1988) and Charbonnel *et al.* (1992) rely on the splitting of circulation into two distinct cells for very shallow convection zones, although other complications (such as due to diffusion) argue against this [Zahn (1992)]. Of relevance may be the occurrence of the break in the rotation curve [Kraft (1967)] at the same T_{eff}as the Li gap. Below the break, stars are inferred to spin down during their lifetime, above they do not. Hence, the hot side of the gap may reflect the absence of mixing, either because the lack of angular momentum loss can no longer cause mixing or perhaps because the lack of a torque allows the establishment of a circulation-free state.

Figure 1.25 shows the model proposed in [Stephens *et al.* (1997)] where the morphology of light element depletion N(Li)and N(Be) vs. T_{eff} are superimposed on theoretical calculations; these models reproduce the shape of the observed Li and Be depletion curves. The signature of simultaneous Li and Be depletion would appear to be the normal depletion pattern for F stars [Stephens *et al.* (1997)].

Distinguishing between different scenarios for slow mixing is a bit more challenging but can potentially be accomplished by understanding 1) the timing of

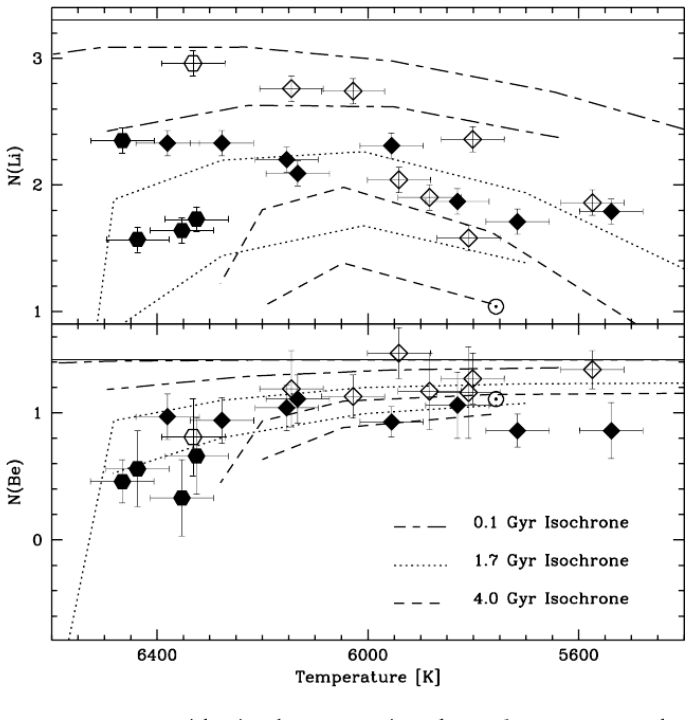

Figure 1.25: Stars with simultaneous Li and Be detection are shown in this abundances vs. T_{eff}. as [Deliyannis *et al.* (1998)] predicted. Open diamonds represent stars with N(Be)$\geq$1.11, solid diamonds stars with N(Be)$\simeq$ 0.81-1.11, and solid hexagons stars with N(Be)$\leq$0.81

the light element depletions, 2) the detailed Li-T_{eff} (and ideally Be-T_{eff}) morphology in clusters and its evolution and dependence on composition, 3) the light element abundance differences at given T_{eff} and 4) the evolution of Li/Be/B ratios, which probe the relative efficiency of mixing with depth.
Although none of the slow mixing scenarios have made specific predictions for B, it is expected that the preservation of B to significantly greater depths than Be (or Li), coupled with the common feature these models have of increasing mixing efficiency toward the surface, results in a little or no B depletion. At least, much more severe Be depletion must precede measurable B depletion. The uniformity of the B abundance in most of the stars is thus consistent with slow mixing.

The B data also argue against older models of "turbulent diffusion" in which the mixing was more uniform with depth and much more severe. Future models should assess the capability of various mechanism to create B depletion. This may be difficult for the internal wave models, for which Li and especially Be depletion is already energetically difficult.

1.7 Open questions

The above discussion on light elements Li, Be and B shows as these elements are of crucial importance in the development of a deeper understanding of some processes acting inside the stars, in fact the study of the abundances of these elements can gives useful information about different mixing process that cause their depletion in external stellar layers. In this sense big effort acquires the study of the reaction involving in the destruction of these light element, mainly the (p,α) reactions that occurs at the temperature of the order of 10^6K. These elements can be used as diagnostic for mixing processes and as tracers for the internal stellar structure [Boesgaard *et al.* (2004a)].

The uncertainties that exist are different, it's important to remember those inherent to the determination of some of the basic parameters for the study of element abundances observed: the value of the effective temperature T_{eff}, and the value of the metallicity [Fe/H] [Primas *et al.* (1999)], Stephens *et al.* (1997)]. Each of these amounts, in fact, introduces different uncertainties on the final value of the observed abundances. Uncertainties are also related to models for the stellar atmosphere and evaluation of the opacity of stellar material. A further source of uncertainty is the imperfect understanding of the processes of mixing discussed above as well as the lack of a theory, an alternative to MLT (Mixing Length Theory), that manages to describe the stellar convection [Boesgaard *et al.* (1998)]. Together with this uncertainties an important role is played by the nuclear reaction rate and consequently the indeterminations values of the cross section for proton capture reactions. Usually the value adopted in the calculation are derived from experimental measurements but due to the low energy at which these kind of process occur, the rates in the energy window relevant for the astrophysics is extrapolated from measurements at higher energies. From the

discussion above, we can see how the nuclear reaction involving boron at astrophysical energies are important for nuclear astrophysics. Therefore in the next chapters we will discusses the application of the nuclear physics in astrophysics, in particular the experimental study of the ^{10}B(p,α)^{7}Be and ^{11}B(p,α)^{8}Be at the astrophysical energies.

Chapter 2

Nuclear Physics in Astrophysics

2.1 Thermonuclear reaction

In a stellar plasma, the kinetic energy for a nuclear reaction derives from the thermal motion of the participating nuclei. Hence, the interaction is referred to as *thermonuclear reaction*.
Thermonuclear reactions play a key role in understanding energy production and nucleosynthesis of the element, these reactions occur most readily between isotopes of hydrogen (deuterium and tritium) and less readily among a few other nuclei of higher atomic number. At the temperatures and densities required to produce an appreciable rate of thermonuclear reactions, all matter is completely ionized; that is, it exists only in the plasma state.

Thermonuclear fusion reactions may then occur within such an ionized gas when the agitation energy of the stripped nuclei is sufficient to overcome their mutual electrostatic repulsions, allowing the colliding nuclei to approach each other closely enough to react. So thermonuclear reactions are the primary responsible of energy production in stars, in fact when interstellar gas, mainly hydrogen and helium, condenses and, as a result of the conversion of gravitational to thermal energy, the star is born. Subsequently when the temperature and density at the center become high enough, the nuclear reactions begins whit in the most easily burned nuclear fuel, hydrogen. The energy released by the nuclear reactions stabilizes the star by fixing a balance between thermal pressure and gravitational force, without a large temperature change until the exhaustion of that particular

nuclear fuel. Then the stars contracts, and convert again the gravitational energy to thermal energy, until the temperature and density become high enough to ignite the next available fuel. So the thermonuclear reactions change the chemical composition of the stellar inner layers.
Very important is evaluation of the rate at which the thermonuclear reactions take place. The rate depend on the determination of the reactions cross-sections. In this chapter is shown which are the main theoretical problems involved in the study of nuclear reactions at astrophysical energy.

2.2 Characteristics of nuclear reactions

The production of nuclear energy and the synthesis of elements proceeds through fusion reactions until all light nuclei are converted to iron. Specific nuclear reactions can be indicated in a manner similar to chemical reaction equations. If a target nucleus A is bombarded by a particle x and results in a nucleus y with emitted particle B, this is commonly written as : $x+A \rightarrow y + B$.

Nuclear reactions are characterized in terms of energy balance by means of the Q-value, that is defined as the energy released in the reaction: Q=(m_x+m_A-m_y-m_B)c^2. Moreover the reaction is said exothermic if the Q-value is positive (the total mass of exit channel is less than that of the entrance channel), indicating that the total nuclear binding energy has increased and that the reaction occurs with energy production. If the Q-value is negative the reaction is said endothermic. The most important reaction in stars having positive Q-values.
Let us to define the *cross section* σ, as:

$$\sigma = \frac{emitted\, nuclei\, B/s}{\frac{hitting\, nucleix/s}{unit\, of\, area} \cdot (num.\, of\, target\, nuclei\, A)} \tag{2.1}$$

which has the dimensions of a surface and it is expressed in terms of *barn*, (1 barn=10^{-24} cm^2). The cross section σ represent the probability that a given reaction take place, and it is used to determine how many reaction occur per unit time and volume. It depend also on the relativistic energy of the interacting particles, $\sigma = \sigma(v)$. A more exhaustive description of the nuclear reactions in

stellar environments is given by the introduction of the *reaction rate* that describe the number of nuclear reactions for unit of time and unit of volume. The reaction rate r is defined as:

$$r = N_x N_y v\sigma(v) \tag{2.2}$$

where N_x is the density of target particle, N_y the density of impinging nuclei and $\sigma(v)$ is the relative velocity between the interacting nuclei expressed in terms of cross section. Since the motion of the nuclei can be described by a Maxwellian distribution of velocities, $\phi(v)$, the quantity $\phi(v)dv$ is the probability that the particles has a velocity between v and $v+dv$. The total reaction rate R can be written as:

$$R = N_x N_y < \sigma v > \tag{2.3}$$

where the bracketed quantity $<\sigma$v$>$ is referred to the reaction rate per particle pair.

$$< \sigma v >= \int_0^\infty \phi(v) v\sigma(v) dv \tag{2.4}$$

Moreover in stellar matter the stellar gas is in thermodynamics equilibrium and the velocities of the nuclei can be described by a Maxwell-Boltzmann velocity distribution;

$$\phi v = 4\pi v^2 \left(\frac{m}{2kT}\right)^{3/2} \exp\left(-\frac{mv^2}{2kT}\right) \tag{2.5}$$

where T refers to the temperature of the gas and m to the mass of nuclei of interest, and usually this quantity is normalized to the unit. The function $\phi(v)$ can be written in terms of energy as:

$$\phi(E) \propto E \exp(-E/kT) \tag{2.6}$$

When the energy is low, E$\ll$kT, the function $\phi(E)$ increases linearly with E and reaches a maximum value at E=kT, while when the energy is higher, E$\gg$kT,

the function decreases exponentially and asymptotically approaches zero at very high energy. Then, using the reduced mass μ of the interacting particles, the rate $<\sigma$v$>$ can be written in terms of the variables v and μ

$$< \sigma v >= 4\pi \left(\frac{\mu}{2\pi kT}\right)^{3/2} \int_0^\infty v^3 \sigma(v) \exp\left(-\frac{\mu v^2}{2kT}\right) dv \tag{2.7}$$

and in terms of the center of mass energy E= $\frac{1}{2}\mu$v^2 as:

$$< \sigma v >= \left(\frac{8}{\pi\mu}\right)^{1/2} \frac{1}{(kT)^{3/2}} \int_0^\infty \sigma(E) E \exp(-\frac{E}{kT}) dE \tag{2.8}$$

For those reactions involving identical particles the reaction rate must be corrected by introducing the Kronecker symbol δ_{xy}

$$r = N_x N_y < \sigma v > (1 + \delta_{xy})^{-1} \tag{2.9}$$

Thus the quantity $<\sigma$v$>$ is a very important input parameter for stellar models and has to be determined at astrophysical relevant velocities.

2.2.1 Mean Lifetime

Estimation on temporal abundances of the elements involved in stellar reactions can be obtained from the reactions rate knowledge. The change of abundance N$_X$ of nuclei X can be defined as:

$$\left(\frac{dN_X}{dt}\right)_Y = -\frac{1}{\tau_y(X)} N_X \tag{2.10}$$

where τ_Y(X) is the mean lifetime of nuclei X due to the interaction with nuclei Y. This change is related also to the reaction rate:

$$\left(\frac{dN_X}{dt}\right) = -(1 + \delta_{XY}) r \tag{2.11}$$

From eq. (2.9), (2.10), and (2.11) the mean life time become:

$$\tau_Y(X) = \frac{1}{N_Y < \sigma v >} \tag{2.12}$$

Then, the lifetime of nuclei X depends only on the number of destructive nuclei N_y and the reaction rate per particle pair, $<\sigma v>$. For high densities of destructive nuclei and large reaction rates, the lifetime of nuclei X can be quite short. If the environment contains a number of different destructive nuclei, the mean lifetime of species X is given by the expression:

$$\frac{1}{\tau(X)} = \Sigma \frac{1}{\tau_i(X)} \tag{2.13}$$

2.3 Charged-Particle induced non-resonant reactions

In the study of nuclear reactions in different astrophysical environments, the main features are closely dependent on the magnitude of the reaction rate (equation 2.8) that is strictly correlated to the stellar temperature. In fact in the evolution of the stars the temperatures changes, and the reaction rate $<\sigma\ v>$ must be evaluated for each temperature of interest. Because there are many different nuclear reactions involved at each stellar temperature it is very important to obtain the analytic expression for the reaction rate in terms of temperature. To do this the mathematical approach is determined by the energy dependence $\sigma(E)$ of the cross section. This energy dependence reflects the reaction mechanism involved in the process. In fact nuclear reaction mechanism can be *non-resonant* or *resonant*. Consider first the case of *non-resonant* reaction.

When the fusion reactions occurs the temperature is very high, and this high temperature is needed because nuclei are positively charged and repel each other with a force proportional to the nuclear charge. If consider two nuclei *1* and *2* with atomic number Z_1 and Z_2, for this repulsive force has the form:

$$V_C(r) = \frac{Z_1 Z_2 e^2}{r} \tag{2.14}$$

where r is the distance between them. When combined with the potential for the very strong and attractive nuclear force, which comes into play at distance equal to a nuclear radius $R_n = R_1 + R_2$, the potential (2.14) leads to an effective potential as shown in Figure 2.1, In this figure the shaded area represent a Coulomb barrier which inhibits nuclear reaction.

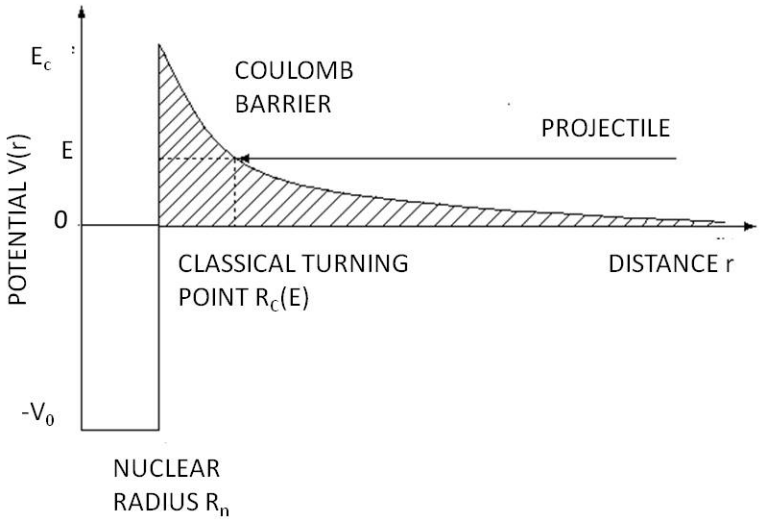

Figure 2.1: Representation of the nuclear and Coulomb potentials. A projectile incident with energy E<E_c has to penetrate the Coulomb barrier in order to reach the nuclear domain [Rolfs & Rodney (1988)].

From the classical point of view, the two interacting particles may be at distance smaller than R_n, radius of nuclear interaction. So that they will have relative energy equal at least to the Coulomb potential for that distance, that is:

$$E_C(R_n) = \frac{1.44 Z_1 Z_2}{R_n} MeV \tag{2.15}$$

This value, called the Coulomb barrier for the interaction of the two nuclei, is always of the order of MeV thus is much larger than the average kinetic energy E=kT. For example for the p-p reaction the hight of Coulomb barrier is E_C=550keV, so the p-p nuclear reaction can occur only when the energy of the protons exceeds this energy, to which corresponds a stellar temperature of T_9=6.4. If no nuclear reaction occur until this temperature is reached, which in principle is possible through gravitational contraction, then when it is reached all pairs of nuclear particle should react instantaneously and stars should experience a catastrophic explosion.

2.3.1 Tunnel Effect

Although the enormous amount of energy liberated in nuclear reactions could be the major source of energy in the sun and in other stars, the classical condition required for nuclear reactions was an insurmountable obstacle. This obstacle was removed with quantum mechanics that showed a small but finite probability for the particles with energies E<E_C to penetrate the Coulomb barrier. This phenomenon of barrier penetration is the tunnel effect that is of considerable importance in stellar burning [Gamow (1928)].

In quantum mechanics the square of the wave function $|\psi(\mathrm{r})|^2$, gives the probability of finding the particle at the position r, that in the case of the classical turning point R_C (Fig. 2.1) it is $|\psi(\mathrm{R}_C)|^2$. Classically the incident particle cannot penetrate the barrier beyond this point while in the quantum mechanics the squared wave function has a finite value at the nuclear radius R_n of $|\psi(\mathrm{R}_n)|^2$. The ratio of this two quantities gives the probability that incoming particle penetrate the barrier:

$$P = \frac{|\psi(R_n)|^2}{|(\psi(R_C)|^2} \tag{2.16}$$

For example for the p-p reaction when the energy is 1 keV, which is near the maximum of the Maxwell-Boltzmann distribution for a stellar temperature T_9=0.01, the tunneling probability P is very small, P=9×10^{-10}, but it is still sufficiently large compared with the requirement imposed i the classical limit, to account for nuclear energy production in stars. In fact for a lower stellar temperature of T_9=0.01 equation 2.5 gives that the number of particle with an energy E=550keV compared with E=kT=0.86 keV is in the ratio:

$$\frac{\phi(550)}{\phi(0.86)} = 3 \times 10^{-275} \tag{2.17}$$

That shows clearly, that the number of high-energy particles is not adequate to produce the energy radiated by stars. At low energy E $\ll$ E_c, the tunneling probability to penetrate the Coulomb barrier is given by the expression:

$$P = \exp(-2\pi\eta) \tag{2.18}$$

where η is called the Sommerfeld parameter and is equal to:

$$\eta = \frac{Z_1 Z_2 e^2}{\hbar \nu} \tag{2.19}$$

in the numerical units the exponent is

$$2\pi\eta = 31.29 Z_1 Z_2 \left(\frac{\mu}{E}\right)^{1/2} \tag{2.20}$$

where the center of mass energy is given in units of keV and μ is in amu. This approximate expression for the tunneling probability is commonly referred to as Gamow factor. The exponential behavior of the probability for tunneling determined the cross section for charged particle induced reaction droping rapidly for energies below the Coulomb barrier:

$$\sigma(E) \propto \exp(-2\pi\eta) \tag{2.21}$$

moreover the cross section depends on the de Broglie wavelenght:

$$\sigma(E) = \pi\lambda^2 \propto \frac{1}{E} \tag{2.22}$$

using both expression the cross section for charged particle induced reaction can be written as:

$$\sigma(E) = \frac{1}{E} \exp(-2\pi\eta) S(E) \tag{2.23}$$

in this equation the function S(E) contain all the strictly nuclear effect and it is called astrophysical factor. This factor is a smoothly function of energy which varies much less with energy than the cross section as shown in figure 2.2. Because of these characteristic the S(E) factor is much more useful in extrapolating measured cross section at astrophysical energies. Using the equation 2.8 and inserting the 2.22 the reaction rate is given by:

$$< \sigma v >= \left(\frac{8}{\pi\mu}\right)^{1/2} \frac{1}{(k_b T)^{3/2}} \int_0^\infty S(E) \exp\left[-\frac{E}{k_b T} - \frac{b}{E^{1/2}}\right] dE \tag{2.24}$$

where the quantity b, which arises from the barrier penetrability is given by:

$$b = (2\mu)^{1/2} \pi e^2 Z_1 Z_2 / \hbar \tag{2.25}$$

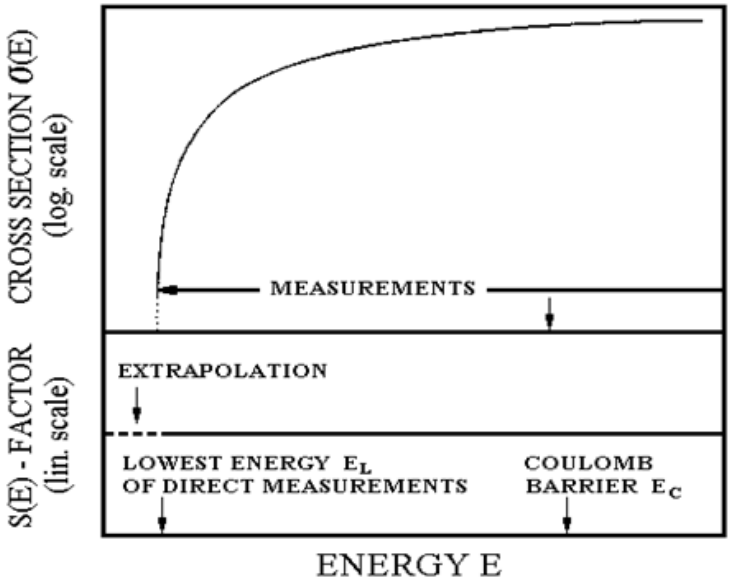

Figure 2.2: Cross section of a charged particle induced reactions drops exponentially with decreasing of the center of mass energy. This behavior is removed by using astrophysical S(E) factor that is a smoothly function of energy [Rolfs & Rodney (1988)]

The square of the quantity b is also called the Gamow energy E_G. For non-resonant reaction the S(E)-factor varies smoothly with energy, in this equation the energy dependence of integrand is governed primarily by the exponential term. The exp (-E/kT) is a measure of the number of particles available in the high energy tail of the Maxwell Boltzmann distribution, and is vanishes at high energy. The term exp ($-b/E^{1/2}$) or also exp ($-E_G/E^{1/2}$) represent the penetration through the Coulomb barrier.

2.3.2 The Gamow peak

A thermonuclear reaction can occur in a star with a probability that depends mainly on two factors. The first factor is the velocity distribution of the nuclei in the plasma and is usually given by a Maxwell-Boltzmann distribution. The second factor is the nuclear reaction cross section and contains the tunneling probability through the Coulomb barrier. Most thermonuclear reactions in stars take place at neither very low energy where the reaction cross section is very

small. Nuclear reactions in a stellar plasma will occur near energies where the product of velocity distribution and cross section is maximum.

For a given stellar temperature T, nuclear reaction take place in a relatively narrow energy window around the effective burning energy of E_0. This energy is given by the convolution of the energy distribution function (Maxwell-Boltzmann) and the quantum mechanical tunneling function through the Coulomb barrier. In fact although the Maxwell Boltzman distribution has a maximum at an energy E=kT, the Gamow factor shift the effective peak to this energy E_0 and this peak is referred to as the Gamow peak (see Fig.2.3). Frequently the S(E) factor is nearly a constant over the window S(E)=S(0)=const, for this condition the $<\sigma v>$ is given by:

$$< \sigma v >= \left(\frac{8}{\pi\mu}\right)^{1/2} \frac{1}{(k_b T)^{3/2}} S(E_0) \int_0^\infty S(E) \exp\left[-\frac{E}{k_b T} - \frac{b}{E^{1/2}}\right] dE \quad (2.26)$$

From this equation, taking the first derivative of the integrand, it possible to find the energy E_0 for which the integrand has its maximum value:

$$\Delta E_0 = \left(\frac{bkT}{2}\right)^{2/3} = 1.22(Z_1^2 Z_2^2 \mu T_6^2)^{1/3} \quad (2.27)$$

as we see E_0 depends on the temperature of particular astrophysical environment and from the charge of interacting particles, then it changes depending on the reaction considered and astrophysical environment in which this reaction takes place. For example at a stellar temperature of the order of 10^6 K the effective burning energy E_0 for some reaction is: for p+p reaction E_0=5.9 keV, for reactions involving light nuclei for example boron, $E_0(^{10}\text{B+p}) \sim$ 10.10 keV, $E_0(^{11}\text{B+p}) \sim$ 10.13 keV which corresponds at T_6=5. The maximum value of the integrand in equation is found by inserting the expression for E_0:

$$< \sigma v >_{MAX} = \exp\left(-\frac{3E_0}{kT}\right) \quad (2.28)$$

So, the rate of nuclear reaction depends strongly on the Coulomb barrier.

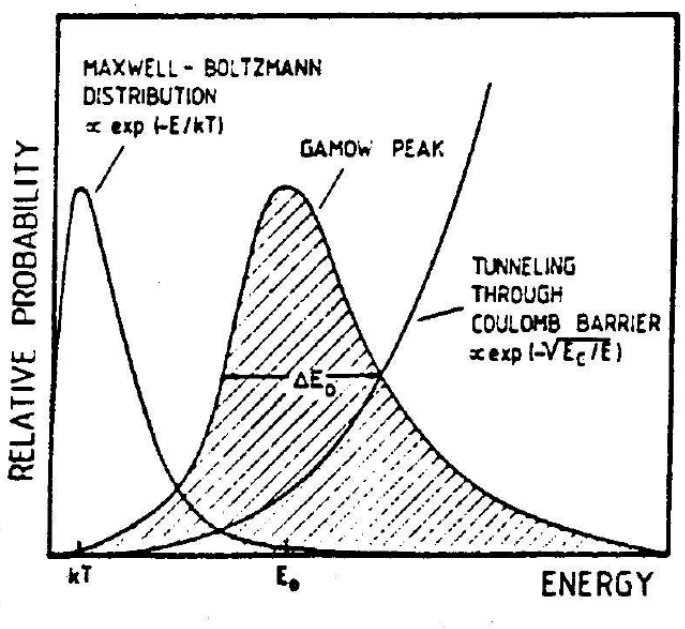

Figure 2.3: Gamow peak: is possible to observe as the energy corresponding to the peak is much greater than kT and as it is by convolution of the Maxwell-Boltzmann distribution and the probability of tunneling the Coulomb barrier.[Rolfs & Rodney (1988)]

Even if there are many species of nuclei present in a star at a particular time, those with the smallest Coulomb barrier will be consumed most rapidly and will account for most of nuclear energy generation. When the nuclei with the smallest Coulomb barrier have been consumed, a star will contract gravitationally until the temperature rises to a point where the nuclei with the next lowest Coulomb barrier can burn. The burning of this new fuel and the energy produced stabilize the star against further contraction.
These well-defined epochs in stellar evolution are referred to as the stage of nuclear burning. The existence of these epochs depends critically on the fact that the nuclear reactions rates are very sensitive to the Coulomb barrier. Approximating the Gamow peak by a Gaussian yields for the 1/E width:

$$\Delta E_0 = \frac{4}{3^{1/2}}(E_0 kT)^{1/2} = 0.749(Z_1^2 Z_2^2 \mu T_6^5)^{1/6} keV \tag{2.29}$$

The region $E_0 \pm \Delta E_0/2$ represent the effective energy window for nonresonant nuclear reactions in stars. For increasing temperature, this window shift toward higher energy and becomes broader according to equation 2.26 and 2.28. The Gamow peak strictly applies to nonresonant reactions.
Summarizing, when the Gamow peak is plotted for a given temperature, but for different target-projectile combinations, a few important observations can be made. For increasing charges Z_1 and Z_2, the Gamow peak shifts to higher energy, the Gamow peak becomes broader; and most importantly, the area under the Gamow peak decreases dramatically. In other words, for a mixture of different nuclides in a stellar plasma at given temperature, those reactions with the smallest Coulomb barrier produce most of the energy and are consumed most rapidly. This is of paramount importance for the star since it explains the occurrence of well-defined stellar burning stage.

2.4 Resonant Reactions

Resonant reactions are another type of reaction mechanisms. They can be described as a two step process in which an excited state E_r of the compound nucleus is first formed in the entrance channel, subsequently decaying to lower-lying states [Satchler (1990)]. The nucleus formed during the x+Xcollision between the incident and the target nucleus later decays to the reaction products Y and y or emitting γ radiation (Fig. 2.4). Resonant reaction can be schematized as:

$$x + X \rightarrow W^* \rightarrow y + Y \tag{2.30}$$

assuming that the energy of the excited state W^* of the compound nucleus W is E_r. To found this state an energy E_R=E_r-Q is necessary in the entrance channel; where Q is the Q-value of the reaction x+X→y+Y.

In particular, the process can occur for all excited states E_i above the Q-value. If the excited state E_r decays by the emission of γ-rays to a state E_f at lower energy, the cross section can be described by using the partial width Γ_i

$$\sigma_\gamma \propto \Gamma_{xX}\Gamma_\gamma \tag{2.31}$$

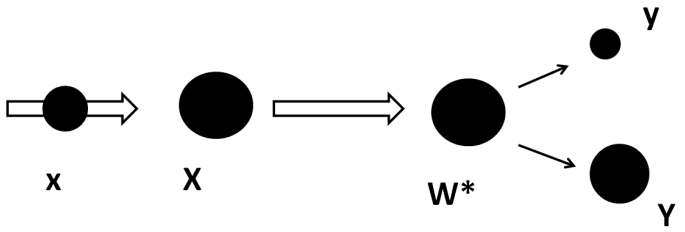

Figure 2.4: Formation and decay of an intermediate compound nucleus state [Rolfs & Rodney (1988)].

where Γ_{xX} is the partial width for the formation of the compound state and Γ_γ the one for the radiative capture neutrons. The magnitude of the resulting cross section can very widely depending on the force laws and the properties of the nuclear states involved in each step of the reaction.

2.4.1 The Breit-Wigner formula

In the case of nuclear resonant reaction the cross section is given by the Breit-Wigner formula:

$$\sigma(E) = \pi\lambda^2 \frac{2J+1}{(2J_x+1)(2J_X+1)}(1+\delta_{12})\frac{\Gamma_1\Gamma_2}{(E-E_R)^2+(\Gamma/2)^2} \tag{2.32}$$

In this formula λ indicates the De Broglie wavelength associated with the motion of the incident nucleus, and second term is a statistical term that takes into account the angular momenta of the interacting nuclei, (J_x and J_X are the spin the projectile and target nuclei respectively while J is the total angular momentum):

$$J = l + J_i + J_f. \tag{2.33}$$

All energies and widths are in the center of mass system. Moreover, Γ_1 and Γ_2 , as we said before, are the partial widths for the formation of compound nucleus and its subsequent decay, while Γ represent the total widths given by the sum of the partial widths of all open decay channels $\Gamma = \Gamma_1 + \Gamma_2 + ...$ Equation 2.31 is valid only for isolated resonances, that is resonance for which the separation of the nuclear levels is large compared with their total widths.

It is also possible to define the "narrow resonance" if the width Γ of the resonance is much smaller than the resonance energy E_R: $\Gamma \ll E_R$. The reaction rate for a narrow resonance reaction is given by:

$$< \sigma v >= \left(\frac{8}{\pi\mu}\right)^{1/2} \frac{1}{(k_b T)^{3/2}} \int_0^\infty \sigma_{BW}(E) E \exp\left(-\frac{E}{k_b T}\right) dE \tag{2.34}$$

where the quantity σ_{BW}(E) is the Breit-Wigner cross section.
For a narrow resonance (Fig. 2.5) the Maxwell-Boltzmann function Eexp(-E/kT), changes very little over the resonance region, and its value at $E=E_R$ can be taken by the integral:

$$< \sigma v >= \left(\frac{8}{\pi\mu}\right)^{1/2} \frac{1}{(k_b T)^{3/2}} E_R \exp\left(-\frac{E_R}{kT}\right) \int_0^\infty \sigma_{BW}(E) dE. \tag{2.35}$$

From the product of the statistical factor ω, where

$$\omega = \pi\lambda^2 \frac{2J+1}{(2J_x+1)(2J_X+1)}(1+\delta_{12}) \tag{2.36}$$

and the width ratio $\gamma=\Gamma_1\Gamma_2/\Gamma$, it is possible to define the strength of a resonance:

$$\omega\gamma = \omega\frac{\Gamma_1\Gamma_2}{\Gamma} \tag{2.37}$$

that is proportional to the area under the narrow-resonance cross section curve. The resonance energy enters exponentially in the above reaction rate expression. It needs to be determined rather precisely, otherwise the resulting uncertainty of the reaction rate becomes relatively large.

2.4.2 Reactions through Broad and subtreshold reactions

We consider hereafter resonances that are broader than the relevant energy window for a given temperature; a resonance is considered broad if:

$$\Gamma/E_R \geq 10 \tag{2.38}$$

The cross section σ(E) extends over a large range of energies, and the dependence of the cross section on energy needs to be taken into account for the calculation

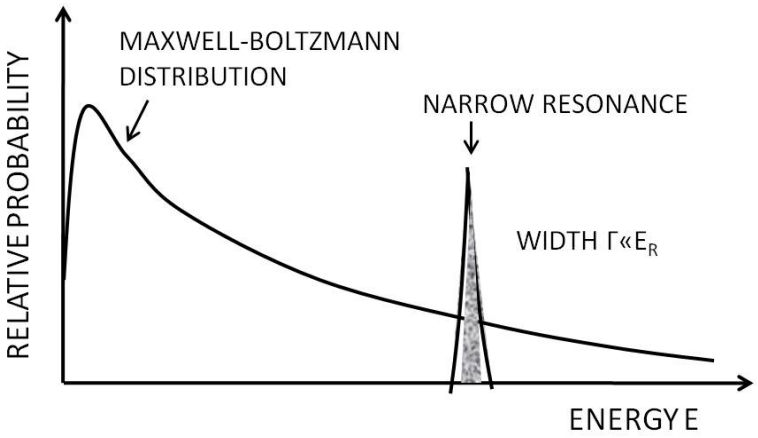

Figure 2.5: Schematic view of the Maxwell-Boltzmann energy distribution at given stellar temperature T together with a cross section for a narrow resonance [Rolfs & Rodney (1988)].

of the stellar reaction rate, the energy dependence of the cross section can be calculated as:

$$\sigma(E) = \sigma_R \frac{E_R}{E} \frac{\Gamma_1(E)}{\Gamma_1(E_R)} \frac{\Gamma_2(E)}{\Gamma_2(E_R)} \frac{(\Gamma_R/2)^2}{(E-E_R)^2 + [\Gamma(E)/2]^2} \tag{2.39}$$

where the cross section and the total width are known at the resonance energy: σ_R=σ(E$_R$), Γ_R=Γ(E$_R$). Obviously, knowledge of the energy dependence of the partial widths is necessary for the calculation of the reaction rate. If the resonance energy E$_R$ is near or above the Coulomb barrier, the partial widths for the entrance and exit channels, Γ_1 and Γ_2, slowly vary over the resonance region (E=E$_R$$\pm$$\Gamma_R$/2). In general, since the term Γ_1(E)/Γ_1(E$_R$) in this last equation varies very rapidly and nonlinearly over the resonance region, the cross section varies much more rapidly for energies below E$_R$ than for energies above E$_R$. If the cross section is expressed in terms of the S(E)-factor the asymmetric resonance shape in σ(E) is removed to a large extent.

$$S(E) = \sigma(E) E \exp(2\pi\eta) \tag{2.40}$$

Now, if we consider an excited state in a nucleus where the energy E$_r$ is smaller than the Q-value for decay to some reaction channel, such as excited state, cannot found this channel or it cannot be formed through it since the resonance

energy E_R=E_r -Q is negative. Such state is referred to as subthreshold state and the resonance formation via this reaction channel as a subthreshold resonance. Because of the width Γ that characterizes the level E_r, it is possible to populate such a subthreshold state through its high-energy tail, extending up to energies of astrophysical range, thus giving a contribution to the cross section. For this resonance reaction the cross section is described by the Breit-Wigner expression:

$$\sigma(E) = \pi\lambda^2\omega\frac{\Gamma_1(E)\Gamma_2(E+Q)}{(E-E_R)^2+[\Gamma(E)/2]^2} \tag{2.41}$$

and the S(E)-factor:

$$S(E) = E\exp(2\pi\eta)\pi\lambda^2\omega\frac{\Gamma_1(E)\Gamma_2(E+Q)}{(E-E_R)^2+[\Gamma(E)/2]^2} \tag{2.42}$$

The S(E)-factor drops rapidly with increasing energy, reflecting the high-energy wing of the subthreshold resonance. For example, proton induced non-resonant capture reactions usually have S(0)$\leq$100 keV b, thus in this case the subthreshold resonance can completely dominate the total stellar reaction rate at low temperatures. In general, for charged particle induced reactions, the cross section drops exponentially with decreasing of the center of mass energy owing to the effect of the Coulomb barrier so the measurement of the cross section becomes increasingly difficult. The observed energy dependence of σ(E) or S(E) therefore must be extrapolated into the stellar energy region (Fig 2.6).

2.5 Electron screening effect

In the extrapolation of cross sections it is assumed that the Coulomb potential of the target nucleus as seen by the projectile is that resulting from a bare nucleus; however, for nuclear reactions studied in the laboratory, interacting nuclei are usually in the form of neutral atoms or molecules or ions, respectively. The electron cloud surrounding the interacting nuclei generates a screening potential; the projectile feels no repulsive Coulomb force and it effectively penetrates a reduced Coulomb barrier vanishing outside the atomic radius R_a (Fig. 2.7) [Assenbaum (1987)]. At distances r <R_a, the electrostatic potential is constant and its approximate value is ϕ_a=Z_1e/R_a.

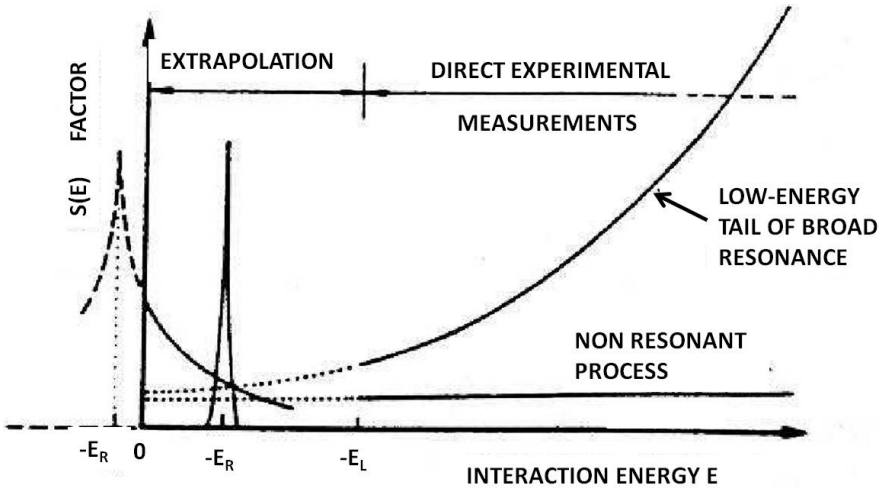

Figure 2.6: For charged-particle-induced reactions the cross section drops exponentially owing to the Coulomb barrier, so the data are usually presented in terms of S(E)-factor. If a subthreshold resonances occurs it can completely dominant the reaction rate thus the extrapolated S(E) factor is only a lower limit [Rolfs & Rodney (1988)].

The incoming projectile is subject to a Coulomb barrier with an effective height E_{eff} given by:

$$E_{eff} = \frac{Z_1 Z_2 e^2}{R_n} - \frac{Z_1 Z_2 e^2}{R_a} \tag{2.43}$$

The effect of the electron shielding on the height of the Coulomb barrier in general is negligible and it is of the order of in the ratio of nuclear to atomic radii $R_n/R_a \simeq 10^{-5}$. Only when the classical turning point R_c of an incoming projectile is close to the atomic radius R_a the magnitude of the shielding effect becomes significant. This condition correspond to $R_c \geq R_a$ and because the classical turning point is related to the projectile energy ($E = Z_1 Z_2 e^2/R_c$) it is possible to rewrite this condition in terms of the electron screening potential U_e:

$$E \leq U_e = \frac{Z_1 Z_2 e^2}{R_a}. \tag{2.44}$$

The fact that the electron screening reduces the height of Coulomb barrier implies an increased of the probability of interaction between nuclei and of the

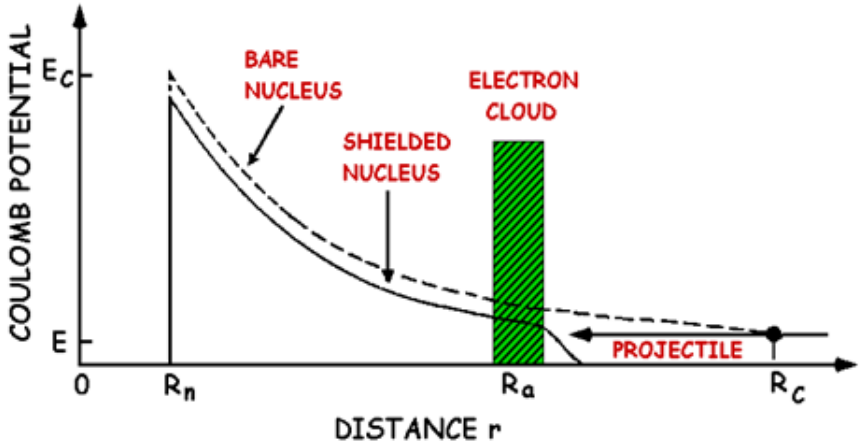

Figure 2.7: Effect of the atomic electron cloud. The Coulomb potential of a bare nucleus is reduced at all distances and vanishes for distances greater than the atomic radius R_a. The effect of electronic screening is to enhance the penetrability through the Coulomb barrier and then the cross section [Rolfs & Rodney (1988)].

cross section. The enhancement in cross section is defined as the ratio of the screened cross section σ_s(E) over the bare-nucleus one σ_b(E) and it is given by an amplification factor

$$f_{lab} = \sigma_s(E)/\sigma_b(E). \tag{2.45}$$

For example, for the p-p reaction is found that the U_e=0.029 keV. The enhancement factor can be written in an approximate form when the contribute of the electron screening potential is explicit:

$$f_{lab} = \frac{\sigma_s(E)}{\sigma_b(E)} = \frac{S_s(E)}{S_b(E)} = \frac{E}{E+U_e}\exp(\pi\eta U_e/E) \tag{2.46}$$

where η is the Sommerfeld parameter. Clearly, the enhancement factor depends only on the single parameter U_e, which in principle can be evaluated by means of atomic physics models. For $E/U_e \geq 100$ electronic shielding effects are negligible, so above these energy the bare nucleus cross-section may be measured directly in the laboratory. If $E/U_e \leq 100$, screening effects cannot be disregarded in direct measurements and one essentially measures a shielded cross section that is exponentially enhanced with respect to the bare nucleus one, as shown in figure 2.8 and 2.9

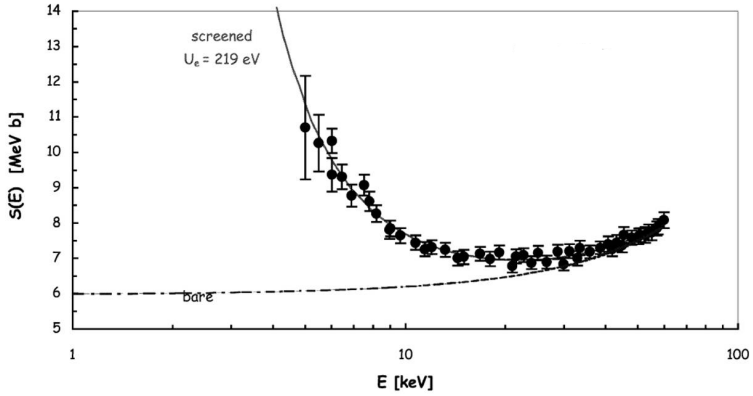

Figure 2.8: Astrophysical S(E)-factor for the ^{3}He(d,p)α reaction. The dashed curve represents the S(E)-factor for bare nuclei and the solid curve that for screened nuclei with U_e=219 eV [Aliotta *et al.* (2001)].

The value of U_e can be estimated using different theoretical approach and deduced from direct and indirect measurements, as will be explained in the next chapter. The simple model describe above does take into account that, during the collision, changes in the electronic charge distribution may occur. In fact, for the determination of the screening effects this dynamical effect must to be included. For simplicity we distinguish two opposite cases: the low velocity case, the so called *adiabatic approximation*, and the high velocity case the *sudden approximation*. In the first case, since the motion of nuclei is much slower than the electron one, the screening potential $U_e{}^{ad}$ is given by: $U_e{}^{ad}$=$E^{(1)}$+$E^{(2)}$-$E^{(comp)}$, where $E^{(1)}$+ $E^{(2)}$ is the electron binding energy in the entrance channel and $E^{(comp)}$ is the binding energy in the compound intermediate nucleus.

The adiabatic limit represents the upper theoretical limit for the electron screening potential U_e [Bracci *et al.* (1990)]. If we consider the collision between two atoms x and X, each of them in the ground state, if the nuclear motion is slower than electron one, the electronic wave function varies in an adiabatic way during the process. Therefore also the atomic compound system (x+X) will be in the ground state. The compound system has a total binding electron energy larger than the sum of the electron binding energies of the separated atoms. This gain in energy, U_e^{ad}, is transferred to the relative nuclear motion , enhancing the

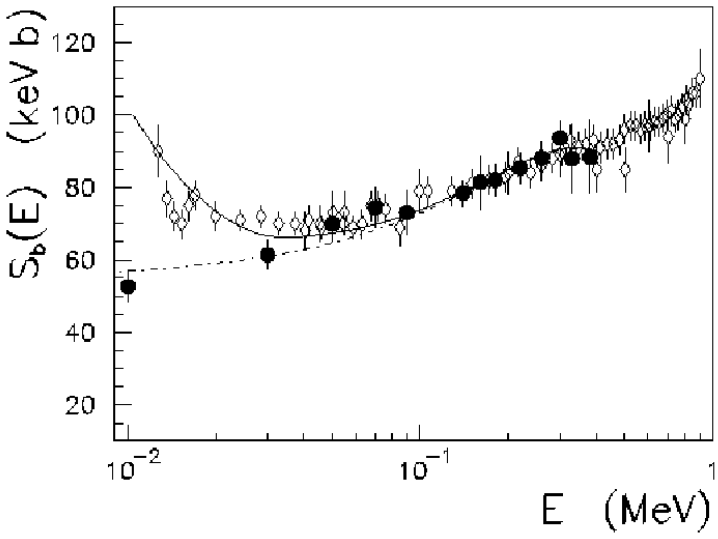

Figure 2.9: Astrophysical S(E)-factor for the reaction ^{7}Li(p,α)α. It increase with decreasing energy because of the electronic screening [Lattuada *et al.* (2001)].

reaction probability. The adiabatic limit is effective in the astrophysical energy range where low *x*-*X* relative energies are involved.

In the *sudden approximation* the velocity of nuclei is much larger than the electron one, thus electron distribution at fusion time is almost the same as it was in the initial state. In this case, the electron wave function remains unchanged during the fusion process. For example, if a bare nucleus Z_1 collides at high velocity V with an atom Z_2, in the hypothesis that the electron wavefunctions do not change during the collision, the variation of electron energy is equal to the difference of the energy potential when at Z_2 is substituted the compound nucleus Z_1+Z_2. This is the gain energy kinetic of the incident nucleus. The experimental determination of U_e has been performed for different reactions, for which it has been possible to explore the energy range where electron screening is effective. It has been found that in most of the cases the theoretical estimates of the screening potentials (using the adiabatic approximation) are systematically and sometimes dramatically lower than the experimental values (U_{ad}<U_{exp}).
This discrepancy can be attributed to different sources:

1. extrapolation of the bare nucleus cross section. The behavior of the bare

nucleus cross section is not properly modelled because of a wrong extrapolation from high energy data or measured subthreshold resonances, besides value of the electron screening can be deduced. In recent years, several indirect methods become available, which allow to determine the bare cross section with no need of extrapolation;

2. low energy stopping power. In the analysis of low energy cross section data, the evaluation of the effective energy in the target always involves energy-loss corrections, which are usually extracted from standard compilations that can provide inaccurate value right at astrophysical energies [Raiola *et al.* (2001)];

3. theoretical models. Dynamic effect such as electron cloud polarization and electron ejection could not be approximately taken into account.

2.5.1 Electron screening effect in a stellar plasma

Because of the high temperatures, in astrophysical environments the atoms can be partly or fully stripped of their electrons. Much are then immersed in a sea of electrons which tend to arrange themselves to form an electron cloud around a positive ion, resulting in an effect similar to that present in an atoms. If the thermal energy kT is much larger than Coulomb energy between the particles, the stellar gas is said "nearly perfect" and in these conditions the electrons are arranged around the nucleus in a cloud with the radius of Debye-Hückel R_{DH}:

$$R_{DH} = \left(\frac{kT}{R4\pi e^2 \rho N_A \xi} \right)^{1/2} \tag{2.47}$$

where N_A is Avogadro number and the quantity ξ is given by the equation:

$$\xi = \Sigma_i (Z_i^2 + Z_i) \frac{X_i}{A_i} \tag{2.48}$$

Z_i, A_i and X_i being the atomic number, the mass and the mass fraction of nuclei of type i respectively, and where the sum is extended over all positive ions and X_i is the mass fraction of nuclei of type i. When the gas density increases the radius R_{DH} decreases and so it does the shielding effect produced by electronic

cloud, which reduces the Coulomb potential and promotes the penetration of the Coulomb barrier causing an increase in the cross section by a factor:

$$f_{pl} = \frac{\sigma_{pl}(E)}{\sigma_b(E)} \propto \exp(\pi\eta U_{pl}/E) \tag{2.49}$$

where U_{pl} is the screening potential in the stellar interior, which is different from the potential U_e measured in the laboratory. So the cross section increases and thus the thermonuclear reaction rates:

$$< \sigma v >_{shieldednuclei} = f_{pl} < \sigma v >_{barenuclei} . \tag{2.50}$$

where f_{pl} usually differs from laboratory screening enhancement and ranges between 1 and 2 for typical density and composition [Rolfs & Rodney (1988)]. In astrophysical environments is necessary to know the cross section or, equivalently, the astrophysical factor for bare nuclei. In fact, using the astrophysical factor for shielded nucleus S_S, it is possible to obtain the astrophysical factor S_b as reported in 2.45. Knowing U_{pl} by Debye theory, is possible to get also f_{pl}, which represents the correction to the cross section in astrophysical environments.

For a stellar plasma, the value of the cross section σ_b(E) must be known because the screening in the plasma is quite different from that measured in the laboratory. Thus it is necessary to know the electron screening factor in the laboratory to extract the bare nucleus S(E)-factor from the shielded one. Moreover, understanding electron screening in the laboratory will give hints on stellar electron screening and its theoretical description. This means that, every measurements of reaction cross sections of astrophysical interest has to determine the S_b value, as mentioned above, in the energy region of the Gamow peak. Since this is almost always impossible extrapolation from the experimental data obtained at much higher energy is necessary. One of the most important uncertainties in the experimental nuclear astrophysics derive from this procedure, and because of this more exhaustive and precise information of S_b are needed at low energies.

2.5.2 Electron screening effect recent results

In recent years, the electron screening has been observed in metals. An investigation of the electron screening for the d(d,p)t reaction has been carried out in

deuterated metals, semiconductors and insulators [Raiola *et al.* (2004)]. In all metals, a large screening potential was observed of the order U_e=300 eV while a smaller screening potential was found in insulators and semiconductors. An explanation of the surprisingly large screening in metals is suggested by the Debye plasma model applied to the quasi-free electrons in metals. The Debye radius for deuterons in the lattice is given by:

$$R_{DH} = \sqrt{\frac{\epsilon kT}{e^2 n_{eff}\rho_a}} = 69\sqrt{\frac{T}{n_{eff}\rho_a}}[m] \tag{2.51}$$

where the temperature T of the quasi free electrons is in Kelvin, n_{eff} is the number of conduction electrons per metallic atom, and ρ_a is the atomic density in unit of atoms/m^3. The Coulomb energy of the Debye electron cloud and a deuteron projectile at R_D is

$$U_D = 2.09 \times 10^{-11}\sqrt{\frac{n_{eff}\rho_a}{T}}. \tag{2.52}$$

For T=293K, ρ_a= 6× 10 ^{28} m^{-3} and n_{eff}=1 it corresponds to a R_D that is a factor of 10 small than the Bohr radius of the hydrogen atom. As a consequence U_D=300eV , which is of the same order of magnitude of the observed U_e value [Raiola *et al.* (2004)]. The acceleration of the incident ions leading to the high observed U_e values is thus due to the Debye electron cloud at the rather small radius (2.51). The deduced n_{eff} values were also compared with those derived from the Hall coefficient, leading a fair agreement within experimental uncertainties for all metals with known Hall coefficient. Another critical test on the Debye model was the predicted temperature dependence, $U_D \propto T^{-1/2}$, which was verified for T 260 to 670 K. Thus, using a metallic plasma the Debye model was tested successfully with respect to all parameters entering the model. One may call metals "*a plasma of the poor man*" .

The prediction was experimentally verified in ^{7}Li(p,α)α and ^{6}Li(p,α)^{3}He (Z_t=3), ^{9}Be(p,α)^{6}Li and ^{9}Be(p,d)^{8}Be (Z_t=4) for both pure metals and alloys. The data demonstrate that the enhanced electron screening occurs across the periodic table and is not restricted to reaction among light nuclides. More complex theories have been developed one may consider the Debye model as a parametrization of the data, with an excellent predictive power. Moreover it allows for the first time a temperature dependence of nuclear cross section [Raiola *et al.* (2004)].

2.6 Extrapolation of cross sections to the Gamow window

The cross section of nuclear reactions of astrophysical interest, due to Coulomb barrier penetration, rapidly drops to values very low of order of nanobarn-picobarn at such constant energy. Due to these low values the reaction rate is very small at the relevant energies and the signal to noise ratio is very poor. Thus, the information obtained by long measurements is not accurate enough for astrophysics. In any nuclear reaction, the number of particles detected per unit of time N_{det} is proportional to the cross section σ, to the number of impinging particle per unit time N_{imp}, to the target thickness, that is to the number of target nuclei N_{tar}, to the solid angle $\Delta\Omega$ covered by the detector and to the detection efficiency in the measurement, ϵ:

$$N_{det} \propto \sigma(E) N_{imp} N_{tar} \Delta\Omega \, \epsilon \tag{2.53}$$

where σ is the cross section for the reaction of interest. As the count rate decreases, it get comparable to the contribution of background sources. Background can have different origins: it can come from physical processes competing with the one of interest, it can result from electronic noise generated from the apparatus used for acquisition and can be related to the cosmic rays. Whatever the origin of the background, the signal-to-noise ratio can be increased in two ways: 1) by optimizing the experimental apparatus to increase the number of detected particles; 2) by introducing passive or/and active shielding to reduce the background.
Obviously, the two approaches are not alternatives, but the signal cannot be increased beyond some physical limit (Ω=4π for instance).
To raise to signal to noise ratio, four independent parameters can be varied; following equation 2.53:

- Increasing the number of impinging particles N_{imp}. This calls for new accelerator and beam transport technologies to achieve μA-nA beams.

- Increasing $\Delta\Omega$ by constructing detection equipment that can cover most of the solid angle 4π. On the other hand, this implies the use a larger number of detectors, complicating the setup;

- Increasing the target thickness. This has a limit related to various causes; for example, the thickness has to be less than the range that a particle from the reactions is able to penetrate; cannot be increased beyond some value corresponding to acceptable energy resolution.

- Raising geometric efficiency by resorting to 4π detectors covering nearly the whole solid angle, or by placing the detector close to the target, but in this case the kinematic spread is responsible of a loss of energy resolution comparable to the straggling effects. Finally intrinsic detector efficiency can be a problem for reaction having γ-rays or neutrons, since intrinsic detection efficiency for charged particle detector is usually very close to one.

An increase of the signal-to-noise ratio can be also obtained by reducing the background contribution. In particular this is the only way where the physical limit has been reached. To eliminate background due to cosmic rays measurements are performed in environments shielded from them such as in underground laboratories (eg. National Laboratory Gran Sasso). The problem natural radioactivity is always present in any material, thus material presenting a low spontaneous activity are employed.

Whenever the cross section gets very small the signal approaches zero so it does the signal-to-noise ratio. The listed methods thus do not provide any improvement and indirect technologies have to be used. Even in cases where it was possible to make measurements at energies close to E_0 (Gamow peak), the astrophysical factor cannot be extracted because of the presence of the effects electron screening.

2.7 Indirect Methods

For better understanding the stellar evolution, the cross section of the astrophysically relevant nuclear reactions should be known at the Gamow energy with a good precision. The presence of the Coulomb barrier for colliding charged nuclei makes nuclear reaction cross sections at astrophysical energies very small so direct measurements in laboratories become very difficult. That is why often direct measurements are performed at higher energies and then extrapolated down to Gamow energy through extrapolation can cause an additional uncertainty. Moreover, direct laboratory experiments are affected by electron screening, so a correction has to be applied to obtain the cross section for bare nuclei.

In recent years, several indirect methods have been developed to extract cross sections relevant for astrophysics. In these alternative approaches, the astrophysical relevant two-body reaction is generally replaced by a suitable three-body one. The relation between their cross section is established with the help of nuclear reaction theory. Through this process introduces some uncertainties, valuable information on the astrophysical reaction can be obtained. Some indirect methods used today in nuclear astrophysics are: i) the Coulomb dissociation (CD) ii) the Asymptotic Normalization Coefficient (ANC), iii) the Trojan Horse Method (THM). In this section we will briefly describe the CD and ANC while in the next chapter we focus our attention on the THM.

2.7.1 Coulomb Dissocation

The CD, proposed by Baur, Bertulani and Rebel in 1986, uses the copious amount of virtual photons acting on a charged nuclear projectile when it traverses the Coulomb field of heavy nucleus [Baur & Rebel (1994)]. The time-varying electromagnetic field experienced by the projectile acts like a spectrum of equivalent photons which can dissociate the projectile. The equivalent photon spectrum can be computed from the kinematics of the process. In this way it is possible to determine the photodissociaton cross section, essentially based on quantum electrodynamics. The projectile can be an exotic nucleus. Thus one has the unique possibility to study the interaction of unstable nuclei with photons. In

this method, instead of studying directly the radiative capture process:

$$a + b \rightarrow c + \gamma \tag{2.54}$$

it is considered the time reserved process

$$\gamma + c \rightarrow b + a. \tag{2.55}$$

The reaction that occurs during the interaction of the incident nucleus with the target is a three-body process like

$$c + C \rightarrow a + b + C \tag{2.56}$$

and it is obvious that the indirect method of CD needs theoretical input in the conversion process. From the indirect experiment it is possible to extract the photo dissociation cross section

$$\sigma_{E\lambda}^{photo}(c + \gamma \rightarrow a + b) \tag{2.57}$$

and to convert it to a radiative capture cross section employing the theorem of detailed balance.

$$\sigma(a + b \rightarrow c + \gamma) = \frac{(2j_c + 1)2}{(2j_a + 1)(2j_b + 1)} \frac{k_\gamma^2}{k^2} \sigma(c + \gamma \rightarrow a + b) \tag{2.58}$$

In this equation the wave number k in the (a+b) channel is:

$$k = \sqrt{\frac{2\mu_{ab} E_{c.m.}}{\hbar^2}} \tag{2.59}$$

where μ is the reduced mass, while the photon wave number is given in terms of the Q-value of the capture reaction:

$$k_\gamma = \frac{E_\gamma}{\hbar c} = \frac{E_{c.m.} + Q}{\hbar c}. \tag{2.60}$$

Usually $k_\gamma \ll k$ so that the phase space favors the photodisintegration cross section as compared to the radiative capture. Fig 2.10 shows schematically the Coulomb dissociation process.

From the experimental point of view there are several advantages; i) the energy of the projectile is sufficiently high (10-100 MeV), the two fragment a and b

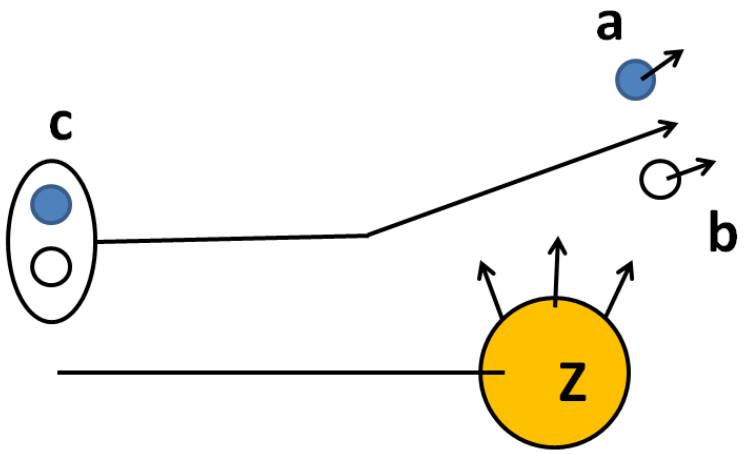

Figure 2.10: Coulomb Dissociation a→ b+c in the field of a target nucleus Z [Baur *et al.* (1986)].

emerge with a rather high energy that facilitates their detection; ii) the choice of adequate kinematical conditions allows to study rather low relative energy of the a and b system thus ensuring that the target nucleus stays in the ground state; iii) the large number of virtual photons seen by the passing projectile leads to an enhancement of the cross section. Assuming that the nuclear effects are not important or that it possible to remove this contribution from the experimental data, that the break up is not resonant and that no post accelerating effects are present. It is possible to factorized the cross section for the three-body process as follows:

$$\frac{d^2\sigma}{d\Omega dE_\gamma} = \frac{1}{E_\gamma}\frac{dn_{E\lambda}}{d\Omega}\sigma_{E\lambda}^{photo}, \tag{2.61}$$

where $1/E_\gamma$ is a kinematical factor, $dn_{E\lambda}/d\Omega$ is the virtual-photon number for unit solid angle and $\sigma_{E\lambda}{}^{photo}$ is the cross section for the photodisintegration process. This equation shows the factorization of the break-up cross section into two terms (a part from the kinematical factor) one corresponding to the virtual photon sources and the other to the photodisintegration pole. Difficulties arise from the presence of effects going beyond the one-photon exchange. Moreover, nuclear interaction is present, leading to nuclear deflection and diffraction of small

impact parameter, if such contributions are not suppressed by the strong absorption. The break-up process can be described by means of two limiting models: resonant break-up if a long living resonance of the projectile is excited, later decaying to the a+b channel; direct (non resonant) break up, where the excitation and the decay region are not separated. In the first case, the excited projectile escapes from the field before disintegrating, in the second case, final state effects may occur, such as post-acceleration of the fragments. A general solution is still open on problem and needs specific consideration of the uncertainties involved for each particular case [Baur & Rebel (1994)].

2.7.2 ANC method

The ANC technique is based on the fact that direct proton-capture reactions of astrophysical interest often involve systems where the binding energy of the captured particle is low. Hence, at stellar energy the capture proceeds through the tail of the nuclear overlap function. The shape of the tail of the overlap function is completely determined by the Coulomb interaction and its amplitude fixes the rate of the capture reaction. This method can be used then to determine the astrophysical factors for peripheral radiative capture processes of the type A+ a $\rightarrow$ B+γ. This is the case of several reactions of astrophysical interest where the interacting particles stays well inside the nuclear well. Moreover the ANC technique turns out to be very productive for analysis of the astrophysical processes in the presence of the subthreshold resonance, and this technique can be used to determine the interference sign of the direct and resonant amplitudes for some important astrophysical radiative capture reactions [Mukhamedzanov & Tribble (1999), Xu *et al.* (1994)]. In general direct capture reaction A(p,γ)B cross section can be written as:

$$\sigma = \lambda \| < I^B_{Ap}(r) \| O(r) \| \Psi^+_i(r) > \|^2 \tag{2.62}$$

where λ is a kinematical factor, O is the electromagnetic transition operator, Ψ^+_i is the scattering wave in the incident channel and I^B_{Ap} is the overlap function for B$\rightarrow$ A+p system. The determination of an appropriate expression for this

overlap function by means of a suitable transfer reaction is the aim of the ANC. The overlap function can be written:

$$I^B_{Ap} \approx C\frac{W_{-\eta,l+1/2}(2\kappa r)}{r} \tag{2.63}$$

where the ANC C defines the tail of the radial overlap function, W is Whittaker function, η and l are the Coulomb parameter and the angular momentum for the bound states B=A+p and κ is the bound state wave number. Is evident that the cross section 2.61 is directly proportional to the square of the ANC. ANCs are measured by means of peripheral transfer reactions. If consider a proton transfer reaction A(a,c)B where a=c+p and B=A+p the cross section can be parametrized in terms as follows:

$$\frac{d\sigma}{d\Omega} = \Sigma_{jBja}\frac{(C^B_{Apl_{BjB}})^2}{b^2_{Apl_{BjB}}}\frac{(C^a_{cpl_{aja}})^2}{b^2_{cpl_{aja}}}\sigma^{DW}_{l_{BjB}l_{aja}} \tag{2.64}$$

where $\sigma^{DW}_{l_{BjB}l_{aja}}$ is the reduced Distorted Way Born Approximation cross section [Mukhamedzanov *et al.* (2005)], and j_i, l_i are the total and orbital angular momenta of the transferred proton in nucleus i. The factor $b_{cApl_{aja}}$ and $b_{Apl_{BjB}}$ are the ANCs for bound state proton wave functions in nuclei a and B which are related to the corresponding ANC of the overlap function by:

$$(C^a_{cplaja})^2 = S^a_{cpl_{aja}}b^2_{cpl_{aja}} \tag{2.65}$$

in this equation $\mathrm{S}_{cpl_{aja}}{}^a$ is the spectroscopic factor. If the reaction is peripheral the ratio:

$$R_{lBjBlaja} = \frac{\sigma^{DW}_{l_{BjB}l_{aja}}}{b^2_{Apl_{BjB}}b^2_{cpl_{aja}}} \tag{2.66}$$

is independent of the single particle ANCs. $\frac{d\sigma}{d\Omega}$ is then proportional to the product of the two ANCs and this factor can be deduced by normalization of the theoretical cross section to experimental one [Mukhamedzanov & Tribble (1999)]. When $(\mathrm{C}^B{}_{Apl_{BjB}})^2$ is known it can be used to fix the tail value of the overlap function

$I^{B}{}_{Ap}$ and then is possible to extract the cross section for peripheral radiative capture reaction of interest for astrophysics. In order to extract reliable ANCs from a transfer reaction, this must be peripheral. This can be checked with a DWBA code by changing the radius and diffuseness parameter for the binding of the transferred particle to the core and determining the ratio $R_{l_{BjB}l_{aja}}$; in a peripheral transfer, the ratio will be nearly constant over a broad range of the parameters. The predicted DWBA cross section will change by large factors.

To test the ANC technique the S-factor was determined for the ground and first excited state of the ^{16}O(p,γ)^{17}F, which is a pouring direct capture reaction at low energy. For this reactions the required *C's* were obtained from the transfer reaction ^{16}O(^{3}He,d)^{17}F. Similarly, using the ANC determined from the proton exchange reaction ^{9}Be(^{10}B,^{9}Be)^{10}B, the component of the atrophysical factor at low energy for the ^{9}Be(p,γ)^{10}B reaction was obtained [Sattarov *et al.* (1999)]. The obtained result is in good agreement with the two previous measurement of the ^{16}O(p,γ)^{17}F reaction [Gagliardi *et al.* (1998)]. As examples of recent measurements with stable beams, the ANCs for ^{15}O$\rightarrow$ ^{14}N+p and ^{21}Na$\rightarrow$ ^{20}Ne +p system have been determined using the ^{14}N(^{3}He,d)^{15}O and ^{20}Ne(^{3}He,d)^{21}Na reactions [Mukhamedzanov & Tribble (1999)]. In detail the ANCs were obtained for the ground and five excited states of ^{15}O and the ground and three excited states of ^{21}Na. In both reactions, at stellar energies capture is dominated by a subthreshold state. In this case, ANCs have been used to obtain the astrophysical S factors for both system [Mukhamedzanov *et al.* (2006)]. In addition to the proton transfer reactions mentioned above, neutron ANCs have been measured for several system. For example, the ANCs for ^{8}Li $\rightarrow^{7}$Li $+n$ have been obtained from the neutron transfer reaction ^{13}C(^{7}Li,^{8}Li)^{12}C. Many measurements of ANCs have been carried out also with radioactive beams.

For example is possible to remember the ^{14}N(p,γ) ^{15}O reaction, one of the most important reaction of the *CNO cycle*, the rate of this reaction has a major impact on the evolution of a wide range of star. From the measurement the total astrophysical factor for this reaction was deduce [Schroeder *et al.* (1987)]. At very low energies appropriate for stellar burning, the reaction was found to be dominated by a combination of direct and resonant capture and interference from the tail of the subthreshold resonance and the first resonance.

Chapter 3

Trojan Horse Method

The THM is an experimental indirect technique that is suited to deduce a charged particle binary-reaction cross section inside the Gamow window, by selecting the *quasi-free* (QF) contribution of a suitable three-body reaction. When studying charged-particle-induced reactions at sub-Coulomb energies, the Coulomb barrier causes a strong suppression of the cross section, which drops exponentially with decreasing energy. In addition, the electron screening effect, due to the electrons surrounding the interacting ions, prevents one to measure the bare nucleus cross section. Today, the only way to get the ultra-low-energy bare-nucleus cross section is by extrapolating the behavior of the higher energy data. This is done by means of the definition of the astrophysical S(E) factor, defined in the previous chapter, showing a much smoother energy dependence than the cross section. An alternative technique is provide by indirect method such as the THM.

3.1 Quasi-free break-up and sequential mechanism

The QF mechanism is a direct reaction process which can be described as a participant-spectator mechanism. In particular, a nucleus a breaks up into two clusters inside the nuclear field of A, yielding a spectator particle s and a participant virtual particle x. The overall reaction is:

$$A + a \rightarrow c + C + s \tag{3.1}$$

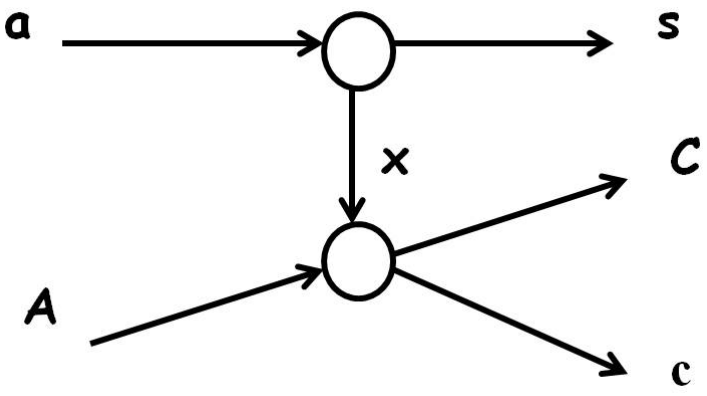

Figure 3.1: A pseudo-Feynman diagram for a QF reaction; a= x⊕s. The upper pole represent break-up of the TH nucleus and the lower pole represent the the virtual two body reaction.

where a can be described in terms of x⊕s cluster structure. The condition that the spectator particle s has to fulfill is that the momentum is the same that it had in the nucleus a. The transferred nucleus x appears only as a virtual particle in the reaction process. To represent this process a pseudo-Feynman diagram is used (Fig. 3.1). In figure 3.1 the upper vertex represents the breakup of the target nucleus a into the cluster x and s while the lower vertex represents the virtual two body interaction

$$A + x \rightarrow c + C. \tag{3.2}$$

The cross section of the three-body reaction 3.1 can be related to the two-body one with the help of direct reaction theory.

Since the THM is based on the selection of the QF coincidence yield it is necessary to discriminate this process from other possible mechanisms that may occur between the target and projectile, giving the same particles in the final state. As example is given by the sequential mechanism. This is described as a two step interaction, in the sense that the exit channel is reached through an intermediate one as shown in Figure 3.2. Although sequential process are often dominant in 3-body reactions, under particular kinematical conditions, their contribute can be distinguished and separated from the QF one. The sequential

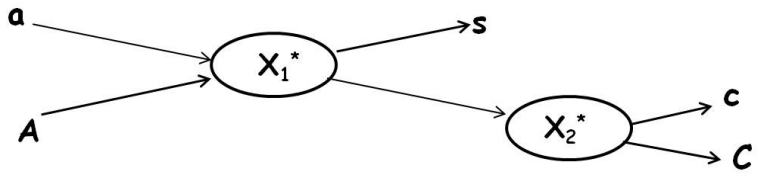

Figure 3.2: A pseudo-Feynman diagram for a three-body sequential process, which gives in the exit channel the same particle that the QF process describe before, through the formation of an intermediate nucleus X_1.

contribution represents a background process that has to be removed during the off-lines data analysis.

3.2 The method

The THM, first suggested by G.Baur [Baur *et al.* (1986)] and significantly improved afterwards [Spitaleri *et al.* (1999),Cherubini *et al.* (1996), Calvi *et al.* (1997), Spitaleri *et al.* (2001), Romano & others. (2008), La Cognata *et al.* (2006)] makes use of QF reactions (e.g. equation 3.1) to extract the cross section of a binary reaction of astrophysical interest. Thanks to the high energy (e.g. about 10 MeV/u) in the $A+a$ entrance channel, the two-body interaction can be considered as taking place inside the nuclear field, without experiencing either Coulomb suppression or the electron screening. Anyway, A-x interaction can take place at astrophysical energies as the beam energy is compensated for by the x-s binding energy, determining the so called 'QF energy' given by:

$$E_{q.f} = E_{Ax} - B_{xs} \pm E_{xs} \tag{3.3}$$

where E_{Ax} represents the beam energy in the center of mass of the A-x system, B_{xs} is the x+s binding energy and E_{xs} correspond to the energy of their inter-cluster motion within the chosen cutoff in the momentum [Tumino *et al.* (2003)]. Then, a cutoff in the momentum spectrum, which is related to the Fermi motion of s inside the Trojan-Horse nucleus a, fixes the range of energies around the QF energy accessible in the astrophysical relevant reaction.

3.2.1 Theory I: Plane Wave Impulse Approximation

It is possible to describe the THM using the Impulse Approximation (IA) [Chew & Wick (1952), Jain *et al.* (1970)], which is based on some fundamental assumptions:

- The projectile A does not interact with both the constituents of the cluster structure (x and s) at the same time. Equivalently, the average distance between the two constituent of the system is larger than the wavelength associated to the impinging projectile;
- the interaction of the incident particle with the cluster x in the target is the same as if that cluster were alone. In other words, the wave amplitude associated with the projectile A when it interacts with x is not affected by the presence of the spectator s;
- the binding energy between the constituents of the nucleus a is supposed to be negligible compared to the energy of the incident projectile.

If these assumptions are fulfilled, assuming that the incident and outgoing particles can be described in terms of plane waves and that the wave function of nucleus a can be expressed in terms of the x-s cluster configuration, the cross section for the three-body reaction (3.1) takes a very simple form [Jain *et al.* (1970)]. Indeed, it can be factorized into two terms corresponding to the two poles of Figure 3.1:

$$\frac{d^3\sigma}{dE_c d\Omega_c d\Omega_C} \propto KF \left(\frac{d\sigma}{d\Omega_{cm}}\right)^{HOES} |\Phi(\overrightarrow{p_s})|^2 \tag{3.4}$$

where: i) KF is a kinematical factor containing the final state phase-space factor and it is a function of the masses, momenta, and angles of the outgoing particles:

$$KF = \frac{\mu_{Aa} m_c}{(2\pi)^5 \hbar^7} \frac{p_C p_c^3}{p_{Aa}} \left[\left(\frac{\overrightarrow{p}_{Bx}}{\mu_{Bx}} - \frac{\overrightarrow{p}_{Cc}}{m_c} \right) \cdot \frac{\overrightarrow{p}_c}{p_c} \right]^{-1}; \tag{3.5}$$

ii) $(\frac{d\sigma}{d\Omega_{cm}})^{HOES}$ is the half-off-energy-shell (HOES) differential cross section for the two body reaction $A(x,c)C$ at the center of mass energy E_{cm} given in post-collision prescription by:

$$E_{cm} = E_{cC} - Q_{2b}, \tag{3.6}$$

where Q_{2b} is the Q-value of the binary reaction and E_{cC} is the relative energy of the outgoing particles c and C. Note that the deduced total two-body cross section $(d\sigma/d\Omega)^{HOES}$ consists of the nuclear part only. The superscript HOES is due to the virtuality of the transferred particle x, because in the entry channel it is not a free particle being bound inside a. It means that the relation between the energy and momentum for the nucleus x is not valid:

$$E_x \neq \frac{p_x^2}{2m_x} \tag{3.7}$$

The HOES cross-section $(d\sigma/d\Omega)^{HOES}$ is converted to the relevant on-energy-shell (OES) cross section $(d\sigma/d\Omega)^{OES}$ (here called THM) by introducing the Coulomb suppression in the HOES cross section in the form of the penetrability factor.

iii) $\Phi(\overrightarrow{p}_s)$ is the Fourier transform of the radial wave function $\chi(\overrightarrow{r})$ for the x-s intercluster motion, usually described in terms of Hänkel, Eckart and Hulthén functions depending on the x-s system properties:

$$\Phi(\overrightarrow{p}_s) = (2\pi)^{-\frac{3}{2}} \int_{-\infty}^{+\infty} \Psi(\overrightarrow{r}) exp(-i\overrightarrow{K}_s \cdot \overrightarrow{r}) d\overrightarrow{r} \tag{3.8}$$

If the momentum distribution is known from independent measurements or calculations and evaluating KF taking into account the experimental and kinematical conditions, it is then possible to derive $(\frac{d\sigma}{d\Omega_{cm}})^{HOES}$ from a measurement of the three-body differential cross-section $\frac{d^3\sigma}{dE_c d\Omega_c d\Omega_C}$ by using equation 3.6. Consequently, it is possible to extract the two-body cross section after inserting the appropriate penetration function G_l to account for the suppression affecting the direct data below the Coulomb barrier:

$$\frac{d\sigma}{d\Omega} = \Sigma_l G_l \left(\frac{d\sigma}{d\Omega_{cm}} \right)^{HOES} \tag{3.9}$$

where G_l is the transmission coefficient for the l-th partial wave measurements or calculation [Spitaleri *et al.* (1999)].

3.2.2 Theory II: Distorted Wave

Besides the PWIA approach, the Distorted Wave Impulse Approximation (DWIA) treatment was sometimes applied in the analysis of QF-reaction and QF scattering

experimental data. In particular, the DWIA allows one to obtain spectroscopic information related to the intercluster wave function $\chi(\overrightarrow{r})$. In the DWIA [Roos *et al.* (1976)] the radial wave functions are deduced from optical-model potentials so that $|\Phi(\overrightarrow{p}_s)|^2$, in equation 3.7, turns out to be dependent on the considered reaction as well as on the energy. It has to be stressed that the main difference between the momentum distributions calculated in PWIA and in DWIA is twofold [Jain *et al.* (1970), Roos *et al.* (1976)]:

- The tails of the *x-s* momentum distribution. For recoil momenta, $p_s < 40$ MeV/c, the essential features of $|\Phi(\overrightarrow{p}_s)|^2$ are the same in both procedures. For instance, calculations of the cross section for (p,pα) reactions at 100MeV on ^{6}Li, ^{7}Li, ^{9}Be, and ^{12}C show very similar shapes in the low momentum region, with the only exception of ^{12}C. However, while the PWIA introduces unphysical zeros in the momentum distribution, they are properly filled in a DWIA treatment [Roos *et al.* (1976), Chant & Roos (1977)].

- The absolute value of the cross section. Indeed, in the DWIA treatment the absolute value of the momentum distribution undergoes a dramatic decrease due to wave absorption effects, which are not taken into account in PWIA. The reduction factor ranges from a few units to several orders of magnitudes.

In particular, because of the various approximations involved in the THM and of the assumption that off-energy-shell effects are negligible, it is not possible to extract the absolute value of the cross section. However, it can be obtained through normalization to the direct data available at energies above the Coulomb barrier. Thanks to this, selecting the region of low spectator momentum, where PWIA and DWIA wave functions have very similar shapes [Chant & Roos (1977)], the astrophysical S(E)-factor can be deduced by the relation:

$$S(E) = E \sum_l G_l \sigma_l^N \exp(2\pi\eta) \tag{3.10}$$

[Spitaleri *et al.* (1999), Spitaleri *et al.* (2004)]. When the projectile energy is not very high and distortion effects are not negligible, a more sophisticated approach based on a modified plane wave Born approximation (MPWBA)[Typel & Wolter

(2000), Typel & Baur (2003)] turned out to be useful in a number of experimental applications of the THM [La Cognata *et al.* (2005), Lattuada *et al.* (2001), Musumarra *et al.* (2001)]. Here we give few details about such an approach. The cross section for reaction $A+a\rightarrow\ c+C+s$ with three particles in the final state depends on the choice of the independent variables and the reference system. Then the differential cross section takes the form:

$$\frac{d^3\sigma}{dE_c d\Omega_c d\Omega_C} = KF|T_{fi}|^2 \tag{3.11}$$

The T-matrix element T_{fi} contains all the essential information relevant to the scattering process. In the distorted wave born approximation (DWBA) it has the form:

$$T_{fi} = \langle \chi^{(-)}_{Bs} \Psi^{(-)}_{Cc} \phi_s | V_{xs} | \chi^{(+)}_{Aa} \phi_A \phi_a \rangle. \tag{3.12}$$

The internal wave functions of nuclei A, a and s are denoted by ϕ_A,ϕ_a and ϕ_s, respectively. The distorted waves $\chi^{(+)}_{Aa}$ and χ^{-}_{Bs} describe the relative motion in the initial and final channel, where B stands for the c+C system. $\Psi^{(-)}_{Cc}$ is the full scattering wave function for the c+C system, while V_{xs} is the interaction potential between the transferred particle x and the spectator s. A crucial step is the so-called *surface approximation* that has been discussed in Typel et al.(2000), enabling us to establish a connection between T_{fi} and the S-matrix elements of the two-body reaction. Using this approximation, only peripheral reactions are supposed to contribute significantly to the matrix element, while absorption at smaller distances between the colliding nuclei is assumed very strong [Spitaleri *et al.* (2001)]. Using the *surface approximation* and the MPWBA the three body cross section can be expressed as:

$$\frac{d^3\sigma}{dE_c d\Omega_c d\Omega_C} = KF|W(\overrightarrow{Q}_{Bs}|^2 \frac{16\pi^2}{(k_{Ax}Q_{Aa})^2} \frac{v_{Cc}}{v_{Ax}} \frac{d\sigma^{TH}}{d\Omega_{Ax}} \tag{3.13}$$

where the quantities $\overrightarrow{Q}_{Aa}$ and $\overrightarrow{Q}_{Bs}$ are:

$$\overrightarrow{Q}_{Aa} = \overrightarrow{k}_{Aa} - \frac{m_A}{m_A + m_z} \overrightarrow{k}_{Bs}, \tag{3.14}$$

$$\overrightarrow{Q}_{Bs} = \overrightarrow{k}_{Bs} - \frac{m_s}{m_s + m_z} \overrightarrow{k}_{Aa} \tag{3.15}$$

with the relative momenta $\hbar\overrightarrow{k}_{Aa}$ and $\hbar\overrightarrow{k}_{Bs}$ in the entrance and exit channels, respectively. The momentum distribution W($\overrightarrow{Q}_{Bs}$) is connected to the wave function of a in momentum space. By taking the Fourier transform of the Schrödinger equation for the a=x⊕s bound system, it can be shown that [Typel & Wolter (2000)]

$$W(\overrightarrow{Q}_{Bs}) = \left(\varepsilon_a - \frac{\hbar^2 Q_{Bs}^2}{2\mu_{xs}}\right)\Phi_a(\overrightarrow{Q}_{Bs}) \tag{3.16}$$

with the binding energy ε_a<0. The momentum $\hbar\overrightarrow{Q}_{Bs}$ is the relative momentum of the spectator and the transferred particles. If the intercluster motion is neglected, -$\overrightarrow{Q}_{Bs}$ represents the momentum transfer to the spectator nucleus s thus it describes the momentum of s inside a, in QF conditions. On the other hand, -$\overrightarrow{Q}_{Aa}$ can be regarded as the momentum transfer to A by the cluster x.

The cross section is:

$$\frac{d\sigma^{TH}}{d\Omega}(Cc \to Ax) = \frac{1}{4k_{Cc}^2}|\Sigma_l(2l+1)P_l(\hat{Q}_{Aa}\cdot\hat{k}_{Cc})[S_l J_l^{(+)} - \delta_{(Ax)(Cc)}J_l^{(-1)}]|^2 \tag{3.17}$$

with the total (nuclear + Coulomb) S-matrix elements S_l for the reaction $C+c \to A+x$, where $\delta_{(Ax)(Cc)}$ is the Kronecker symbol. It has the form of a usual two body cross section except for the function $J_l^{(\pm)}$ which are a consequence of the half-off-energy-shell nature of the two-body process. They can be well approximated by

$$J_l^{(\pm)} = D_l k_{ax} Q_{Aa} R^2 e^{\mp i\sigma l}[G_l(k_{ax}R) \pm iF_l(k_{ax}R)] \tag{3.18}$$

where D_l is a constant, F_l and G_l are the regular and irregular Coulomb functions, σ_l is the Coulomb phase shift in partial wave l and R is cut-off radius originating from the surface approximation. The argument of the Legendre polynomial P_l is the cosine of the center-of-mass scattering angle for the two-body reaction. The analysis is simplified if the reaction of astrophysical interest is a nonelastic two body process with different initial and final channels. Then, assuming that only one partial wave l contributes to the total cross section, we find:

$$\frac{d^3\sigma}{dE_c d\Omega_c d\Omega_C} = KF|W(\overrightarrow{Q}_{Bs})|^2 \frac{v_{Cc}}{v_{Ax}} P_l^{-1} C_l \frac{d\sigma_l}{d\Omega_{Ax}}(Cc \to Ax) \tag{3.19}$$

with the on-shell two-body cross section $\mathrm{d}\sigma_l/\mathrm{d}\Omega_{Ax}$ for the reaction $C+c\rightarrow A+x$ in partial wave l and a constant C_l. The essential feature is the apparance of the Coulomb penetrability factor

$$P_l(k_{Ax}R) = \frac{1}{G_l^2(k_{Ax}R) + F_l^2(k_{Ax}R)}, \tag{3.20}$$

which compensates for the strong suppression in the two-body cross section at small energies due to the Coulomb repulsion. Because of the presence of the factor C_l and the surface approximation, the two body cross section can only be obtained with an arbitrary normalization, so the energy dependence only can be extracted only. However, this is not a problem since the absolute magnitude can be derived from the scaling to the direct data available at higher energies.

3.3 Theory III: The modified R-matrix approach

When the THM is applied to reactions proceeding through a resonant state in the subsystem a different approach is required, which takes into account the off-shell character of the transferred particle x. Thus, the modified R-matrix approach has been introduced. The conventional R-matrix approach [Lane & Thomas (1958)] was developed in the analysis of binary resonant reactions. The R-matrix approach is based mainly into two assumption:

- Non-relativistic quantum mechanics is applicable. This requirement is fulfilled by low energy nuclear astrophysics since the energies involved in the examined process stay much lower than the masses of interacting nuclei
- It is possible to divide the whole space, for each pair of nuclei, in two regions. The first one is the external region where the particles interact through the Coulomb potential and therefore the wave function are exactly known, the other one is the internal region (with radius a) where nuclear potential is dominant. In such a region, approximately corresponding to the sum of the radii of the colliding nuclei, nuclear reaction can take place, both direct and compound nucleus reactions. The physics of the process is contained in the R-matrix parameter.

In the R-matrix theory, the physics of the collision process is described by a parameter set, defined in the internal region, and associated with resonances or in the R-matrix vocabulary, with poles. These parameters are the energies and width of the poles. The R-matrix method can be applied in two direction [Lane & Thomas (1958)]:

1. To solve the Schrödinger equation for positive energies. In that case the pole properties are determined from a set of basic functions.

2. To fit experimental phase shifts or cross section. The pole properties are considered as adjustable parameters and are fitted to data. This is the main application of the R-matrix method in nuclear astrophysics.

The standard R-matrix has to be modified to account for the off-shell nature of particle x when considering TH reactions. The entry-channel widths appearing in the R-matrix cross section, is replaced by the square of the transfer reaction amplitude, populating resonance states. The generalized R-matrix method has been developed for the two channel, two level case as explained in La Cognata *et al.* (2007), La Cognata *et al.* (2010). Let us consider the TH reaction $a+A \rightarrow c+C+s$ where a=x$\bigoplus$s, and used to obtain the astrophysical factor for the binary subreaction $x+A \rightarrow c+C$. If this is resonant, disregarding the particle spins the TH reaction amplitude is given in post form by:

$$M(P, \mathbf{k}_{aA}) = < \chi^{-}_{\mathbf{k}_{sB}} \varphi_s \Phi^{-}_B | \Delta V_{sB} | \Psi^{+}_i > \tag{3.21}$$

where Φ^{-}_B is the wave function of the system $B=c+C=x+A$, Ψ^{+}_i is the exact $a+A$ scattering wave function,$\chi^{-}_{\mathbf{k}_{sB}}$ (r_{ij}) is the distorted wave of the system $s+B$, φ_i is the bound state wave function of nucleus i, P=$\{\mathbf{k}_{sB}, \mathbf{k}_{cC}\}$ is the six-dimensional momentum describing the three-body system s c and C in the exit channel. $\Delta \mathrm{V}_{sB}=\mathrm{V}_{sB}-\mathrm{U}_{sB}$, $\mathrm{V}_{sB}=\mathrm{V}_{sc}+\mathrm{V}_{sC}=\mathrm{V}_{sA}+\mathrm{V}_{sx}$ is the interaction potential of s and the system B and U_{sB} is their optical potential. The surface approximation assumes that the TH reaction amplitude has contribution from the external region only, where the interaction between the fragments C and c (A and x) can be neglected and the wave function Φ^{-}_B can be replaced by its leading asymptotic form, which contains the ingoing wave in the channel $x+A$. It means that, when

considering resonant reactions, where the contribution from the internal region is dominant, the surface approximation fails and the MPWBA cannot be applied. Equation 3.21 is the exact expression for the TH reaction amplitude and can be used as a starting point to derive the expression for the TH reaction amplitude proceeding through the interfering resonances in the subsystem B. Assuming that the resonant reaction $x+A \rightarrow c+C$ proceeds through the formation of the intermediate compound state Φ_i, the direct coupling between the initial $x+A$ and final $c+C$ channels, which dominantly contributes to direct reactions but gives negligible contribution to resonant one, is neglected. An important step in deriving the resonant contribution to the TH reaction matrix element is the spectral decomposition for the wave function $\Phi^-{}_B$ [Mahaux & Weidenmüller (1969)]. It leads to a representation for Φ_B^- that is similar the level decomposition for the wave function in the internal region in the R-matrix approach:

$$\Phi_B^- \approx \sum_{\nu,\tau=1}^{N} \tilde{V}_\nu^{cC}(E_{cC})[D^{-1}]_{\nu\tau}\Phi_\tau \tag{3.22}$$

where N is the number of the levels included, E_{cC} is the relative kinetic energy of the nuclei c and C, Φ_τ is the bound state wave function describing the compound system F excited to the level τ and $[\mathrm{D}^{-1}]_{\nu\tau}$ is the same level matrix as in the conventional R-matrix theory [Mahaux & Weidenmüller (1969)], which in the simplest case (one resonance) is given by $[\mathrm{D}^{-1}]_{\nu\tau} = \frac{1}{E_R - E}$. Finally:

$$\tilde{V}_\nu^{cC}(E_{cC}) = < \chi_{cC}^- \varphi_c | \Delta V_{cC} | \Psi_\nu > \tag{3.23}$$

is the resonance form factor for the decay of the resonance ν, described by the compound state Φ_ν, into the channel $c+C$. The partial resonance width is given by:

$$\tilde{\Gamma}_\nu(E_{cC}) = 2\pi |\tilde{V}_\nu^{cC}(E_{cC})|^2. \tag{3.24}$$

Then the reaction amplitude is:

$$M^R(P, \mathbf{k}_{aA}) = \sum_{\nu\tau=1} \tilde{V}_\nu^{cC}(E_{cC})[D^{-1}]_{\nu\tau} \times M_\tau(\mathbf{k}_{sB}, \mathbf{k}_{aA}) \tag{3.25}$$

where $M_\tau(\mathbf{k}_{sB}, \mathbf{k}_{aA})$ is the exact amplitude for the direct transfer reaction $a+A \rightarrow s+B_\tau$ populating the compound state B_τ of the system $B=x+A=c+C$ and

$$M_\tau(\mathbf{k}_{sB}, \mathbf{k}_{aA}) =< \chi^-_{sB}\Phi_\tau|\Delta V_{sB}|\Psi^+_i > . \tag{3.26}$$

The direct transfer reaction is very well described by the DWBA amplitude, so the term $M_\tau(\mathbf{k}_{sB}, \mathbf{k}_{aA})$ can be replaced by:

$$M^{DW}_\tau(\mathbf{k}_{sB}, \mathbf{k}_{aA}) =< \chi^-_{sB}\Phi_\tau|\Delta V_{sB}|\varphi_a\varphi_A\chi^-_i > . \tag{3.27}$$

The DWBA takes into account the rescattering of nuclei a and A in the initial state of the TH reaction and enters as a form factor into the TH resonant reaction amplitude, reflecting the off-energy shell character of the transferred particle x. Since in the THM the astrophysical factor is normalized to the on-energy-shell (OES) S-factor, the replacement of the exact transfer amplitude by the DWBA one does not affect the final results. At this point is possible to extract the triple differential cross section for the TH process $a+A \rightarrow s+c+C$ proceedings through interfering resonances [Mukhamedzanov *et al.* (2008)]:

$$\frac{d^3\sigma}{dE_{cC}d\Omega_{\mathbf{k}_{cC}}d\Omega_{\mathbf{k}_{sB}}} = \frac{\mu_{cC}\mu_{sB}\mu_{aA}}{2\pi^5}\frac{k_{cC}k_{sB}}{k_{aA}}\frac{1}{\hat{J}_a\hat{J}_A} \times \left|\sum_{\nu,\tau=1}^{N}\tilde{V}^{cC}_\nu(E_{cC})[D^{-1}]_{\nu\tau}M_\tau(\mathbf{k}_{sB}, \mathbf{k}_{aA})\right|^2 \tag{3.28}$$

where $E_{cC} = k^2_{cC}/(2\mu_{cC})$, μ_{ij} is the reduced mass of particles i and j, $\hat{J}$=2J+1 is the statistical factor for the i_{th} particle. The simplest case for TH process is that proceeding through an isolated resonance; the triple differential cross section is then given by:

$$\frac{d^3\sigma}{dE_{cC}d\Omega_{\mathbf{k}_{cC}}d\Omega_{\mathbf{k}_{sB}}} = |KF|\frac{\Gamma_{Cc(\tau)}(E_{cC})|M^{DW}_\tau(\mathbf{k}_{sB}, \mathbf{k}_{aA})|^2}{(E_{Ax} - E_{R_\tau})^2 + i\frac{\Gamma^2_\tau(E_{Ax})}{4}} \tag{3.29}$$

where KF is the kinematical factor, $\Gamma_{Cc(\tau)}(E_{cC})$ is the observable resonance partial width in the channel $c+C$, $\Gamma_\tau(E_{Ax})$ is the total observable width of the resonance. Since the goal of the THM is the determination of the energy dependence of the astrophysical factor at the astrophysically relevant energy, normalization of the TH differential cross section to the OES experimental astrophysical factor, is

necessary. In the THM, the HOES astrophysical factor is normalized to the OES $S(E_{xA})$ factor for the binary reaction which is given, for single resonance, by:

$$S(E_{xA}) = NF(E_{xA})\frac{d^3\sigma}{dE_{cC}d\Omega_{\mathbf{k}_{cC}}d\Omega_{\mathbf{k}_{sB}}} = \frac{\pi}{2\mu_{xA}}e^{2\pi\eta_{xA}}\frac{\Gamma_{Cc(\tau)}(E_{cC})\Gamma_{xA(\tau)}(E_{xA})}{(E_{Ax}-E_{R_\tau})^2+\frac{\Gamma^2_\tau(E_{xA})}{4}} \quad (3.30)$$

here η_{xA} is the Coulomb parameter of the x-A nuclei moving with the relative momentum $k_{xA}=\sqrt{2\mu_{xA}E_{xA}}$, and NF is the normalization factor given by:

$$NF(E_{xA}) = \frac{\pi}{k^2_{xA}}\frac{1}{\lambda_3}E_{xA}e^{2\pi\eta_{xA}}\frac{\Gamma_{xA(\tau)}(E_{xA})}{|M^{DW}_\tau(\mathbf{k}_{sB},\mathbf{k}_{aA})|^2} \quad (3.31)$$

generally depending on the A-x relative energy. The amplitude of $M^{DW}(\mathbf{k}_{sB},\mathbf{k}_{aA})$ remains practically constant over the interval of a few hundreds keV. Equation 3.31 is at the basis of the phenomenological procedure used in the TH analysis [La Cognata *et al.* (2007)].

The normalization factor can be obtained using the barrier penetration factor that appear in the R-matrix theory, $P(E_{xA})=\Gamma_{xA(\tau)}(E_{xA})/\Gamma_{xA(\tau)}(E_{R_1})$ that multiplies the factor $NF(E_{R_1})$, which can be found phenomenologically by comparing the experimental triple differential cross section with the available OES experimental astrophysical factor at the resonance energy. This normalization leads to the intermediate astrophysical factor:

$$S'(E_{xA}) = \frac{\pi}{2\mu_{xA}}e^{2\pi\eta_{xA}|E_{xA}=E_{R_1}}\frac{\Gamma_{Cc(\tau)}(E_{cC})\Gamma_{xA(\tau)}(E_{xA})}{(E_{Ax}-E_{R_\tau})^2+\frac{\Gamma^2_\tau(E_{xA})}{4}} \quad (3.32)$$

The final astrophysical factor can be derived by multiplying $S'(E_{xA})$ by the energy-dependent renormalization factor $e^{2\pi[\eta_{xA}-\eta_{xA}|_{E_{xA}=E_{R_1}}]}$. Thus normalization of the TH triple differential cross section to the experimental astrophysical factor at resonance energy plays a very special role in the TH method.

3.4 THM: validity test

Since the THM is an indirect method, validation is required before proceeding to its application to reaction of astrophysical relevance. Indeed, additional physical phenomena might be introduced by indirect methods that have to be identified

and disentangled. Moreover, the dependence of the results on the adopted theoretical approach has to be checked to evaluate what is its contribution to the systematic uncertainty. This is accomplished by comparing the direct and indirect cross sections above and below the Coulomb barrier. Moreover, the same two-body reaction has been studied by using two different target nuclei [Pizzone *et al.* (2003), Tumino *et al.* (2006)] and the results confirm that the method does not depend on the choice of the Trojan Horse nucleus. Finally, the THM application has been verified both when the nucleus A is a projectile or a target [Musumarra *et al.* (2001)]. A validity test of the THM is provided by the comparison of excitation functions and angular distributions extracted from direct and indirect measurements made at energies for which the electronic screening effect is negligible. The agreement between the trends of direct and THM data and is a necessary condition that must be met before extracting the astrophysical factor in the region where the contribution due to electron screening is present.

An example of the THM validity test is given in Figure 3.3. It shows the results obtained for the ^{7}Li(p,α)α reaction [Zadro *et al.* (1989)], studied through the $^{2}H(^{7}Li, \alpha\alpha)n$ process. The figure shows the comparison between direct (full line) and indirect data (black point) obtained by the THM using, in this case, the deuteron as the TH nucleus and the neutron as a spectator to the two-body reaction. The good agreement between the two data sets was a first validity test for the application of the method.

Recently, another test has been introduced to validate the pole independence of the binary cross section obtained through the THM. To this purpose the ^{7}Li(p,α)α reaction was studied using ^{3}He as the TH nucleus and deuteron as a spectator of the virtual two-body reaction [Tumino *et al.* (2006)]. Figure 3.4 shows the results; the black symbols are the THM data from the ^{3}He(^{7}Li,$\alpha\alpha$)d, the open one are the previous THM data from the ^{2}H(^{7}Li,$\alpha\alpha$)n reaction while the full black line stands for the direct data from [Englester *et al.* (1992)]. The good agreement between the three data sets is a strong evidence for the pole invariance in the THM application. In fact, according to the description of the method no hypothesis was made on the TH nucleus in the three-body process, so if the same participant is considered in the two-body reaction while the spectator differs, (neutron in the first measurement [Zadro *et al.* (1989)]or deuteron in the second

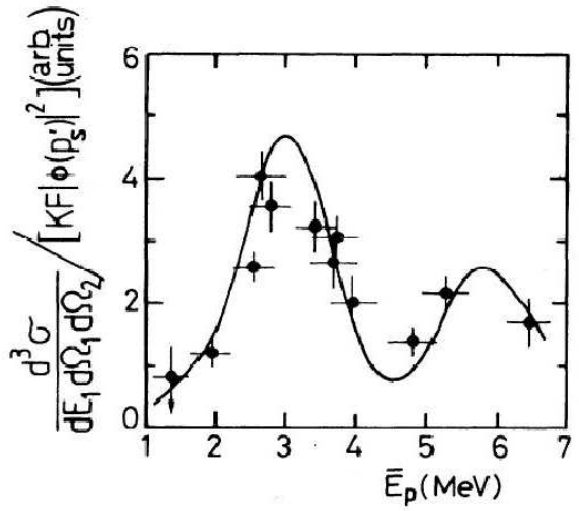

Figure 3.3: Comparison between the indirect (full dots) and the direct (solid line) excitation functions for the ^{7}Li+d$\rightarrow \alpha + \alpha + n$ reaction [Zadro *et al.* (1989)]. In this case the deuteron is used as the Trojan Horse nucleus and neutron as a spectator.

one [Tumino *et al.* (2006)]), the final result should not change. The validation of pole invariance allows us to reduce the error budget affecting the final THM result, by removing the model dependence of the extracted binary cross section.

3.5 Application of the Trojan Horse Method

In the last decade, the method has been applied to several reactions of astrophysical and nuclear physics interest. A list of the reactions studied by means of THM is given in Table 1 together with the relevant references.

In particular, in this table we can see the main topics investigated by the THM. In the following, we shortly review some of them and discuss the main results.

Primordial nucleosynthesis The ^{3}He(d,α)p and d(d,p,)t reactions have been extensively studied via the THM [La Cognata *et al.* (2005), Rinollo (2005)]. They are of interest for astrophysics and applied in physics. The knowledge of the bare nucleus cross section is important in the study of the primordial

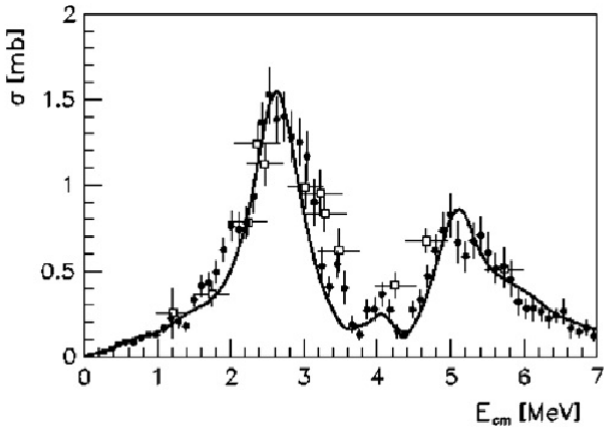

Figure 3.4: The total cross section for ^{7}Li(p,α)α extracted by using the $^{3}He(^{7}Li, \alpha\alpha)d$ three body reaction (black points)[Tumino *et al.* (2006)], compared with the Zadro *et al.* (1989) results, where the participant proton is transferred from the deuteron (open symbols), and with the direct data from Englester *et al.* (1992) shown as a full black line obtained by fitting the data.

nucleosynthesis, in particular to constrain the present-day models. On the other hand, they have been used to validate the most common models used to calculate the electron screening potential. In particular, reactions among light nuclei bear a great relevance as they might be used in fusion reactors, in the same energy range (E<100 keV) as astrophysics.

The fluorine problem in AGB star The Asymptotic Giant Branch (AGB) stage of stellar evolution represents the final nucleosynthesis phase for low and intermediate mass stars. The study of AGB stars is an important topic in astrophysics as they are a possible site for heavy-element production through slow neutron captures (*s-process*). In particular, the abundance of ^{19}F is very sensitive to the internal stellar structure and therefore provides a key parameter to constrain AGB-star and s-process models. When the theoretical abundances are compared to the observed ones, remarkable discrepancies (up to one order of magnitude) emerge revealing a poor understanding of the physical conditions under which ^{19}F is synthesized. Thus the study of nuclear reactions involved in ^{19}F production and destruction

Reaction studied via THM		
Two-body reaction	Three-body reaction	References
^{6}Li(d,α)α	^{6}Li(^{6}Li, $\alpha\alpha$)α	Pizzone *et al.* (2003)
^{6}Li(p,α)^{3}He	d(^{6}Li,α ^{3}He)n	Tumino *et al.* (2003), Pizzone *et al.* (2005)
^{7}Li(p,α)α	d(^{7}Li,$\alpha\alpha$)n	Pizzone *et al.* (2003)
^{7}Li(p,α)α	^{7}Li(^{3}He,$\alpha\alpha$)d	Tumino *et al.* (2006), Pizzone *et al.* (2005)
^{9}Be(p,α)^{6}Li	d(^{9}Be,α ^{6}Li)n	Romano *et al.* (2006)
^{10}B(p,α)^{7}Be	d(^{10}B,α ^{7}Be)n	Lamia *et al.* (2007)
^{11}B(p,α)^{8}Be	d(^{11}B,α ^{8}Be)n	Spitaleri *et al.* (2004), Romano *et al.* (2004)
^{3}He(d,p)α	^{6}Li(^{3}He,pα)α	La Cognata *et al.* (2005)
d(p,p)^{3}H	d(^{6}Li,p ^{3}H)α	Rinollo (2005)
^{15}N(p,α)^{12}C	d(^{15}N,α ^{12}C)n	La Cognata *et al.* (2006)
^{19}F(α,p)^{22}Ne	^{6}Li(^{19}F,p ^{22}Ne)d	La Cognata *et al.* (2006)
^{18}O(p,α)^{15}N	d(^{18}O,α ^{15}N)n	La Cognata *et al.* (2008)
^{17}O(p,α)^{14}N	d(^{17}O,α ^{14}N)n	Sergi *et al.* (2010)
^{6}Li(n,α)^{3}H	d(^{6}Li,α ^{3}H)p	Tumino *et al.* (2005)
p(p,p)p	d(p,pp)n	Tumino *et al.* (2007)

Table 3.1: list of reaction studied via THM

is needed. A key role is played by the ^{15}N(p,α)^{12}C reaction, which removes both ^{15}N and protons from the ^{19}F production chain in AGB stars. Also the ^{19}F(α,p)^{22}Ne and ^{18}O(p,α)^{15}N can affect fluorine abundances, the first one being the main ^{19}F destruction channel in the AGB inter-shell region, whereas the second reaction influences the production of ^{15}N that can modify the nitrogen supply in the burning chain producing ^{19}F. These reactions have been studied by means of the THM [La Cognata *et al.* (2006); La Cognata *et al.* (2008)]. Specifically, in the ^{18}O(p,α)^{15}N case the strength for the low-lying resonance sitting at 20 keV above the ^{19}F$\rightarrow$ ^{18}O+ p threshold has been experimentally determined for the first time, as shown in Figure 3.5.

Light-elements depletion problem The abundances of light elements, such as lithium, beryllium and boron (LiBeB in the following), plays a key role in

a number of not yet completely solved astrophysical problems, as explained in the first chapter. The (p,α) reactions on these nuclides are crucial as they constitute the main light-element destruction channel in stellar environments (E=1-50 keV). The cross sections are then necessary input for astrophysical models introduced to predict the light-element abundances in the universe. A great effort has been devoted to the study of the relevant reactions: ^{6}Li(p,α)^{3}He [Tumino *et al.* (2003), Pizzone *et al.* (2005)], ^{6}Li(d,α)^{4}He [Pizzone *et al.* (2003)], ^{7}Li(p,α)^{4}He [Pizzone *et al.* (2003); Tumino *et al.* (2006)], ^{9}Be(p,α)^{6}Li [Romano *et al.* (2006)], ^{11}B(p,α)^{8}Be [Spitaleri *et al.* (2004); Romano *et al.* (2004)] and ^{10}B(p,α)^{7}Be Lamia *et al.* (2007). The experimental study of the last two reactions is the subject of this thesis. For some of them, it has also been possible to extract the electron screening potential $(U_e)^{THM}$, in agreement with the direct $(U_e)^{dir}$ estimates. As an example, the figure 3.6 shows the astrophysical S(E)-factor for the ^{7}Li(p,α)^{4}He and ^{6}Li(d,α)^{4}He reaction cross sections, obtained with the THM. Both results confirmed the screening potential determined in direct measurements [Englester *et al.* (1992)]as well as the isotopic independence of the U_e value.

Nuclear physics application Besides nuclear astrophysics, the THM , has also been applied to studies of mostly nuclear physics interest.

- *Development of virtual neutron beams*: Recently, the THM was successfully applied to the d(^{6}Li,α^{3}H)p reaction with the aim to study the QF ^{6}Li(n,α)^{3}H reaction, where the Coulomb barrier suppression is absent [Tumino *et al.* (2005)]. The very good agreement with direct data in the literature validates the pole approximation for this experiment. This kind of application needs to be further confirmed also in the view of future applications to key astrophysical reactions using deuterons as a source of a virtual neutron beam.
- *p-p elastic scattering*: Another application of the THM concerns the indirect study of the *p-p* elastic scattering. It is well known that in such a simple process the interference terms between Coulomb and nuclear amplitudes are expected to contribute to the cross section.

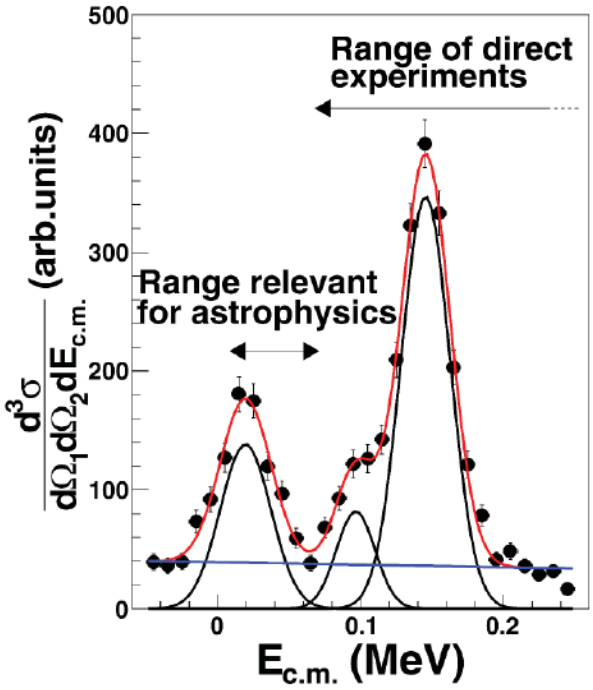

Figure 3.5: Cross-section of the d(^{18}O,α^{15}N)n THM reaction (full circles) for the reaction. The three Gaussian curves (black lines) refer to the three states in ^{19}F at 8.1014, 8.084, and 8.138MeV. The red line is the result of a fit including the three Gaussian curves and a first order polynomial (blue) for the background contribution.

In particular the combination of the two effects gives rise to a destructive interference which leads to a deep minimum in the cross section. The THM has been applied to the d(p,pp)n reaction [Tumino *et al.* (2007)]. In the THM hypothesis the Coulomb effects are suppressed in the two-body cross section at sub-Coulomb energies. For this reason, we can expect that the interference contribution should be absent and the two-body cross section should not display the deep minimum.
Figure 3.7 shows that the *p*-*p* cross section is completely dominated by the nuclear field as is expected in the higher energy region. This strongly confirms the Coulomb suppression hypothesis which makes the THM the unique experimental method able to investigate nuclear

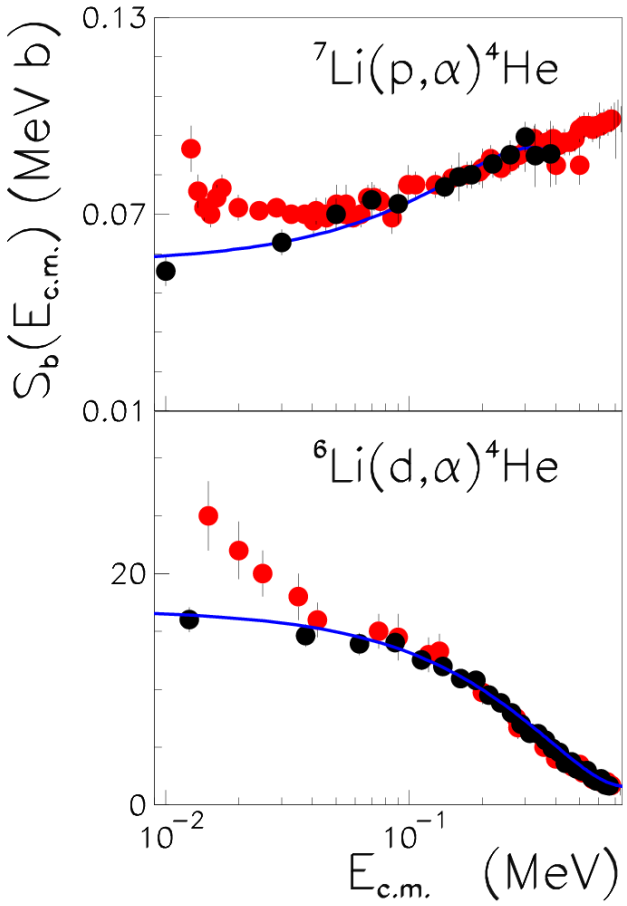

Figure 3.6: (top) Bare-nucleus astrophysical S_b(E)-factor extracted by means of the THM (black dots) for the ^{7}Li(p,α)^{4}He reaction. The direct data from Englester *et al.* (1992) are shown as a red circle.(bottom) Bare-nucleus astrophysical factor for the reaction ^{6}Li(d,α)^{4}He (black dots), compared with the direct data (red symbols [Englester *et al.* (1992)].

effects at low energies, not only in the framework of nuclear astrophysics.

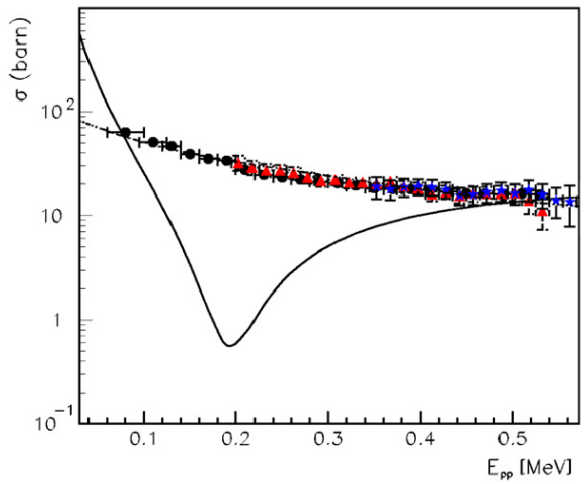

Figure 3.7: The THM two-body cross section versus *p*-*p* relative energy. The figure has been extracted from [Tumino *et al.* (2007)]. Black dots, red triangles and blue stars are referred to different experimental THM works. Solid line and dashed-dotted line represent the calculated p-p cross section as described in [Tumino *et al.* (2007)].

Chapter 4

Study of ^{10}B(p,α)^{7}Be reaction through the THM

In the context of depletion of light elements, as mentioned in the previous chapters, the study of the ^{10}B(p,α)^{7}Be plays a fundamental role in order to understand several astrophysical problem. In particular the ^{10}B(p,α)^{7}Be reaction is the main responsible for the ^{10}B destruction in stellar interior. This reaction was studied indirectly through the THM applied to the ^{2}H(^{10}B,α^{7}Be)n three-body reaction. The importance of this reaction is due to the presence of a resonance related to the ^{11}C* excited state (J=5/2^{+}, E$_x$=8.701MeV) which corresponds to the center of mass energy E$_{cm}$=10 keV. Moreover this resonance lies in the Gamow peak region so that the determination of the S(E)-astrophysical factor, in such energy region, becomes crucial. The aim of this analysis was to study the energy region corresponding to the Gamow peak where the direct measurements present only an extrapolation. In this sense we will see the status of the art for this reaction and we will see all the stages of the data analysis that allowed us for the subsequent extraction of the S(E)-astrophysical factor.

4.1 Status of the art

The direct data present for the ^{10}B(p,α)^{7}Be reaction are reported in NACRE compilation and are shown in Figure 4.1. This figure reports all the data present in the literature, including data from Angulo *et al.* (1993) and reference therein,

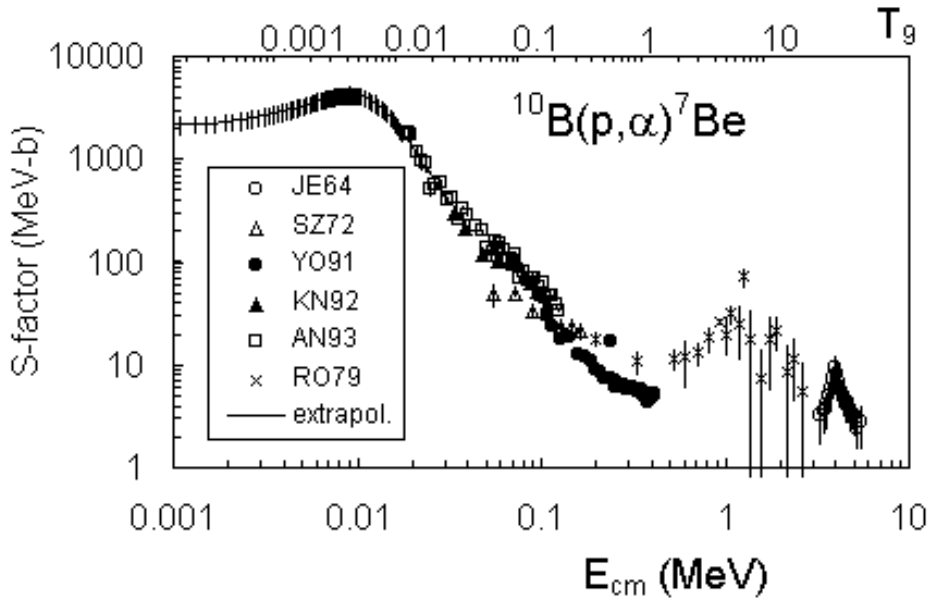

Figure 4.1: Astrophysical S(E)-factor for the ^{10}B(p,α)^{7}Be reaction reported in NACRE compilation. The different points represent different measurement present in the literature. The region of our interesting is the low-energy region where are present the data from Angulo *et al.* (1993)

to which we are interested since we want to study the low energy region. In this article is reported the S(E)-astrophysical factor from ∼400 keV down to ∼18 keV, while in the lower energy region, where a contribution of the ^{11}C excited state at E_x=8.701 MeV is expected, they made a theoretical determination of the S(E)-factor in terms of single level Breit-Wigner shape. In such theoretical determination they used the resonance parameter as deduced in the work of Wiescher *et al.* (1983), in which the 8.701 ^{11}C level was observed through the study of ^{10}B(p,γ)^{11}C reaction. Using this approach, the authors extracted a value of S(10)=2.87×10^3 (Mev b). Recently, the ^{10}B(p,α)^{7}Be has been studied via the THM applied to the ^{2}H(^{10}B,α ^{7}Be)n three-body process.This first experiment was performed at E_{beam}= 27 MeV energy beam at the Istituto de Fisica Nuclear de Sao Paulo (Brazil). The results of the S(E)-factor for the 10 keV resonance was quite in disagreement with the extrapolation performed by Angulo et al. (1993) as shown in figure 4.2 [Lamia *et al.* (2007)]. For this reason a new experiment

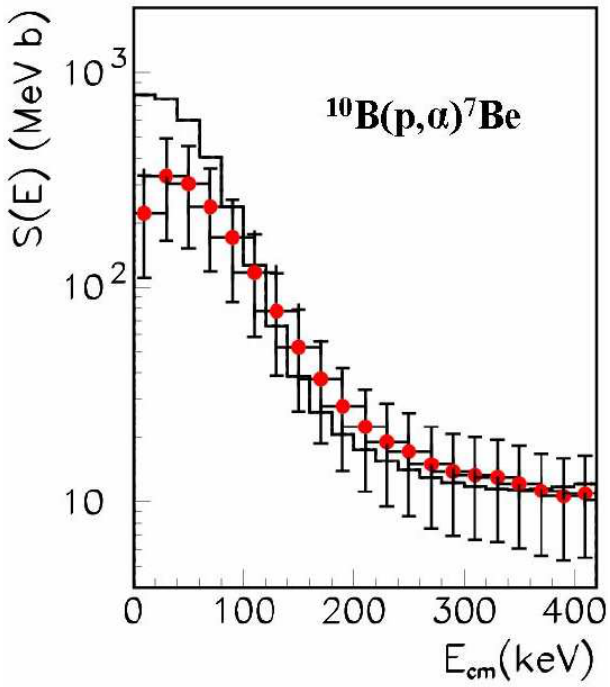

Figure 4.2: Astrophysical S(E)-factor for the ^{10}B(p,α)^{7}Be reaction obtained in the first experiment performed by using the THM [Lamia *et al.* (2007)]. The THM data (red point) were compared with the extrapolation reported in Angulo *et al.* (1993) (histogram).

with a higher accuracy was performed, and the results will be discussed in this thesis.

4.2 The THM approach: kinematical conditions

The ^{10}B(p,α)^{7}Be (Q=1.144 MeV) reaction has been studied with the THM. In the previously chapter we have seen the hypothesis to be tested for the applicability of the method. According to the assumption described above in order the study of the ^{10}B(p,α)^{7}Be reaction, the selection of QF-contribution of the ^{2}H(^{10}B,α^{7}Be)n (Q=-1.079 MeV) three-body reaction, is necessary.

Figure 4.3 represent a Pseudo-Feyman diagram for the QF contribution of the

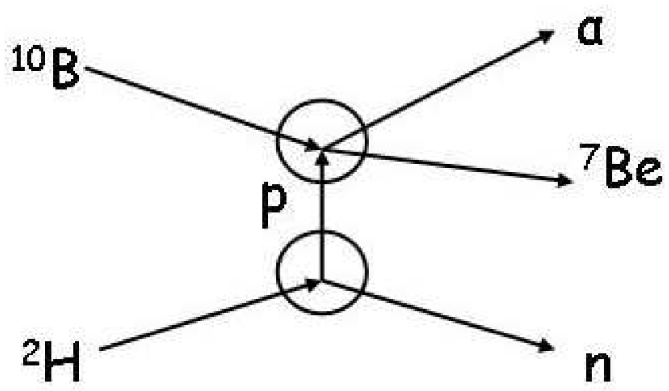

Figure 4.3: Pseudo-Feyman diagram for the QF process ^{2}H(^{10}B,α^7Be)n. The escaping neutron is considered as a spectator to the process, while the transferred proton interact only with the ^{10}B.

^{2}H(^{10}B,α^7Be)n reaction, proceeding through deuteron break-up. In this figure the upper pole represents the virtual two body reaction and the lower pole represents the break-up for the deuteron used as the TH nucleus. The choice of deuteron as the TH nucleus is due to two main different reasons [Tumino *et al.* (2003), Spitaleri *et al.* (2001)]; deuteron nucleus has a simpler cluster structure consisting of two nucleons and can therefore be described as d=p$\oplus$n with binding energy B_{p-n}=2.2 MeV; moreover the relative momentum distribution of intercluster motion inside the deuteron, being the Fourier transform of the relative motion wave function in the coordinate space, is well known from independent experiment [Zadro *et al.* (1989)]. Since the relative motion of the neutron-proton system inside the deuteron takes place essentially in s-wave (l=0), and the QF break-up occurs in the target nucleus, the experimental momentum distribution correspond is expected to be peaked at p_n=0. Its analytical expression is given in terms of Huthén wave function [Zadro *et al.* (1989)] and its shape is shown in Figure 4.4 where is evident the maximum at relative momentum p_n=0 Mev/c. As regards the beam energy, the main physical constraint is connected to the hypothesis that the energy of the impinging particles exceeds the Coulomb barrier in the entrance channel of the three-body reaction, this allows to extract the cross section

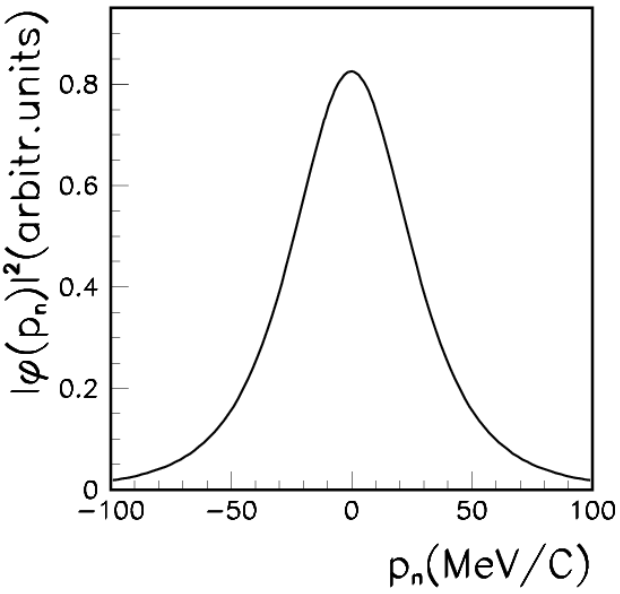

Figure 4.4: Hulthén function that describes the behavior of the momentum distribution of inter-cluster motion inside the deuteron [Zadro *et al.* (1989)].

of the astrophysical reaction of interest free of Coulomb suppression. Thus in the present case the beam energy in the center-of-mass system of the ^{10}B+d channel exceed about 1.8 MeV, that is the Coulomb barrier evaluated by means of equation 2.14. In order to determine the beam energy using the formula described in the previous chapter:

$$\Delta E_{QF} = E_{ax} - B_{xs} \pm E_{xs} \tag{4.1}$$

our goal is the study of the energy region corresponding to the resonance at 10 keV. Then assuming the ΔE_{QF}=10 keV $\pm$ E_{xs} and using the deuteron binding energy B_{xs}=2.2 MeV it is obtained:

$$E_{ax} = E_{beam} \cdot \frac{m_p}{m_p + m_{10B}} = 2.21 MeV \Rightarrow E_{beam} = 24.4 MeV \tag{4.2}$$

where m_p and $m_{^{10}B}$ are the proton and boron mass expressed in atomic mass unit. Once that the beam energy is fixed, it is possible to perform a detailed study of the simulated-kinematical condition for the chosen three-body reaction

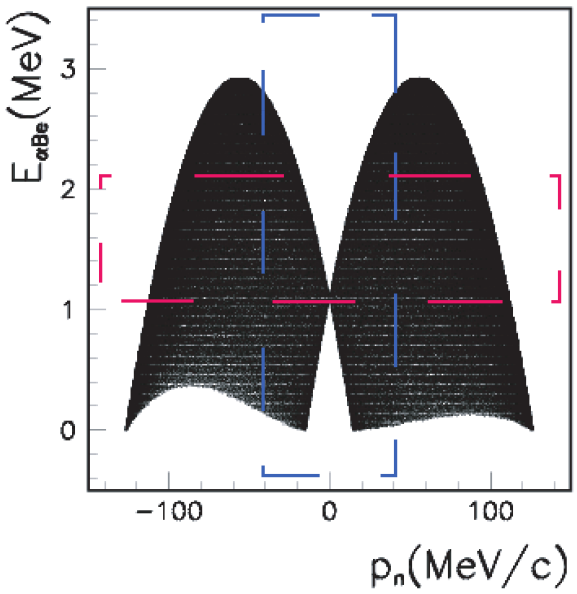

Figure 4.5: Simulated "butterfly diagram", the energy region of astrophysical interest is highlighted by red dashes and it is reached for 'low' momentum value within the blue dashes box.

at this energy. In order to select the region in which a strong QF contribution to the three body reaction is expected, the study of the relative energy $E_{\alpha Be}$ as a function of a neutron momentum is useful. Using the beam energy as obtained before, the named "butterfly diagram" has been calculated by Monte Carlo simulation (Fig.4.5). In Figure 4.5 is evident that the energetic region of interest for astrophysics corresponds to the low momentum for the neutron, the selection of such values for the neutron momentum corresponds to the selection of a region in which a strong QF contribution is expected. Therefore, a detailed study of a Monte Carlo simulation to establish the kinematical condition corresponding to the QF-contribution, was carried out. Figure 4.6 shows with black points the simulated emission angles of both α and ^{7}Be particles of the three-body exit channel (left panel) and the kinematical locus for the three-body reaction ^{2}H(^{10}B,α^7Be)n (right panel). In this figure the red points define the condition at which the momentum p_n of the undetected third particle is $|p_n|$<30 MeV/c.

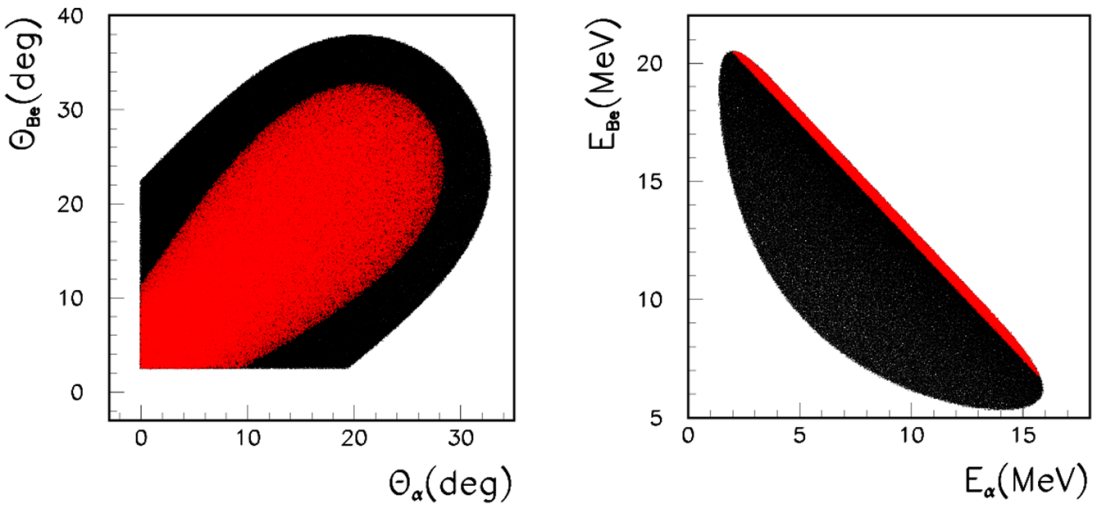

Figure 4.6: Left panel: Simulation of the whole angular range for α and Be particles in the exit channel(black points). Red points represents the condition for $|p_n|<30$ MeV/c in which is expected the strong QF contribution. Right panel: Simulation of the kinematical locus for the three-body reaction ^{2}H(^{10}B,α^7Be)n, also in this case, the region with red points represent the events with $|p_n|<30$ MeV/c.

This value was chosen according to the QF break-up conditions for which the undetected third particle has in the exit channel the same momentum that had before the interaction with the projectile. The angles corresponding to this condition are known as QF angles.

4.3 Experimental setup

The experiment was performed at the Laboratori Nazionali del Sud in Catania. The Tandem Van de Graaf accelerator provided at 24.4 MeV ^{10}B beam that was accurately collimated in order to achieve a beam spot on the target of about $2mm$ diameter. The beam intensity up to 1.5 nA. Thin self-supported deuterated polyethylene target (CD_2)$\approx$192 g/cm^2 thick, was adopted in order to minimize energy and angular straggling and was placed at 90° with respect to the beam direction. The detection setup, sketched in Figure 4.7, consisted of a telescope (A), made up of an ionization chamber (IC) and a silicon position sensitive de-

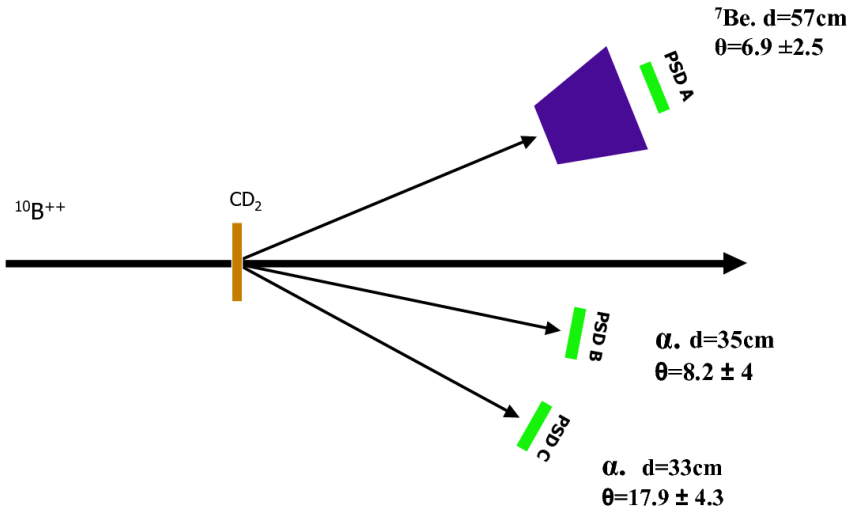

Figure 4.7: Experimental setup displacement in the scattering chamber of LNS. The two PSD (PSD_B, PSD_C) and the ionization chamber devoted to ^{7}Be detection are evident.

tector (PSD_A). It was devoted to the ^{7}Be detection on one side with respect to the beam direction and was placed at a distance of about 57 *cm* from the target. The ionization chamber was used to discriminate the beryllium nuclei by means of the standard ΔE-E technique (as explained below). Two additional silicon PSDs (PSD_B, PSD_C) were placed on the opposite side with respect to the beam direction at the angles 8.2° ± 4° (PSD_B), 17.9°± 4.3° (PSD_C) and at a distance d_B=35 *cm* and d_C=33 *cm* from the target, respectively. Angles and distances for each PSD are summarized in table 4.1. In order to minimize the angular straggling in the IC a 1 μm thick Mylar foil was used as the entrance window.

The IC was filled with about 40 *mbar* butane gas that provided an energy resolution of about ten per cent which was enough to discriminate the impinging particles according to their nuclear charge but not their mass.
Angular conditions were selected in order to maximize the expected QF contribution. Indeed, they were chosen to cover momentum values of the undetected neutron from 0 to 150 MeV/c.

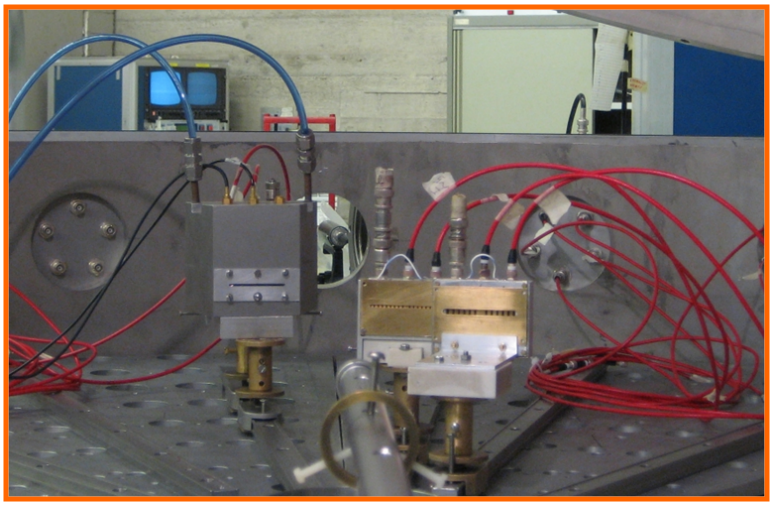

Figure 4.8: Picture of the scattering chamber located at LNS. The two PSD (PSD_B, PSD_C) as well as the ionization chamber are mounted, PSD_B and PSD_C are clearly visible in the right side, while PSD_A, put behind the ionization chamber is not visible.

Thus, the bulk of the QF contribution for deuteron break-up fall inside the investigated region because the momentum distribution for the p-n system has a maximum at p_n=0 MeV/c. The wide explored momentum range allows for a cross check of the method inside and outside the phase space region where the QF contribution is expected. To decrease the detection threshold, no ΔE detectors were put in front of PSDs B and C, therefore α-particle identification was done from the kinematics of events. Energy and emission angle of the detected α's and emission angle of ^{7}Be nuclei were used in the subsequent analysis to enhance energy resolution. Two kinds of events were triggered by using a time-to-amplitude converter (TAC): A-B, A-C coincidences. Energy and position signals of the PSDs were processed by standard electronics together with the TAC signal for each coincidence event and sent to the acquisition system for on-line monitoring and data storage for off-line processing.

Detector	Angle (deg)	Angular range (deg)	Distance (cm)
PSD_A	6.9	4.4-9.4	57
PSD_B	8.2	4.2-12.2	35
PSD_C	17.9	13.4-22.4	33

Table 4.1: Angular position and distance for the three PSDs.

4.4 Detectors calibration

Before the data analysis procedure is necessary to calibrate all detectors involved in our experimental setup. Since for the application of the method is necessary to have information about the relative energies between the outgoing particle, that is correlated to the angles and energy of the involved product, the measurements of both quantities, energies and angles, is needed. In this sense the detector used are Position Sensitive Detectors (PSD) that gives information about the energy of the particle and moreover the position at which the particle penetrates the detectors, so it is possible to obtain two signals: energy and position (*E,P*).

From the pattern of operation of PSD shown in figure 4.9 it is possible to observe that they consist of two electrodes: one uniform and resistive, and the other whit lower resistivity. The position signal P is taken from one end of the electrode resistive and is obtained by partition of the charge produced by the incident particle, while the energy signal E is taken from the electrode with a lower resistivity. The position signal is proportional to the energy according to the equation:

$$P \propto E\frac{x}{L} \tag{4.3}$$

where x is the distance between the point of incidence of the ion and the opposite extreme to the collection of charges and L is the length of the resistive layer. Therefore, one of the main aims of the position calibration is to remove the energy dependence of the position signal, as discussed in the following section. The used PSD's have a 0.5 mm position resolution and an energy resolution better than 1% while their surface area is about 50×10 mm^2 . The two signals, position P and energy E are taken from each detector and converted by the Amplitude

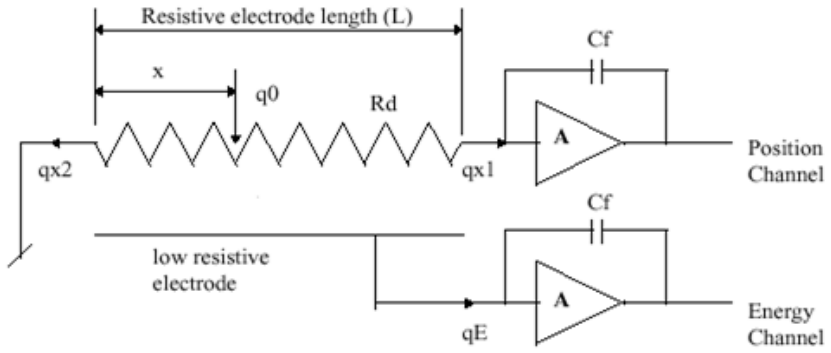

Figure 4.9: Detailed drawing in which the basic principle of the position sensitive silicon detector employed in the experiment is shown. In the resistive electrode the total charge produced Q_E is divided so that the larger is the signal and smaller is the resistance.

Digital Converter (ADC) channels. Therefore it is necessary a calibration of the detector in energy and in position to get a suitable relationship energy-channel and channel-position-angle. The detectors were calibrated in position and energy by using the data from $^{12}C(^{6}Li,\alpha)^{14}N$, $^{12}C(^{6}Li,^{6}Li)^{12}C$, $^{197}Au(^{6}Li,^{6}Li)^{197}Au$ reactions and from α-source.

4.4.1 Position calibration

At the initial stage of the measurement, grids with a number of equally spaced vertical slits were placed in front of the PSD in order to perform position calibration. The angle of each slits with respect to the beam direction was measured by means of an optical system, making possible the correspondence between position signal from the PSDs and detection angle of impinging particles. Figure 4.10 shows the distribution of events in the plane P_{ch}- E_{ch}, where P_{ch} and E_{ch} represent the position and energy signal respectively expressed in channels.
In this figure the contribution of each slits is evident, if one selects a slits, it will be possible found a linear dependence between the position and energy signal. The corresponding pairs P_{ch}-E_{ch}, for each slit, were then placed in a linear fit of the type:

$$P_{ch} = a_i(\theta) \cdot E_{ch} + b_i(\theta) \tag{4.4}$$

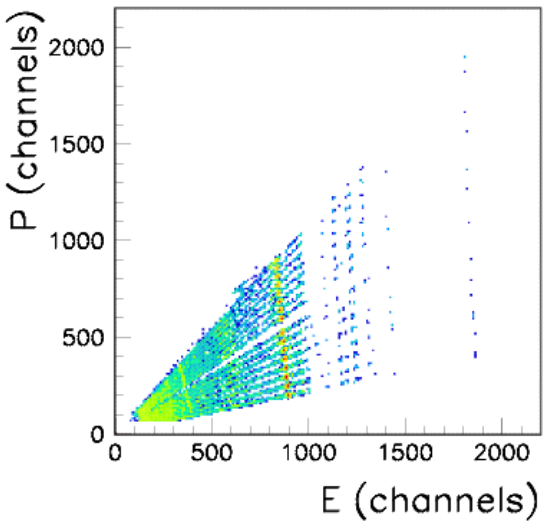

Figure 4.10: Two-dimensional position-energy spectrum of a PSD. Both position and energy are expressed in channels. The slit contribution is clearly visible.

The coefficients a_i and b_i are different for each slit and their angular dependence is almost linear:

$$\begin{aligned} a_i(\theta) &= a_0 + a_1 \cdot \theta \\ b_i(\theta) &= b_0 + b_1 \cdot \theta \end{aligned} \tag{4.5}$$

Putting together 4.4 and 4.5, then, it is possible to get a single relationship between both signals not yet calibrated, and then again expressed in channels, and the angle of the emitted particle:

$$\theta(deg) = \frac{P_{ch} - a_0 E_{ch} - b_0}{a_1 E_{ch} + b_1} \tag{4.6}$$

4.4.2 Energy calibration

Energy calibration was performed with a standard three-peaks α source (^{241}Am at 5.16 MeV ,^{244}Cm at 5.48 MeV and ^{239}Pu at 5.80 MeV), and by means of the events coming from the ^{12}C(^{6}Li,α)^{14}N reaction (Q=6.798 MeV, E=9.02 MeV),

the ^{6}Li scattering on CD_2 (E_{beam}=9.2 MeV) and on Au (E_{beam}=27.2 MeV) and the ^{6}Li+d$\rightarrow\alpha+\alpha$ reaction (Q=22.372 MeV, E=9.2 MeV) which, due to its high Q-value, represent a good α-source for the higher energy region. Assuming that the existing proportionality between the energy of the incident particle and the associated channels is not significantly perturbed by nonlinear effects deriving from associated electronics, the law that regulates the energy-channel correspondence as a function of a given incident angle θ can be written as:

$$E = a(\theta) + b(\theta) \cdot E_{ch} \tag{4.7}$$

where E is energy in MeV of the ion detected. The energy spectrum for different angles of the detector was reconstructed and the peaks corresponding to different reaction were identified. The energy to be associated to each peak is calculated taking into account the energy loss of the incident beam and of the reaction products in the half thickness of the target where the reaction is assumed to take place.
The energy loss of incident particles were calculated, considering the variation of the target thickness as a function of the output angle of the particle relative to the direction of the beam. For the detector PSD_A was taken into account also the energy loss in the gas (butane at a pressure of 40 mbar) present in the ionization chamber placed in front of the detector. Figure 4.11 shows a calibrated energy-angle plot.

4.5 Data analysis: Reaction channel selection

After the calibration of the involved detectors, the first step in the A-B, A-C coincidences analysis is the identification of the events corresponding to the ^{2}H(^{10}B,α^7Be)n three-body process. This is accomplished first through a selection of the beryllium locus in the ΔE-E two-dimensional plot as shown in figure 4.12. The channel selection procedure begins with the beryllium locus in the ΔE-E two-dimensional plot by means of a graphical cut and only the corresponding events are used for the further analysis. After particle identification the E_{Be} vs E_α plot was reconstructed.

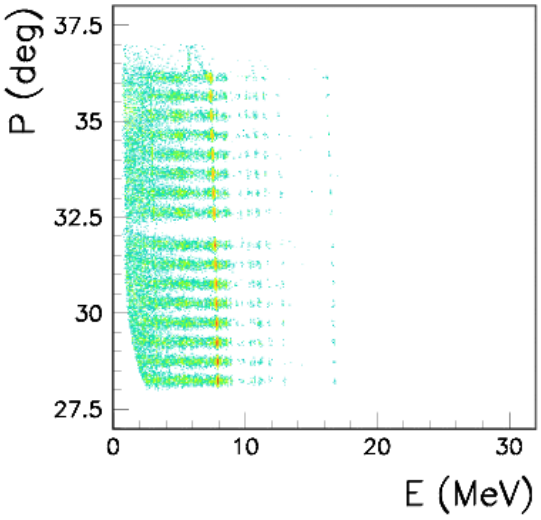

Figure 4.11: Typical plot of the calibrated PSD.

The locus corresponding to the ^{2}H(^{10}B,α^{7}Be)n reaction was singled out by a comparison with a Monte Carlo simulation of that process, taking into account detection threshold, energy losses and the kinematics of the TH reaction. An example of E_{Be} vs E_{α} energy correlation plots is given in figure 4.13.

This result is supported also by the experimental Q-value spectrum where a single peak is centered at the energy of about -1 MeV (see Figure 4.14) which well agree with the theoretical value ($Q_{theoretic}$ = -1.075) and confirms not only the identification of the reaction channel but also the accuracy of the performed calibration. Similar results are reproduced for both the A-C and A-B pairs, as shown in the figure. Thus, in the subsequent analysis only events following inside the peak were selected and used for the further analysis. In the Figure 4.15 a comparison between a simulation and the selected experimental data is reported for A-B and A-C coincidences as a further test of the good selection of the three-body channel and our good calibration.

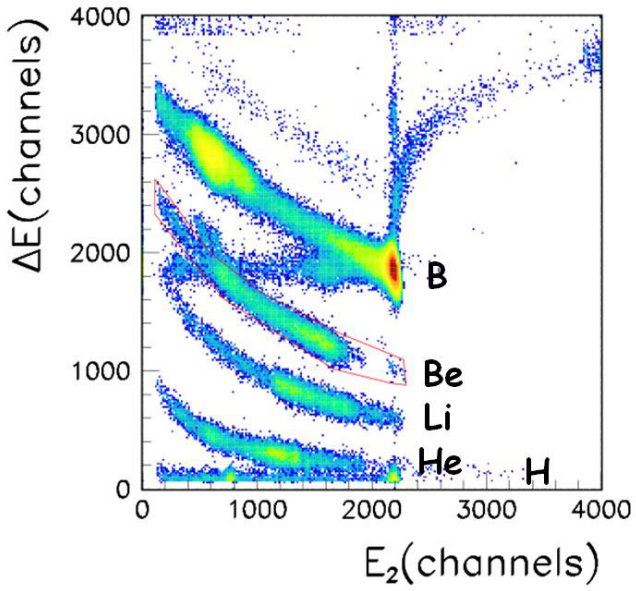

Figure 4.12: ΔE-E two-dimensional plots for the A telescope, useful for particle charge identification. Data from both A-B and A-C coincidence provides similar results. Beryllium locus clearly shows up and is evident the graphical cut that gives a selection of Be particles used for the further analysis.

4.5.1 Selection of QF Reaction Mechanism

After the selection of the three-body reaction ^{2}H(^{10}B,α^{7}Be)n of interest, the next step in the data analysis was to establish whether in the selected experimental kinematic region the contribution of the QF process is evident and well separated from the other possible reaction mechanism.

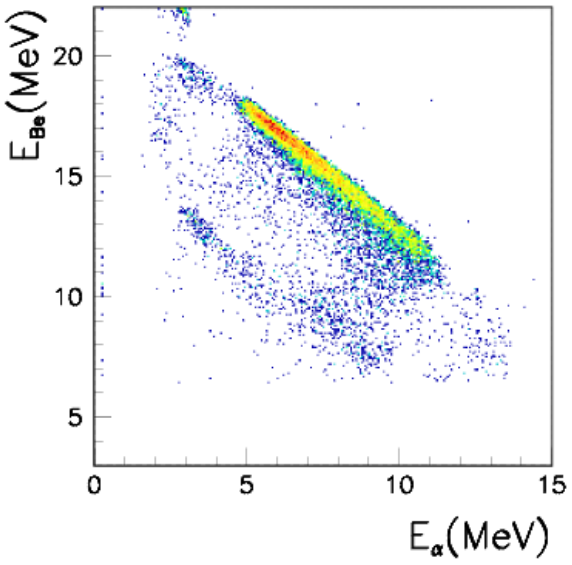

Figure 4.13: Kinematical locus for the three-body reaction after a selection of Be particle.

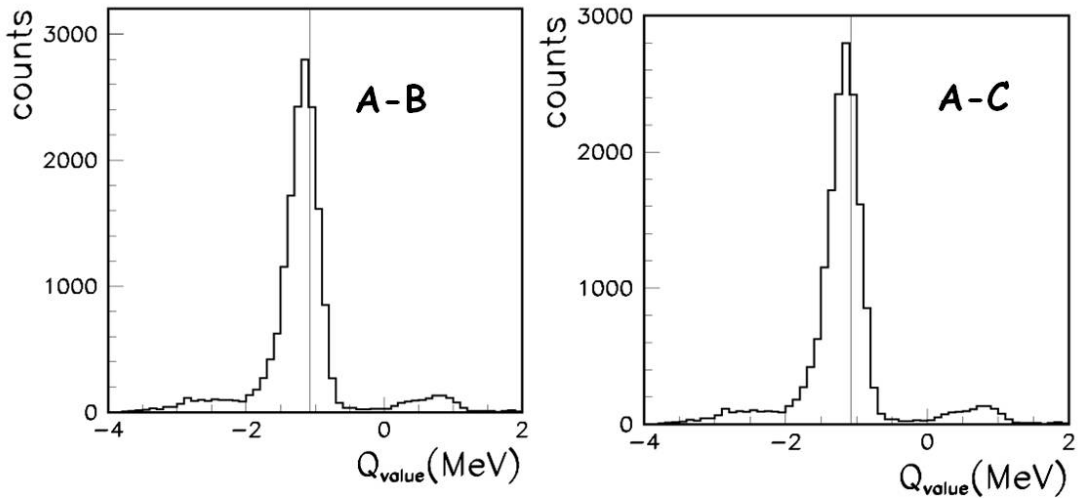

Figure 4.14: Reconstructed Q-value spectrum for the three-body ^{2}H(^{10}B,α^{7}Be)n reaction for both A-B and A-C pairs. The experimental value (Q_{exp}-1 MeV) must be compared with the theoretical one (Q_{the}=-1.079 MeV).

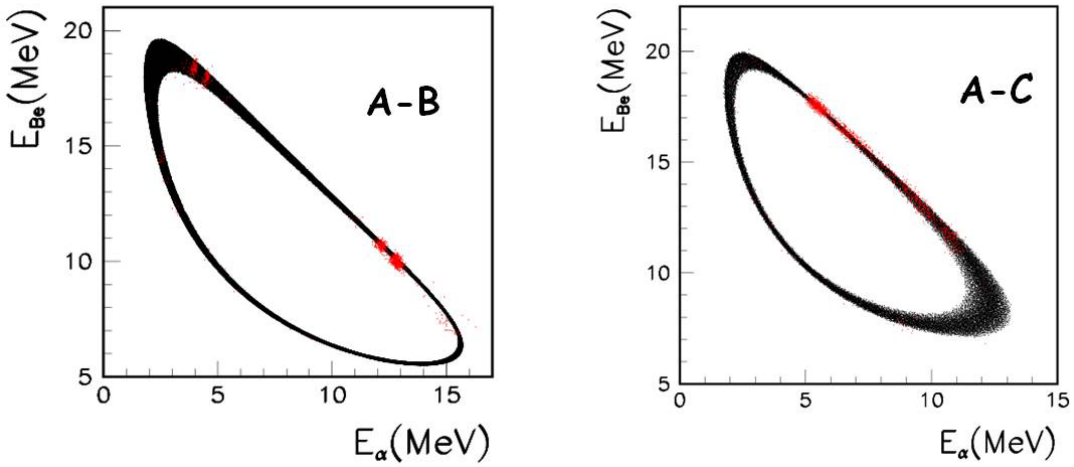

Figure 4.15: Three-body reaction ^{2}H(^{10}B,α^{7}Be)n kinematical locus for the events following inside the peak in Fig 4.14. (red points) compared with the calculation (black points) for the A-B pair in the left panel and A-C pair in the right one. Is evident the good agreement that confirm the precise selection of the three-body reaction of interest.

This is an essential step because the equations needed for THM application are valid only under the assumption that the neutron acts as spectator in the ^{10}B-d interaction. This is accomplished by a study of the reaction dynamics to disentangle the different processes feeding the exit channel, in the same way a study of the reactions kinematics was demanded to figure out the contribution from contaminant reaction channels. In fact the α and Be particles in the exit channel could be derived from mechanism, as sequential decay (SD), that are not of interest for our investigation as shown in figure 4.16. Therefore, an exhaustive study of those reaction mechanism is necessary step to disentangle the QF from other "background" processes.

4.5.1.1 Study of relative energy spectra

In order to study the reaction mechanisms for the events belonging to the kinematic locus for the ^{2}H(^{10}B,α^{7}Be)n reaction the two-dimensional plots showing the relative energies for the α-^{7}Be, α-n and ^{7}Be-n system were deduced from the measured energies and emission angles. Of course, the relative energy spectra represent the excitation energy spectra for ^{11}C, ^{5}He and ^{8}Be respectively. It means

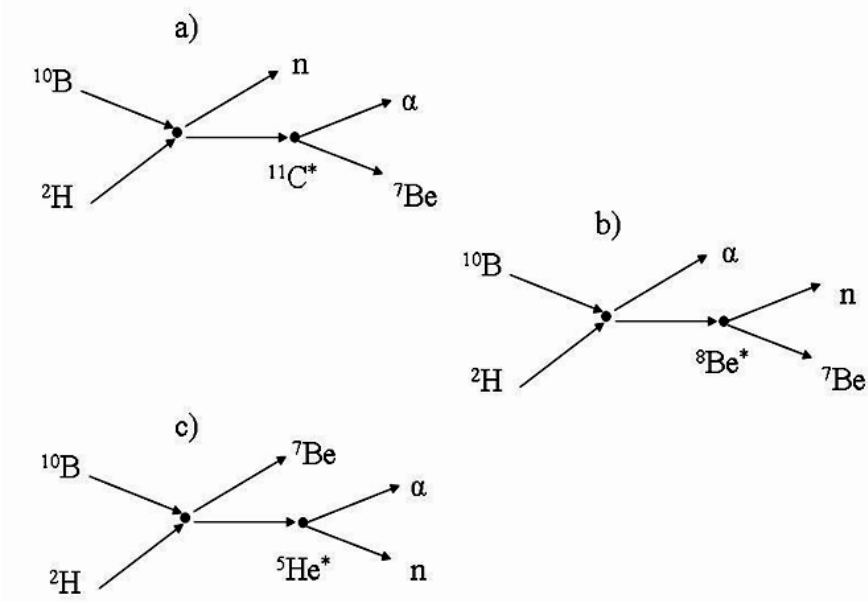

Figure 4.16: Different possible reaction mechanism to the same final state. In particular Sequential mechanism coming through the ^{11}C,^{5}He ^{8}Be intermediate state.

that if any state in such compound system has been fed in the investigated phase-space region, a bump in the reaction yield should up at the energy corresponding to the populated excited level. The relative energies $E_{\alpha-n}$ and E_{Be-n} are given in Figure 4.17 as a function of $E_{\alpha-Be}$ relative energy for the A-B coincidence and in figure 4.18 for the A-C coincidences.

No horizontal loci, corresponding to resonances in the ^{5}He compound nucleus are evident, showing that the ^{10}B+d$\rightarrow^{5}$He+^{7}Be$\rightarrow^{7}$Be+α+n two-step (^{5}He-SD) process is not important. Similarly, the ^{10}B+d$\rightarrow\alpha+^{8}$Be$\rightarrow^{7}$Be+α+n two-step reaction would lead to the formation of an intermediate ^{8}Be excited system (SD mechanism). Since no horizontal loci are apparent in the Figure 4.17 and 4.18 we can conclude that in the examined phase-space region the ^{5}He and ^{8}Be sequential decay is less favored process. We can state that such sequential process (through ^{5}He and ^{8}Be) give a negligible contribution to the coincidence yield α-^{7}Be relative energies. On the other hand, clear vertical loci appear in both the 2D-plots at about $E_{\alpha-Be}\approx$0.8 and $E_{\alpha-Be}\approx$1.1 MeV corresponding to excited states of ^{11}C at 8.42 MeV ($J^{\pi}=5/2^{-}$), 8.701 MeV ($J^{\pi}=5/2^{+}$) (figure 4.19).

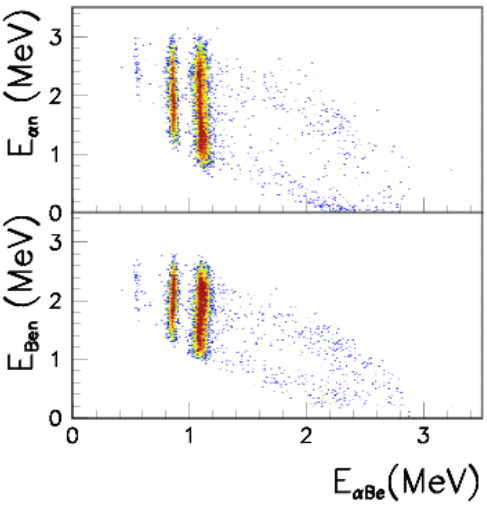

Figure 4.17: Energy correlation two-dimensional spectra for the A-B coincidences, also for this pair is evident the vertical loci correspond to ^{11}C excited states

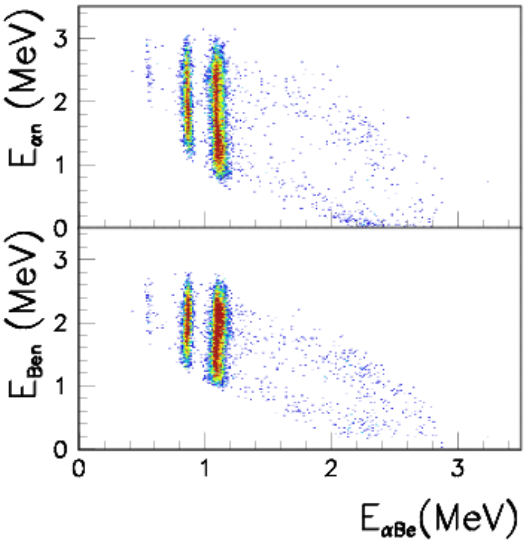

Figure 4.18: Energy correlation two-dimensional spectra for A-C coincidences. $E_{\alpha-n}$ vs $E_{\alpha-Be}$ and E_{Be-n} vs. $E_{\alpha-Be}$relative energy respectively. Clear vertical loci correspond to ^{11}C excited states. No additional loci are apparent, i.e. no sequential decay process is contributing.

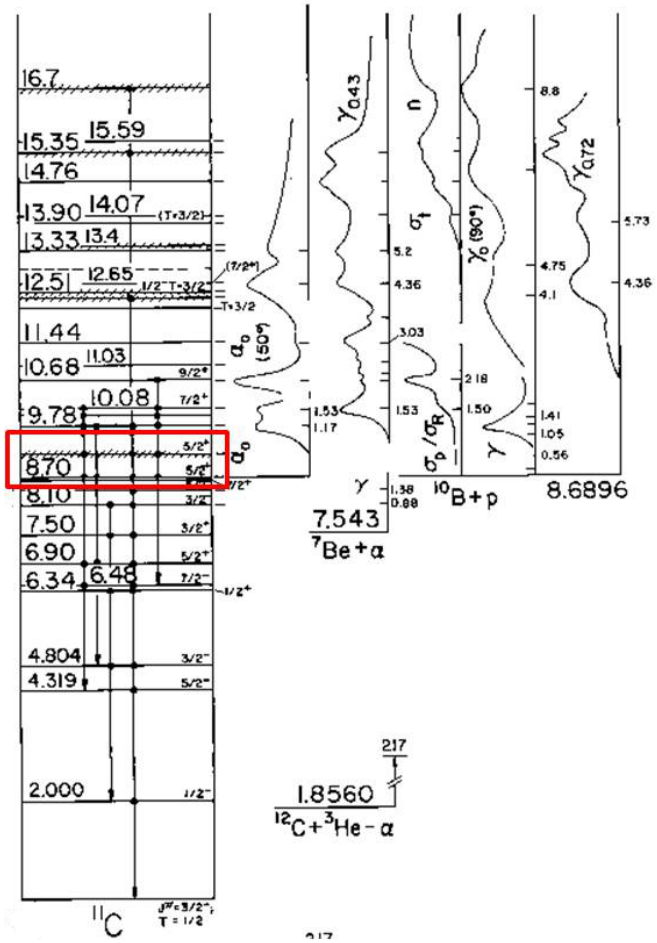

Figure 4.19: Scheme of the level of ^{11}C [Ajezenberg-Selove (1988)]. In the red box is evident the region of our interest correspond to the level at 8.701 MeV ($J^{\pi}=5/2^{+}$).

These levels can be formed either through the QF reaction mechanism , following deuteron direct breakup, or via a two-step SD process. Thus, the occurrence of sequential mechanism in the α-^{7}Be channel cannot be ruled out by studying the relative energy correlation plots only, because the same excited states of the α-^{7}Be system can be formed through a QF or SD process.

4.5.1.2 Angular correlation

Before any data extraction, next step of the analysis, is the study of the reaction mechanism involved in the exit channel of the 3-body reaction of interest. As

we already point out, the QF angles designate the angular condition where the QF mechanism is favored. Therefore the analysis of angular correlation spectra constitutes a test allowing to study the reaction mechanism involved in the population of the ^{11}C states free of space-phase effects. A way to investigate the reaction mechanism and therefore the nature (QF or SD) of these level is the angular correlation analysis on the data in order to point out the modulation of the three-body cross section by a neutron moment distribution inside deuteron.

Figure 4.20 shows typical coincidence spectra for the A-C coincidences projected on the ^{7}Be axis and corrected for the phase-space effects, for a fixed θ_{Be} and for three different θ_α angles. In the upper panel the E_{7Be} spectrum is displayed as obtained in correspondence of two QF angles (given in figure). In the other two, instead the spectrum has been extracted for other two couples, not matching the QF condition. This result demonstrate that the coincidence yield is larger for the QF angles and decrease while moving toward larger p_n value. From the sequence of these spectra it can be observed that the coincidence yield attains a maximum when a neutron momentum approaches zero value. This features is expected for a QF reaction because the momentum distribution of the p-n system inside deuteron has a maximum for p_n=0 MeV/c. Similar results have been obtained for other QF angular pairs and in similar way for A-B coincidences.
Also in this case the enhancement of the cross section close to zero p_n momentum is evident. These experimental spectra show a strong correlation between the coincidence yield and the neutron momentum p_n, and represent a first check for the existence of the QF mechanism in the ^{10}B(p,α ^{7}Be)n reaction.

4.5.1.3 Data as a Function of the Neutron Momentum

As a second stage of the investigation about the presence of the QF mechanism and the discrimination between the two mechanisms (QF or SD) is through the study of the reaction yield as a function of the neutron momentum p_n. Indeed, the occurrence of sequential mechanism in the α-^{7}Be channel cannot be ruled out by studying the relative energy correlation plots only since the same excited state of the α-^{7}Be system can be formed through both a QF reaction mechanism and a sequential one. Instead the investigation of the $E_{\alpha-Be}$ vs. p_n two-dimensional

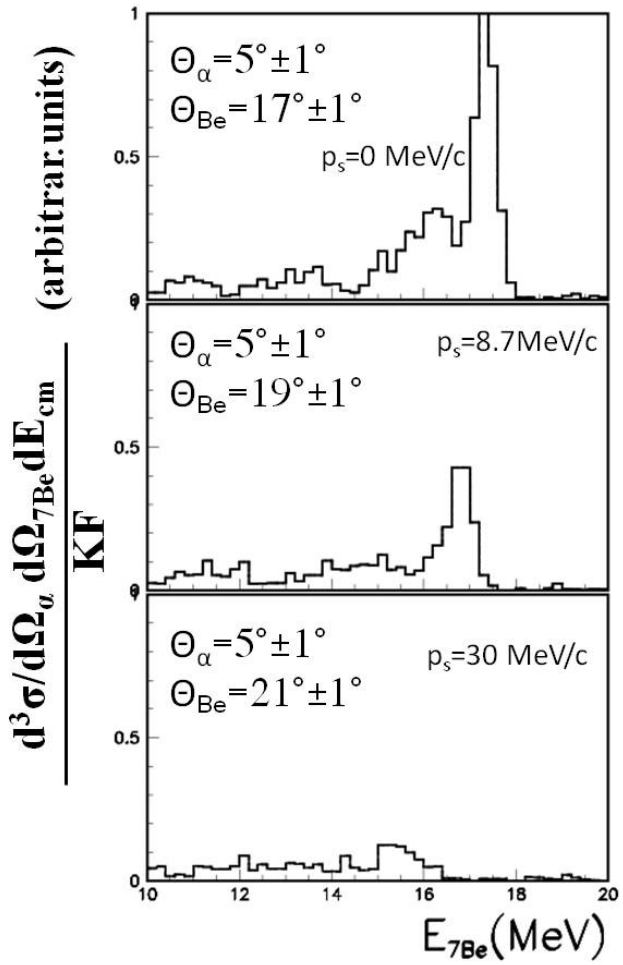

Figure 4.20: Typical coincidence spectra for the A-C coupled projected on the ^{7}Be axis for a fixed θ_{Be} and three different θ_{α}. The first condition corresponding to the minimum neutron momentum.

plot allows one to discriminate the sequential mechanism by introducing graphical selection which leave outside of the astrophysically relevant energy region those loci corresponding to sequential decays from the intermediate compound nucleus. In Figure 4.21 ("butterfly diagram") the relative energy $E_{\alpha-Be}$ is reported as a function of the neutron momentum p_n, for both detectors pairs. The horizontal lines correspond to the excited states of ^{11}C, as discussed in the previous section. In particular the kinematic loci extending to low p_n are connected to the decay from 8.701 MeV, 8.655 MeV (this two levels are unresolved also in this plot) and

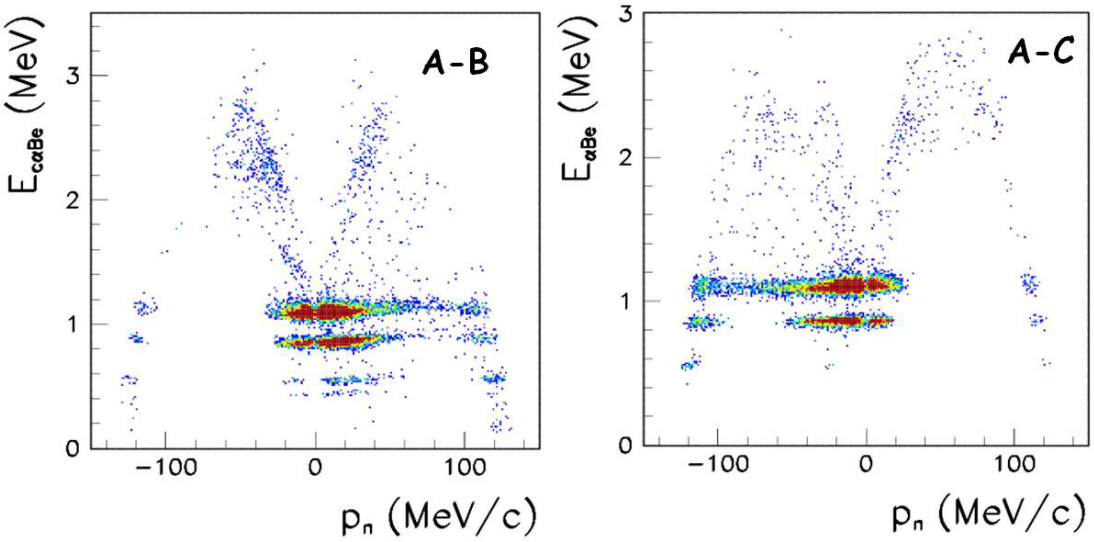

Figure 4.21: Typical experimental "butterfly diagram" for each pairs of detectors. The horizontal locus in the 2D matrix reveals the presence of the 8.701 MeV ^{11}C excited states just in the region where the bulk of the QF mechanism is expected.

8.401 MeV ^{11}C excited states, the first one constituting the most relevant for astrophysical applications. Moreover, as a second check to explore the behavior of the coincidence yield for the $^{11}C^{*} \rightarrow \alpha + ^{7}Be$ channel depending on the neutron momentum p_n, the $E_{^{10}B-p}$ relative energy spectra was reconstructed for all coincidence events.

$E_{^{10}B-p}$ relative energy corresponds to the $E_{c.m.}$ variable define by the energy conservation law: $E_{c.m.} = E_{\alpha-Be} - Q_{2-body}$, where Q_{2body} =1.145 MeV is the Q-value of the $^{10}B(p,\alpha)^{7}Be$ reaction [Spitaleri *et al.* (2004)]. Such spectra are obtained for different neutron momentum p_n and divided for the phase-space factor in order to remove the pure kinematics effects due to the actual phase-space selection. These spectra, reported in figure 4.22 were obtained by selecting the $0<p_n<20$ MeV/c (black line), $20<p_n<40$ MeV/c (red line) and $40<p_n<60$MeV/c (green line) intervals of the neutron momentum p_n. Such a picture clearly demonstrates that in the energy region around 10 keV, and in the lower energy region where is present the contribution of the subthreshold level of ^{11}C at 8.42 MeV, the coincidence yield is much higher for $0<p_n<20$ MeV/c than what is obtained at larger p_n momenta. Indeed, at higher momenta it drastically decreases and the

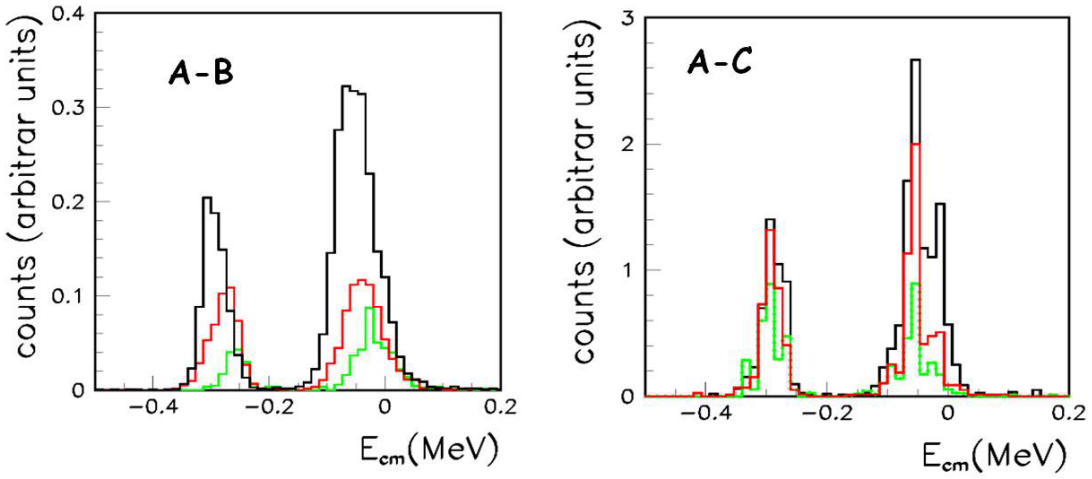

Figure 4.22: The coincidence's yield for a different range of the neutron momentum for the both coincidences A-B and A-C. The decreasing of the maximum of the peak moving from $0<p_n<20$ MeV/c (black line) to $20<p_n<40$ MeV/c (red line) and to $40<p_n<60$MeV/c (green line). This represent a first test of the occurrence of the QF mechanism in the ^{2}H(^{10}B,α^7B)n reaction.

resonances becomes barely visible compared to the background. Moreover, in such figure are also evident, in addition to the contribution of a subthreshold resonance at 8.402 MeV, two unresolved peaks corresponding at 8.701 MeV and at 8.655 MeV ^{11}C excited states, therefore the level of our interest (8.701 MeV) until now was not distinguishable from the other level. These experimental data provide a strong evidence that a clear correlation between coincidence yield and spectator momentum p_n exists. This is a necessary condition for the dominance of the QF reaction mechanism in the region approaching zero neutron momentum. A very similar result was obtained for the A-C coincidence couple as shown in the left panel in figure 4.22. Moreover, the number of events are shown as a function of neutron momentum.
The result shown in figure 4.23 is in agreement with the theoretical Hulthén wave function.

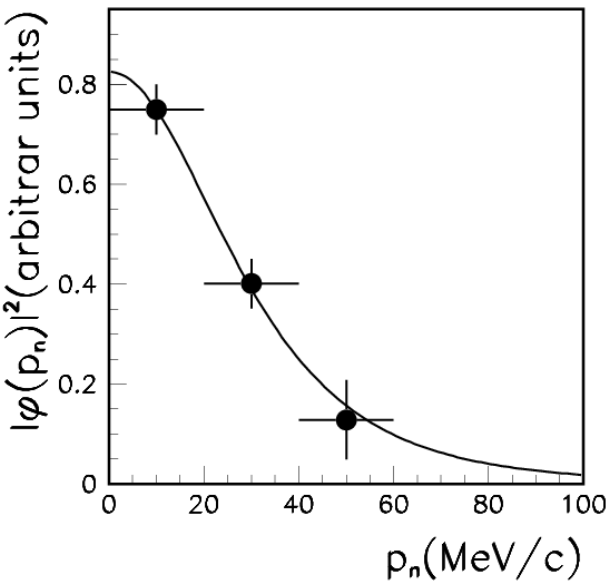

Figure 4.23: Data obtained as a function of neutron momentum.

4.5.1.4 Experimental Momentum Distribution for the p-n relative motion inside the deuteron

This discussion can be made more quantitative as the neutron momentum distribution inside the deuteron can be measured by means of the ^{2}H(^{10}B,α^7Be)n QF reaction. Indeed, only if the deuteron breakup process is direct, the neutron momentum distribution keeps the same shape as inside *d*. Thus the agreement between the shape of the deuteron momentum distribution and experimental one is a compelling evidence of the occurrence of the QF mechanism [Spitaleri *et al.* (1999), Spitaleri *et al.* (2004)].

To reconstruct the experimental p_n distribution, the energy-sharing method [Spitaleri *et al.* (2004), La Cognata *et al.* (2005)] is applied to each pair of coincidence detectors selecting a narrow $E_{\alpha-Be}$ relative energy window, ΔE=100 keV for both coincidence pairs. Dividing the resulting quasi-free coincidence yield by the kinematic factor, a quantity that is proportional to the product of the p_n momentum distribution and the differential two-body cross section is deduced:

$$|\varphi_a(p_n)|^2 \left(\frac{d\sigma}{d\Omega_{c.m.}}\right)^{HOES}_{E_0} \propto \frac{d^3\sigma}{d\Omega_\alpha d\Omega_{^7Be} dE_{c.m.}}[KF]^{-1} \tag{4.8}$$

where E_0 is the mean energy of the relative energy window. In the restricted chosen relative energy range, the differential binary cross section $(d\sigma/d\Omega_{c.m})^{HOES}$ of the ^{10}B+p reaction can be considered almost constant. Thus the experimental p_n momentum distribution is given in arbitrary units by the equation:

$$|\varphi_a(p_n)|^2 \propto \frac{d^3\sigma}{d\Omega_\alpha d\Omega_{^7Be} dE_{c.m.}}[KF]^{-1} \tag{4.9}$$

The momentum distribution from A-B and A-C coincidences were averaged out after being normalized to each other. This results is compared with the Hulthén wave function in momentum space [Zadro *et al.* (1989)] representing the shape of *n-p* momentum distribution in the plane-wave impulse approximation (PWIA):

$$\varphi_a(p_n) = \frac{1}{\pi}\sqrt{\frac{ab(a+b}{(a-b)^2}}\left[\frac{1}{a^2+p_n^2} - \frac{1}{b^2+p_n^2}\right] \tag{4.10}$$

with parameters a=0.2317 fm^{-1} and b=1.202 fm^{-1} for the deuteron [Zadro *et al.* (1989)]. The experimental momentum distribution for A-B and A-C coincidence detectors are reported in figure 4.24, where the superimposed theoretical distribution superimposed onto the data contains a single fitting parameter.

The normalization constant was fixed by the experimental maximum. Thus equation 4.10 with parameters *a* and *b* from Zadro *et al.* (1989) reproduce quite well the shape of the experimental data. The good agreement between the two, together with the previous tests, makes us confident that the QF mechanism gives the main contribution to the ^{10}B+d reaction in the selected kinematical experimental region; and it can be selected without significant contribution from

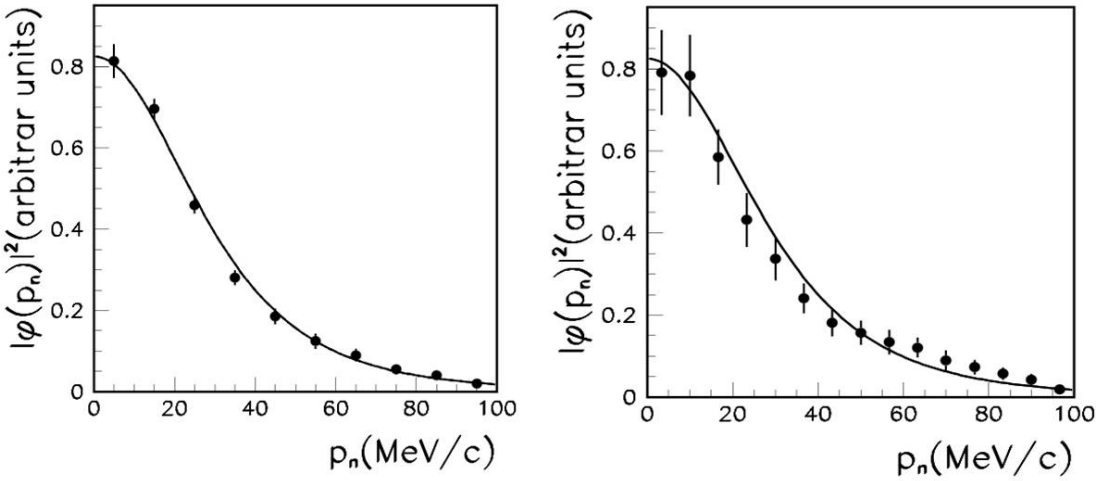

Figure 4.24: Average experimental momentum distribution (full dots) obtained from the A-C coincidence (left panel) and A-B coincidence (right panel), compared with the theoretical distribution (full line).

contaminant SD process. Moreover, this agreement means that the QF mechanism is present and dominant in the p_n<40 MeV/c neutron momentum range. For these reasons, in the following analysis only the phase-space region where the p_n<40 MeV/c is taken into account, allowing us to apply the PWIA in the following calculation.

4.5.2 Data analysis: Study of the 10 keV resonance

The channel of interest in the three-body reaction ^{2}H(^{10}B,α^7Be)n can be populated through the formation of various excited states of the compound nucleus ^{11}C*. The presence of the ^{11}C levels is evident in the relative energy plot reported in Figure 4.17 and 4.18 and it is more clear in Fig. 4.25 where the projection of the events on the $E_{\alpha-Be}$ axes is reported. In the Figure peaks at 8.422 MeV ($5/2^-$) and the unresolved two peak 8.655 MeV ($7/2^+$) and 8.701 MeV ($5/2^+$) are evident. In table 1 we reported the parameters for the resonances [Ajezenberg-Selove (1988)].

As explained above, the energy region of our interest, Gamow region around E_{cm}=10 keV, corresponds to the ^{11}C excited state at 8.701 MeV. In order to

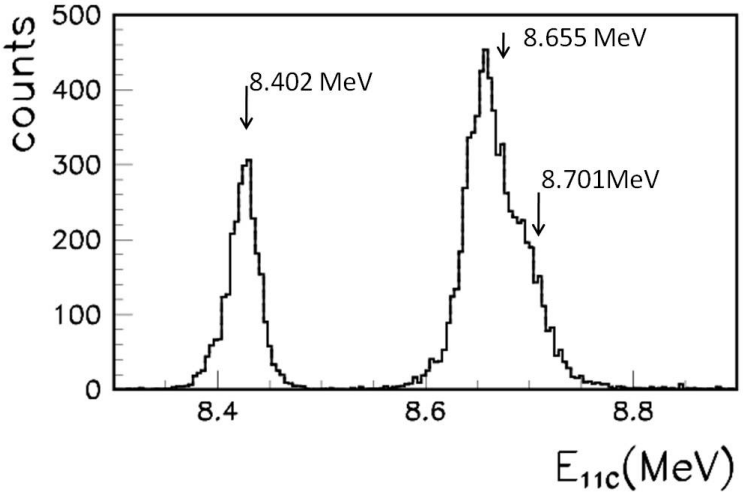

Figure 4.25: Spectrum of energy levels of ^{11}C, in the region of our interest. Is clear the level at 8.42 MeV while is evident the unresolved peak corresponding to the 8.655 MeV and 8.701 MeV ^{11}C excited states.

^{11}Clevels		
^{11}C levels	J^{π}	Γ_{TOT}(MeV)
8.402	$5/2^{-}$	-
8.655	$7/2^{+}$	$\leq$5keV
8.701	$5/2^{+}$	0.016$\pm$0.001

Table 4.2: Level of ^{11}C of our interest as reported in literature [Ajezenberg-Selove (1988)]

make the study of this resonance it was necessary to subtract the contribution due to the presence of the level at 8.655 MeV. Figure 4.26 shows the two levels contribution fitted by the sum of two Breit-Wigner centered at the resonance energies and with natural width corrected by our energy resolution, that for this pairs of detectors is δE=14 keV. Thus the contribution of the subthreshold resonance has been subtracted and the result is reported in figure 4.27. This result shows the level of our interest that has been considered for the subsequent extraction of the astrophysical factor. the error associated with this process is estimated to be about 5%.

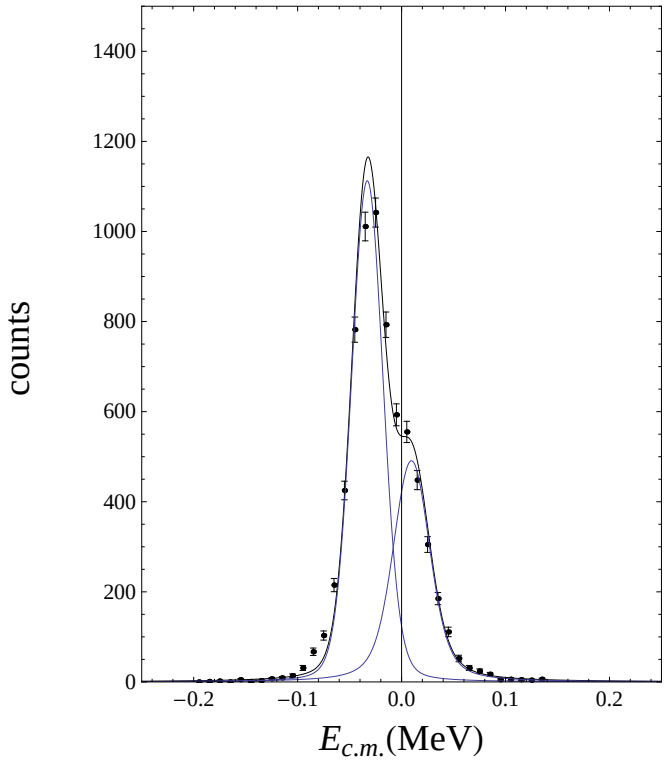

Figure 4.26: Energy spectrum for the events corresponding to the 8.655 MeV and 8.701 MeV ^{11}C excited states. The figure shows the Breit Wigner functions and their sum (see text), which reproduces the experimental data.

4.6 Extraction of the Astrophysical S(E)-factor

Once the contribution of the 10 keV resonance has been determined a Monte Carlo simulation was then performed to extract the KF $\cdot|\Phi_{ps}|^2$ product. The geometrical efficiency of the experimental setup as well as the detection threshold of PSD's were take into account. The energy resolution for the PSD A-C pair was evaluated about 14 keV while for the A-B pair is about 23 keV then the latter pair was not considered for the next phase of analysis, in fact, due to poor resolution the contributions of the subthreshold level could not be well separated. So, in order to extract the behavior of the astrophysical S(E)-factor, we have considered only the PSD's A-C pairs, having the lowest energy resolution.

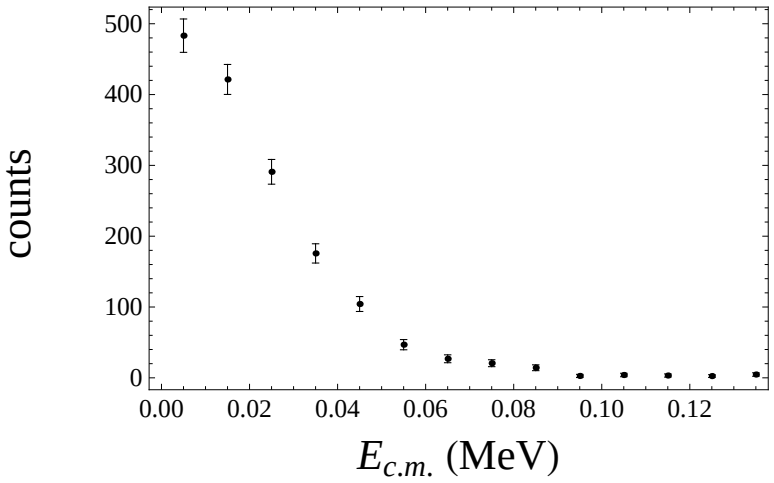

Figure 4.27: Result of subtracting the contribution due to the level at 8.655 MeV. Thus this spectrum represent the level of our interest at 8.701 MeV corresponding to E_{cm}=10 KeV the Gamow peak for this reaction.

Following the PWIA prescription the two-body cross section was derived dividing the selected three-body coincidence yield by the result of Monte Carlo simulation. As already mentioned, since the PWIA approach supplies the off-energy-shell two body cross section, it is necessary to perform the appropriate validity test on the indirect two-body cross section before extracting the low-energy cross section of astrophysical interest.

4.6.1 Validity test: Angular distribution

A first test involves the THM angular distribution. The emission angle for the alpha particle in the α-^{7}Be center of mass system, can be calculated according to the relation used in [Jain *et al.* (1970)]. This angle is relevant for the angular reconstruction

$$\theta_{c.m.} = \arccos \frac{(\overrightarrow{v}_p - \overrightarrow{v}_t) \cdot (\overrightarrow{v}_C - \overrightarrow{v}_\alpha)}{|\overrightarrow{v}_p - \overrightarrow{v}_t||\overrightarrow{v}_C - \overrightarrow{v}_\alpha|} \tag{4.11}$$

where the vectors $\overrightarrow{v}_p$, $\overrightarrow{v}_t$, $\overrightarrow{v}_C$ and $\overrightarrow{v}_\alpha$ are the velocity of the projectile, transferred proton and the outgoing ^{7}Be-α particles, respectively. These quantities are calculated from their corresponding momenta in the laboratory system, where

the momentum of the transferred particle is equal and opposite to that of neutron when the quasi-free assumption are fulfilled [Jain *et al.* (1970)]. The center of mass angular ranges covered in the present experiment were $\theta_{c.m.}$=40° - 110° e and $\theta_{c.m.}$=2°-60°; 120°-160° for the A-C and the A-B detector coincidences, respectively. The angular distribution test is performed only in the energy region correspond to $E_{c.m.}$=10 keV, after the subtraction of the contribution due to the subthreshold level.

To select the region where the QF contribution is dominant, coincidence events for neutron momentum ranging between -40<p_n<40 MeV/c are considered, according to the results obtained in the experimental study of the p-n relative motion momentum distribution. Because any angular distribution are present in literature for the energy region of our interest (less than 400 keV), our goal was to reproduce the flat behavior according to l=0 contribution of the 8.701 MeV ^{11}C level. The result are given in figure 4.28 where the error bars represent only the statistical errors.

4.6.2 Validity test: Excitation function

As a further validity test, the energy behavior of the indirect excitation function is examined to check whether the cross section integrated over the full $\theta_{c.m.}$ range is consistent with direct data as reported in literature [Angulo *et al.* (1993)].

By using the PWIA it is possible to extract the nuclear part of the 2-body cross section for the ^{10}B(p,α)^{7}Be reaction following the relation already mentioned in previous chapter:

$$\left(\frac{d\sigma}{d\Omega}\right)^{N}_{^{10}B-p} \propto \frac{d^{3}\sigma}{dE_{\alpha}d\Omega_{\alpha}d\Omega_{Be}}[(KF)|(\Phi(\overrightarrow{p_s})|^2]^{-1} \tag{4.12}$$

where 'N' in the apex reminds that the THM allows to extract the nuclear part of the cross-section, therefore without Coulomb effects including the electron screening one. For the kinematical region in which the QF contribution is dominant ($|p_n|$ <40 MeV/c) and for the events selected as previously explained, the ratio between the measured three-body coincidence yield and the quantity (KF) $|\Phi(\overrightarrow{p}_n)|^{2-1}$ term has been evaluated.

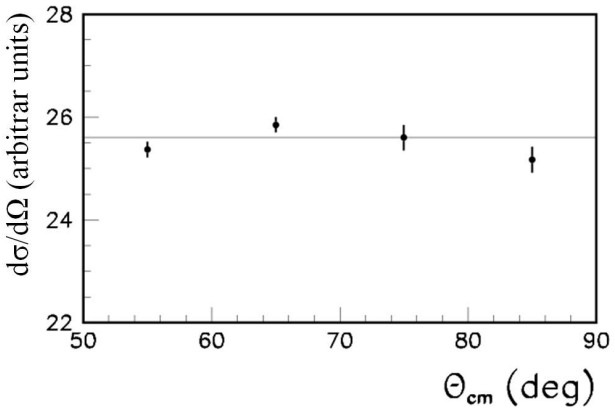

Figure 4.28: Extract angular distribution for the indirect measurement of the^{10}B(p,α)^{7}Be reaction. The evident of a flat distribution is a test of l=0 for the level of our interest.

According to equation 4.12 such ratio represents the 2-body cross section in arbitrary units expressed in terms of $E_{c.m.}$ variable (Fig. 4.29). In addition, to compare two data sets and to extract the normalization factor, needed to express the indirect data in absolute units, THM cross section is multiplied by the Coulomb penetration factor, supposing a dominant l=0 partial wave in the entrance channel of the ^{10}B+p two body reaction and a channel radius given by the sum of the radii of the two interacting nuclei. The penetrability factor is determined by the equation:

$$P_l(k_{10B-p}R) = \frac{1}{F_l^2(k_{10B-p}R) + G_l^2(k_{10B-p}R)} \tag{4.13}$$

where F_l and G_l are the regular and irregular Coulomb wave function, k_{10B-p} and R the ^{10}B-p relative wave number and interaction radius respectively [Spitaleri *et al.* (2001)]. Finally normalization to the direct behavior was performed in the energy region between $E_{c.m.}$=30 keV and 100 keV. The final binary cross section extracted from A-C coincidence events is shown in Figure 4.30 (red dots) where direct data are also given as black dots. The good agreement between the data sets is a test of validity for the method and it is a necessary condition for the further extraction of the astrophysical S(E) [Spitaleri *et al.* (2004), Spitaleri *et al.* (2001), Tumino *et al.* (2003), La Cognata *et al.* (2005)].

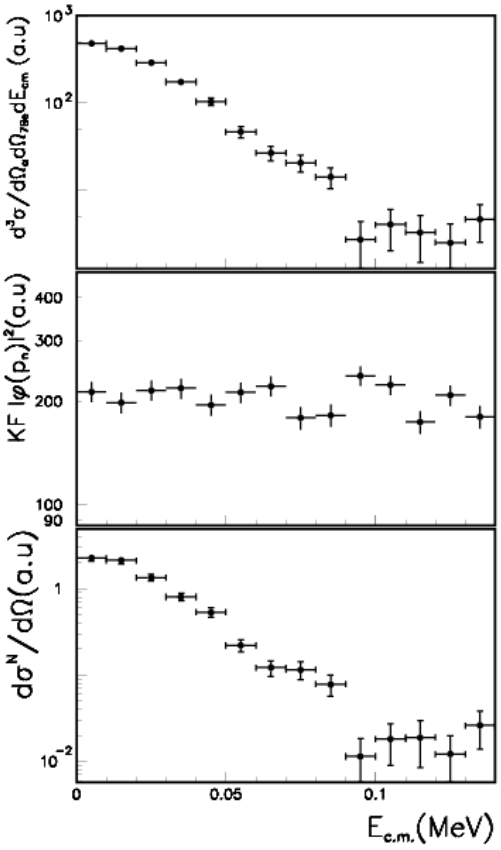

Figure 4.29: From the 3-body coincidence yield to the nuclear part of the 2-body cross section. Upper panel: the experimental 3-boby coincidences in the momentum range $|p_n|$<40 MeV/c. Middle panel: simulation of the KF $|\Phi\ p_n|^2$ term. Lower panel: the extracted nuclear part of the 2-body cross section, is evident the resonance that correspond to $E_{c.m.}$=10keV.

4.7 Results and Discussion

This reaction, as already explained, proceeds mainly through the formation of the 8.701 MeV ^{11}C ($J^{\pi}=5/2^{+}$ and $\Gamma=16\pm2$ [Wiescher *et al.* (1983)]) excited state. The direct and indirect data are not directly comparable due to their different energy resolution: 5 keV in direct data and 30 keV in THM data. In order to overcome this problem, a "smearing out" of the direct data was performed.

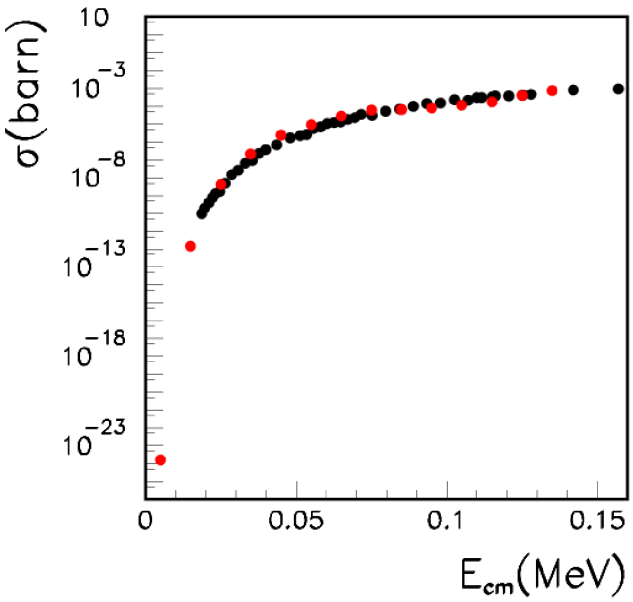

Figure 4.30: Comparison between the TH indirect excitation function (red dots) for the ^{10}B(p,α)^{7}Be reaction and the direct data (black dots)[Angulo *et al.* (1993)].

Then, to make this worsening process of direct data, the experimental fit on direct data as reported in [Angulo *et al.* (1993)] was reproduced taking into account the different energy resolution. The equation of the fitted S(E)-factor, was reported in Youn *et al.* (1991) and used by Angulo *et al.* (1993), consists into a single-level Breit-Wigner with:

$$S(E) = S_r(E_r)\frac{exp(2\pi\eta(E))}{exp(2\pi\eta(E_r))}\frac{\Gamma_p(E)}{\Gamma_p(E_r)}\frac{\Gamma_\alpha(E)}{\Gamma_\alpha(E_r)}\frac{[\frac{1}{2}\Gamma(E_r)]^2}{(E-E_r)^2+[\frac{1}{2}\Gamma(E)]^2} \qquad (4.14)$$

where the energy dependence of Γ_p(E) and Γ_α(E) were obtained by means of ^{10}B(p,γ)^{11}C reaction studied in [Wiescher *et al.* (1983)] and can be expressed as:

$$\frac{\Gamma_p(E)}{\Gamma_p(E_r)} \cong \exp[-W_0(E)]/\exp[-W_0(E_r)], \qquad (4.15)$$

$$\frac{\Gamma_\alpha(E)}{\Gamma_\alpha(E_r)} \cong \exp[-W_1(E_\alpha)]/\exp[-W_1(E_{\alpha r})], \qquad (4.16)$$

where W_0 and W_1 is *s*-wave and *p*-wave penetration factor respectively, E$_\alpha$ is center of mass energy in MeV of α+^{7}Be system and the energy dependence of the

total width of Γ(E) was assumed to be that of Γ_α taking $\Gamma(E_r)$= 0.016 MeV [Youn *et al.* (1991)]. For each value of this experimental fit, a "dispersion" function on the variable $E_{c.m.}$ was made up fixing its σ-value according to our energy resolution. By assuming that for each energy the integral of the number of the direct and indirect data was the same, the net contribution of a worsening of the energy resolution of the direct data is reflected in a smearing of the value of the astrophysical S(E)-factor, especially in the resonant region. The result of this smearing is shown in Figure 4.31 (line I) and is compared with the behavior of the direct fit before having worsened the resolution (line II).

Once that the smearing out of direct data was performed, it is possible to perform a consistent comparison between THM S(E)-factor and direct one. The THM astrophysical S(E)-factor, was extracted following the usual definition [Spitaleri *et al.* (1999), Spitaleri *et al.* (2004)] and using the procedure describe in the chapter 3. Once that the nuclear part of the two body cross-section was extracted, the S(E)-factor was obtained by:

$$S(E) = E \sum_l W_l P_l \sigma^N(E) \exp(2\pi\eta) \tag{4.17}$$

being P_l penetrability factor expressed again in terms of regular and irregular Coulomb function. Thus, the TH data have been fitted to the smearing direct one represented by line II in figure 4.31.

The result is shown in Figure 4.32 in which is evident that the TH data (black points) is in good agreement with the direct data smeared out at the same energy resolution, remembering that the direct data are present only in the center of mass energy region above 20 keV while in the lower energy region is present only the extrapolation. Using the fit of direct data after smearing out to our energy resolution, we are able to fit the THM data leaving as the only free parameter the normalization factor so that we obtained the value for S(10 keV)=1379 $\pm$ 207. This value was compared with the S(10 keV) obtained in the first experiment with the THM as showed in table 4.2. The error on the THM S(E)- factor has been determined taking into account the errors of the subtraction procedure, the statistic errors and the error related to the normalization procedure.

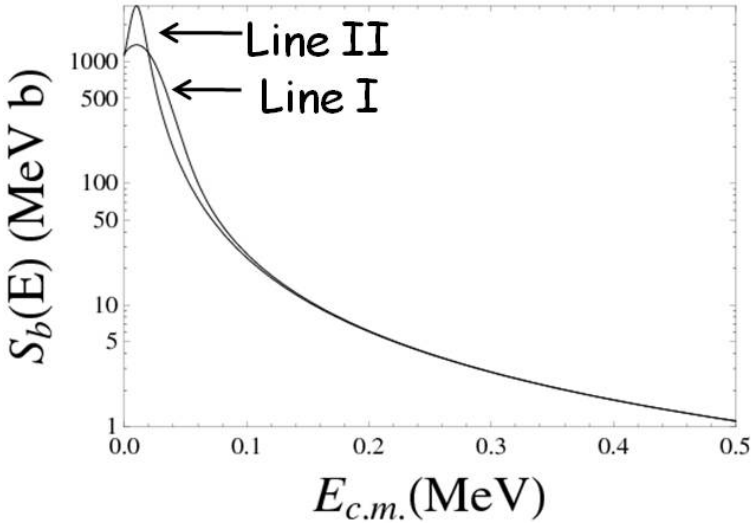

Figure 4.31: Smearing out of the fit on the direct data [Angulo *et al.* (1993)](line I) at our energy resolution 30 keV compared with the fit of direct data without worsening (line II).

Thus, we are able to reproduce the behavior of the direct data making a first measurement below 20 keV where is present only the extrapolation. We can conclude that this approach to the study of the present reaction confirms the power of the THM to reach the ultra-low energy value. This is an important feature of the method, since its application allows to study the resonant contribution even in the energy region, usually reached through the extrapolation, where both Coulomb penetration and electron screening effects are dominant.

Experiment	S(10) (MeV b)	S(0)(MeV b)
THM first experiment	577 ± 173.	562± 168
THM present experiment	1379± 207	1166.93± 175.04

Table 4.3: angles and distance covered by the detectors and distance from target.

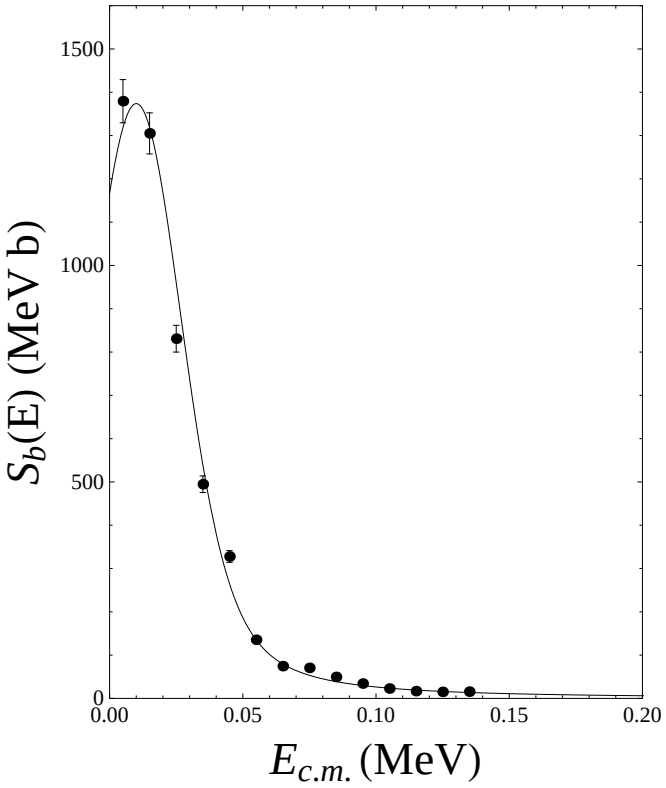

Figure 4.32: Trojan Horse astrophysical S(E)-factor (full dots) compared with direct energy behavior (line).

Finally, the comparison between THM data (bare nucleus) and direct data (screened data) allows for the evaluation of the electron screening potential U_e (see chapter 3). The relationship between the screened and bare nucleus astrophysical S(E) factor is the following

$$S_s(E) = S_b(E) \exp(\frac{\pi \eta U_e}{E}) \tag{4.18}$$

where the exponential term represents the enhancement factor due to the electron screening effect, which depends on the U_e potential. Since the electron screening effect depends only from the changes of the interacting particles, we have adopted the $U_e = 502 \pm 140$ eV value evaluated from the ^{11}B(p,α) reaction study performed via the THM (see chapter 5). The result is reported in figure 4.24 and it is compared with the one obtained by [Angulo *et al.* (1993)] with $U_e = 430 \pm 80$ eV. From the analysis of the figure it is evident that the two electron screening

potentials are quite consistent, within the experimental error. Thus, taking into account the two results we can assume U_e=448 ±69 eV as best estimation of the electron screening potential in the ^{10}B + p interaction.

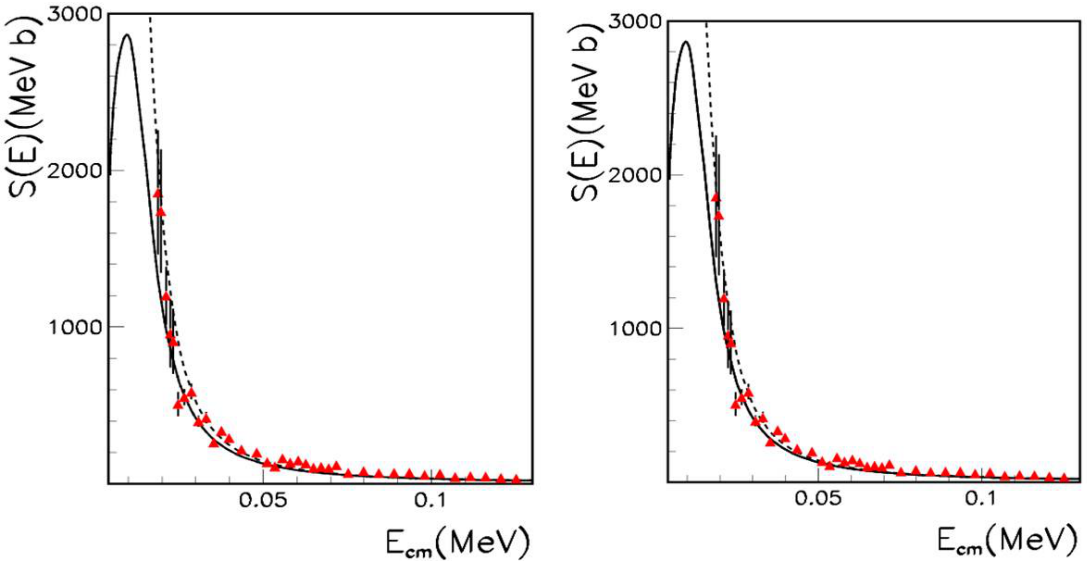

Figure 4.33: Extrapolation of Astrophysical S(E)-factor reported in [Angulo *et al.* (1993)] in comparison with their data (red points). Dashed curve includes the effects of electron screening. Left panel using the value U_e=500±140 obtained using equation 4.18 and right panel U_e=430±80 value obtained by [Angulo *et al.* (1993)].

Chapter 5

Study of ^{11}B(p,α)^{8}Be reaction through the THM

The investigation of proton induced reactions on boron isotopes represents one of the most interesting application field concerning the "burning problem" for lights element. In particular, the study of (p,α) reaction induced on both the boron-isotopes ^{11}B and ^{10}B finds application in the astrophysical scenario of light element depletion. For this reason we performed different experiments also for ^{11}B(p,α)^{8}Be, in order to evaluate the cross section in the energy region relevant for astrophysics and to complete the results coming from the available direct data. The indirect measurements for the ^{11}B(p,α)^{8}Be through the THM allows one to extend the available direct information about the behavior of the astrophysical S(E)-factor even in the energy region where both Coulomb barrier and electron screening effects are dominant. The ^{11}B(p,α)^{8}Be is mainly induced for temperature T$\geq 5\cdot10^{6}$K, giving a value for the energy of the Gamow peak of about 10 keV while the Coulomb barrier is of about 1.7 MeV. The experiment was performed at Laboratori Nazionali del Sud in Catania applying the THM to the three-body ^{2}H(^{11}B,α^{8}Be)n reaction induced at about 27 MeV. The experiment was devoted to study the α_0 and α_1 channel for this reaction, that refers at α-particles coming from ^{8}Be in its ground state (α_0) and from its first excited state (α_1).

5.1 Status of the art

Several direct measurements were performed in order to study the ^{11}B(p,α)^{8}Be reaction. In these study the astrophysical S(E)-factor shows up a resonant state at about 600 keV in the ^{11}B-p center of mass system corresponding to the 16.57 MeV ($J^{\pi}=2^{-}$) level of ^{12}C and a further low-energy level at about 150 keV corresponding to the 16.106 MeV ($J^{\pi}=2^{+}$) level of ^{12}C. In particular in the case of ^{11}B(p,α_0)^{8}Be reaction (Q=8.59 MeV) the S(E)-factor shows the presence of the l=1 $\sim$150 keV level superimposed on a non resonant l=0 reaction yield while the $\sim$600keV cannot contribute to the α_0 due to its J^{π} assignment.

For the ^{11}B(p,α_1)^{8}Be reaction (Q=5.56 MeV) both level contribute to the α_1 reaction yield. The direct measurement for the ^{11}B(p,α)^{8}Be are reported in literature by [Angulo *et al.* (1993)] and [Becker *et al.* (1987)], in particular in the second paper the authors report the investigation for both α_0 and α_1 channels, (i.e. the contribution to the total cross section coming from the ground state of ^{8}Be and its first excited state). In order to investigate the contribution of the resonant level at about 150 keV an evaluation of the excitation function with both solid and gas target was performed. In such work there is not an evaluation for the electron screening effects and the extrapolated astrophysical S(E)-factor values are: S(0)= 2.1 MeV b for the α_0 channel and S(0)=195 MeV b for the α_1 channel [Becker *et al.* (1987)]. In figure 5.1 the results for the α_0 channel only are showed.

A further investigation was performed by [Angulo *et al.* (1993)], with the investigation starting from $E_{c.m.}$=132 keV down to $E_{c.m.}$=18.73 keV that confirmed the presence of the resonant contribution and extracted the experimental value of the electron screening potential. In this work the astrophysical S(E)-factor is reported for both α_0 and α_1 channels. From such measurement they extracted the experimental value for the electron screening potential U_e=430$\pm$80 eV that appear to be higher than the upper limit predicted from the adiabatic model, U_e^{ad}=340eV [Angulo *et al.* (1993)], confirming the systematic discrepancy between experimental and theoretical value for the electron screening potential

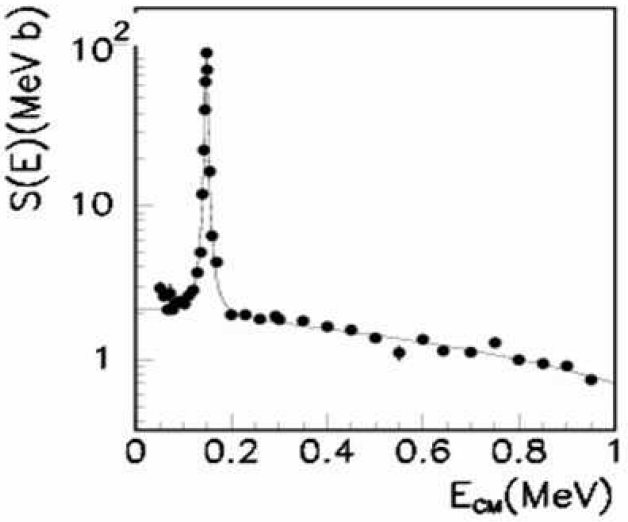

Figure 5.1: Astrophysical S(E)-factor for the ^{11}B(p,α_0)^{7}Be reaction reported in [Becker *et al.* (1987)].

values [Assenbaum (1987), Strieder *et al.* (2001)]. These direct measurements are included in NACRE compilation for nuclear astrophysics (figure 5.2).

The direct measurements studied the reaction in a wide range of energies but the present value of the astrophysical factor at zero energy S(0) and the value of the electron screening potential comes from the extrapolation of high-energies direct data. The THM allows one to extend the available direct information about the behavior of the astrophysical S(E)-factor even in the energy region relevant for astrophysics where is present the extrapolation. This reaction has been already studied via the THM [Spitaleri *et al.* (2004)]. In this first work the astrophysical S(E)-factor was extracted selecting the QF contribution on the ^{2}H(^{11}B(p,α^{8}Be)n reaction. Figure 5.3 shows the extracted S(E)-astrophysical factor, for which the value S(0)=0.41$\pm$0.09 MeV b was smaller than the direct one [Becker *et al.* (1987)]. Due to this discrepancy and in order to have a better resolution, a new experiment was performed devoted to a new extraction of the S(E)-astrophysical factor for the ^{11}B(p,α)^{8}Be reaction.

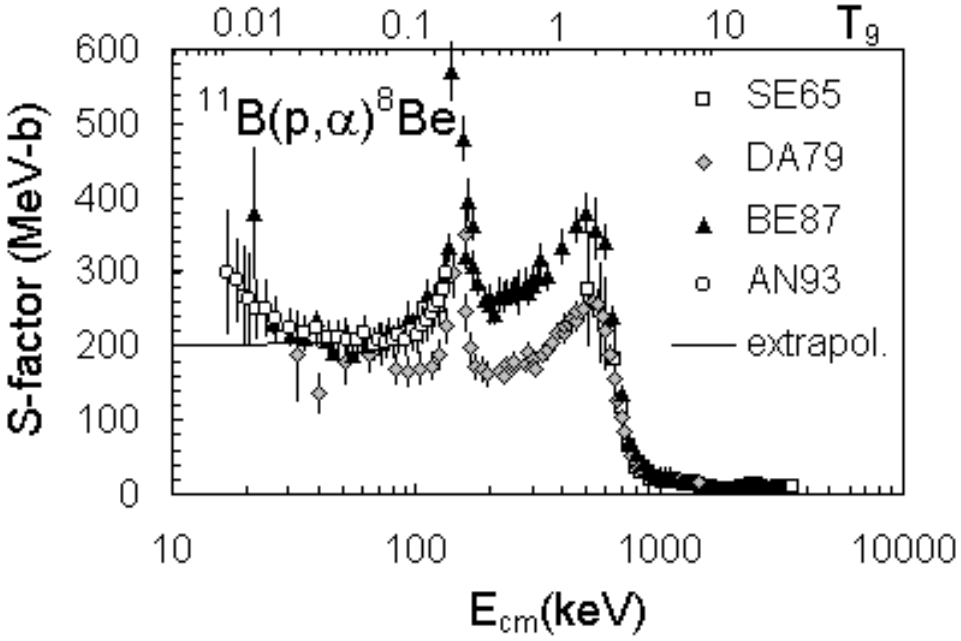

Figure 5.2: Behavior of the astrophysical S(E)-factor as deduced from direct measurements reported in NACRE compilation. A strong resonance at energies of about 150 keV is evident; besides this is a collection of different measurement where the sum of both α_0 and α_1 data are reported.

5.2 Experimental approach

The study of the ^{11}B(p,α)^{8}Be two body reaction was performed through the THM by selecting the QF contribution of the three-body ^{2}H(^{11}B,α^8Be)n reaction (Q_{3body}=6.36 MeV). The pseudo-Feyman diagram for this reaction is reported in figure 5.4, where in the upper pole is present the virtual two body reaction and in the lower pole the deuteron break-up. Also in this reaction (like in the ^{10}B(p,α)^{7}Be) the deuteron is used as the TH nucleus having a low binding energy for the *p*-*n* system (B_{p-n}=2.2 MeV) and the momentum distribution for inter-cluster motion known from independent experiments [Zadro *et al.* (1989)]. Since, the motion occurs mainly in *s*-wave the maximum for the neutron momentum is around at p_n=0 MeV/c.

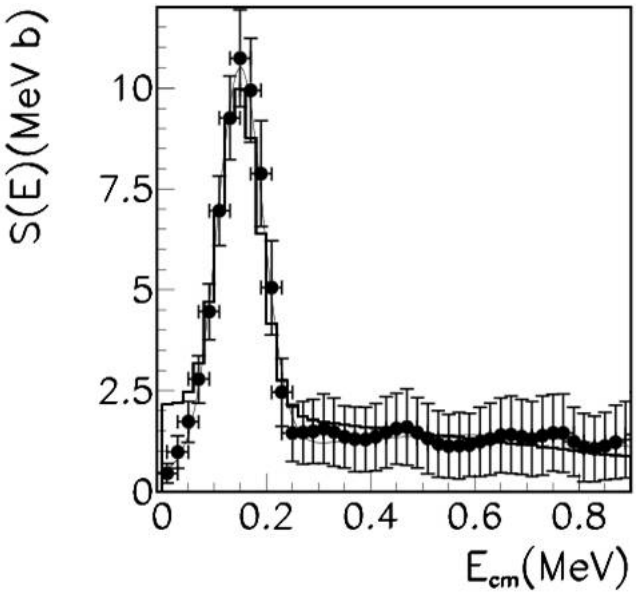

Figure 5.3: Astrophysical S(E)-factor as deduced from previous measurements of the ^{11}B(p,α)^{8}Be reaction through the THM. Is evident the peak in correspondence to the resonance at 150 keV with a FWHM of 140 keV due to the experimental resolution.

As was done for the previous reaction (see chapter 4), we choose the energy for the induced (p,α) reaction in order to reach the Gamow energy region, so the beam energy for the ^{11}B was calculated using this formula:

$$\Delta E_{QF} = E_{ax} - B_{xs} \pm E_{xs} \tag{5.1}$$

where E_{ax} is the value of the beam energy in the center of mass for the two-body reaction, B_{xs} is the binding energy of the deuteron and E_{xs} is the energy associated to the p-n intercluster motion inside the deuteron. Using this equation and selecting ΔE_{QF}=200 keV the beam energy requested for our study is 27 MeV. Moreover, a Monte Carlo simulation was carried out in order to explore the energetic and angular condition in which the three-body reaction occurs, and to identify the kinematical condition in which the QF contribution is dominant.

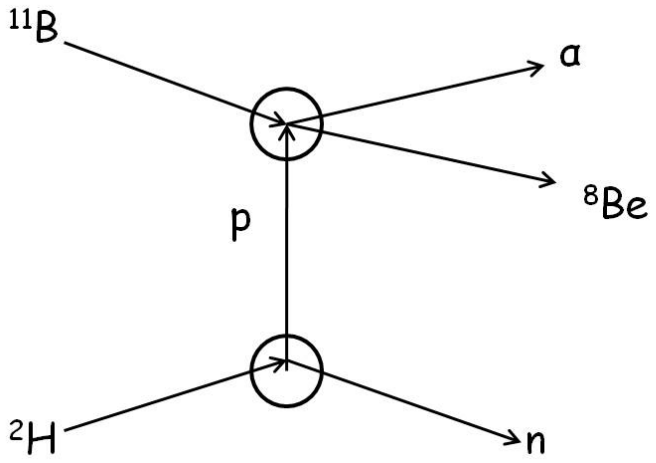

Figure 5.4: Pseudo-Feynman diagram for the QF process ^{2}H(^{11}B,α^{8}Be)n. In the upper pole is evident the virtual two body reaction while in the lower pole is present the deuteron break-up using as the TH nucleus.

5.2.1 The experiment

The experiment was performed at the Laboratori Nazionali del Sud in Catania with the aim of studying the ^{11}B(p,α)^{8}Be in the two channel ^{11}B(p,α_0)^{8}Be and ^{11}B(p,α_1)^{8}Be because both channels contributing to the total cross section as reported in the literature [Becker *et al.* (1987)]. In particular, while the α_0 channel implies the study of the α particles leading the beryllium in its ground state ($E_{g.s}$=92 keV) and α_1 channel implies the study of the α particles leading the beryllium in its first excited state (E*=3 MeV).

The SMP Tandem Van de Graaf accelerator provided a 27 MeV ^{11}B beam with a spot size on target of about 1.5 mm and intensities ranging between $2enA$ and $4enA$. Deuterated polyethylene target (CD_2) was placed at 90° with respect to the beam direction. The detection setup displaced inside the CAMERA 2000 scattering chamber, consisted of four Dual Position Sensitive Detectors (DPSD) made on two $50\times10mm^2$ silicon detectors mounted one above-the other and separated by an empty $1mm$ space. Such arrangement has been chosen in order to cover a large area where events coming from ^{8}Be are expected. Two standard Position Sensitive detector (PSD) were also used in order to detect the alpha-particles coming from the α_0 channel.

All the DPSD detectors were placed at about 200 *mm* from the target and placed symmetrically with respect the beam direction. The covered laboratory angles by the detectors are: θ_{DPSD1}=47°±7°, θ_{PSD2}=32°±5° and θ_{DPSD3}=17°±7° while the detectors DPSD6,PSD5 and DPSD4 were placed in the same angles respectively but in the other side with respect the beam direction. The pattern of the detectors is shown in table 5.1.
A schematic view of used detection setup is shown in figure 5.5 while in figure 5.6 is shown a photo. The adopted displacement allows to investigate a region where a dominant contribution of the QF mechanism is expected. This assures that the bulk of the QF contributions for the break-up process of interest falls inside the investigated regions. The α-particles coming from the decay of ^{8}Be were detected in coincidence in the DPSDs. The trigger for the event acquisition was the logic OR of the signals of involved detectors, in order to reconstruct, the two α_0 and α_1 channels separately in the off-line analysis. Energy and position signals for the detected particle were processed by standard electronics and sent to the acquisition system.

Detector	Central Angle (deg)	Angular coverage (deg)	Distance from target (cm)
DPSD1	+47	40.4-53.6	21.7
PSD2	+32	27.8-36.2	34
DPSD3	+17	10.2-23.8	21
DPSD4	-17	10.4-23,6	21.5
PSD5	-32	28-36	35.6
DPSD6	-47	40.8-53.2	22.8

Table 5.1: angles and distance covered by the detectors and distance from target.

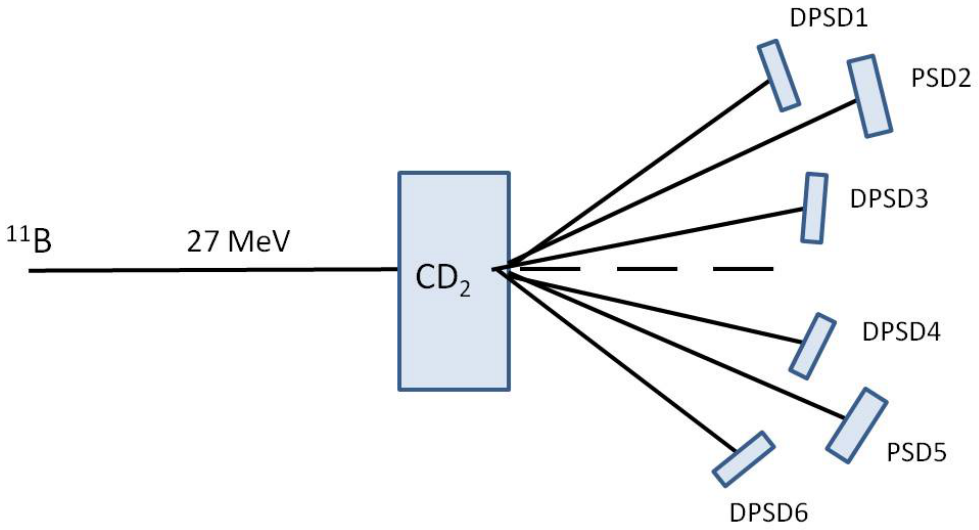

Figure 5.5: Schematic draw of experimental setup.

Figure 5.6: Photo of the experimental setup inside the CAMERA 2000, used for the study of ^{11}B(p,α)^{8}Be reaction.

5.3 Data analysis

5.3.1 Detector's calibration

The first step of the experiment was the calibration of the involved detectors. The calibration procedure is the same as was described in Chapter 4. All the detectors were calibrated in position using a grid with equally spaced slits, the slits positions were measured using a theodolite and the correspondence position-angle was established. Both position and energy calibration were performed delivering the 9 MeV ^{6}Li beam impinging on gold, carbon and deuterated polyethylene targets in order to use the kinematics of the elastic scattering ^{6}Li+^{197}Au and ^{6}Li+^{12}C and of the ^{6}Li+^{12}C$\rightarrow\alpha+^{14}$N reaction. Moreover a standard 3-peak alpha source was used in the low-energy region. The energy and position resolution were about 1% for each silicon detectors.

5.3.2 Identification of ^{8}Be events

The first stage in the data analysis, after the calibration, is the discrimination of the reaction channel of interest. Due to the presence of the unstable ^{8}Be isotope, it was necessary to reconstruct the "^{8}Be event" from a measurement of two α-particles in coincidence. The ^{8}Be decays as ^{8}Be$\rightarrow\alpha+\alpha$ with the half life of only τ=10^{-18}sec. Its ground state has $E_{g.s.}$=92 keV and its first excited state is at about E^{*}=3 MeV. Applying the energy and momentum conservation laws it is possible to reconstruct the relative energy of the two α-particles by means of the standard formula:

$$E_{rel} = \frac{1}{2}\mu v_{rel}^{2} \tag{5.2}$$

where μ is the reduced mass of the two particles and v_{rel}^{2} their relative velocity defined as:

$$\overrightarrow{v_{rel}} = \overrightarrow{v_1} - \overrightarrow{v_2} \tag{5.3}$$

from (5.2) and (5.3) we obtain

$$E_{rel} = \frac{1}{2}\mu(V_1^{2} + V_2^{2} - 2V_1V_2\cos\theta_{12}) \tag{5.4}$$

where $\cos\theta_{12}$ represents the relative angle between the two particles. In terms of the alpha-particles energies eq. 5.4 becomes:

$$E_{rel} = 0.5(E_{\alpha 1} + E_{\alpha 2} - \sqrt{E_{\alpha 1} E_{\alpha 2}} \cos\theta_{\alpha 1 \alpha 2}) \tag{5.5}$$

The analysis of the relative energy spectra allows for the identification of both $^8\mathrm{Be}_{gs}$ and ^8Be first excited state. Therefore, by measuring a energy and position of each particle, it was possible to extract its correspondence velocity and the reconstructed E_{rel} spectrum is shown in figure 5.7. where in the right panel is shown the prominent peak at about 92 keV that strongly reflect the presence of events $\alpha + \alpha \leftarrow ^8\mathrm{Be}$ whereas in the left panel is evident the peak at about 3 MeV in agreement with the relative energy of α-particles coming from ^{8}Be in its first excited state. As can be seen, for the α_1 channel the peak is broader than the α_0 one, this is probably due to the low resolution and background noise.

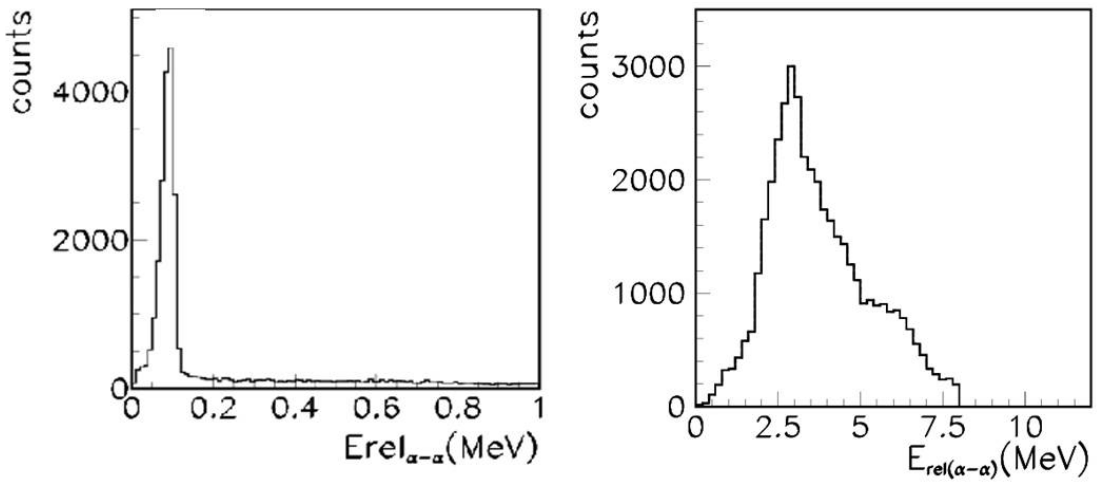

Figure 5.7: Relative energy spectrum for the two coincidence particle detected in the DPSD4. The peak at about 92 keV corresponds to the detection of two alpha-particles coming from the decay of $^8\mathrm{Be}_{g.s.}$ (right panel). In the left panel is shown the relative energy spectrum for the α-particles detected in coincidence in one part of DPSD4 and on PSD2. In this case is evident a peak at about 3 MeV that corresponds to the alpha particles coming from ^{8}Be in its first excited state.

5.3.3 Selection of the three-body reaction

After the identification of ^{8}Be and the assumption of mass number 4 for the third particle detected in the same coincidence event, the locus of events in the E_{α} vs. $E_{^{8}Be}$ plot for the ^{2}H(^{11}B,α ^{8}Be)n reaction was compared with the corresponding three-body kinematic calculation, appearing to be very well reconstructed. Figure 5.8 shows the locus of event for the α_0 channel in the right panel and for α_1 channel in the left one.

At this point, using momentum and energy conservations rules, it should be possible to reconstruct the Q-value of the three-body reaction. Since the selection of the three-body channel is fundamental for the progress of the data analysis, it is important to constrain the selection of the events as much as possible. The experimental spectrum of the Q_{3body} for both channels of reaction is shown in figure 5.9. The right panel shows a peak at about 6.35 MeV in agreement with the theoretical one (Q_{the}=6.36 MeV) for the α_0 channel the left panel shows a peak at around 3.3 MeV also in this case in agreement whereas the theoretical value 3.33 MeV for the α_1 channel.
This agreement is a signature of the goodness of our calibrations and for the precise selection of reaction channel. Only the events belonging inside the peak will be taken into account for the further analysis.

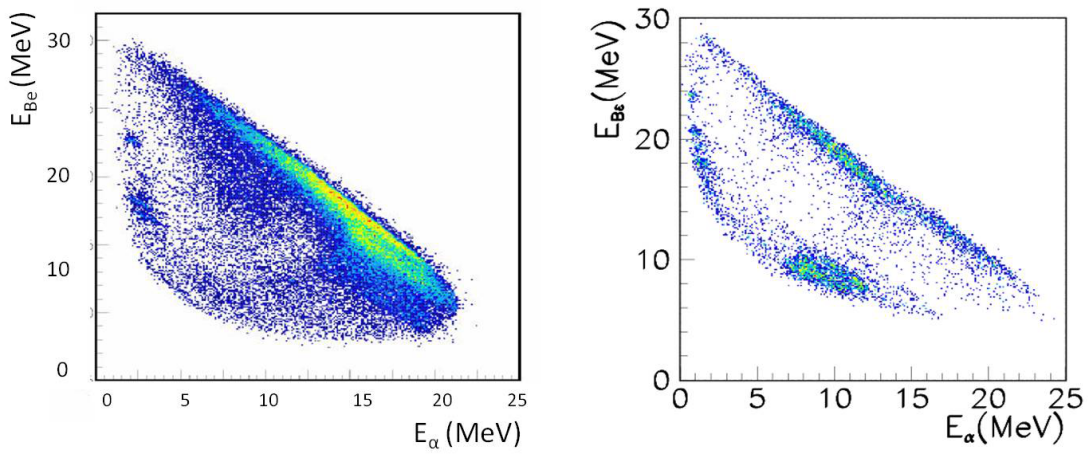

Figure 5.8: Experimental kinematical locus of event for the ^{2}H(^{11}B,α_0 ^{8}Be)n reaction(right panel)and for ^{2}H(^{11}B,α_1 ^{8}Be)n reaction in the left one.

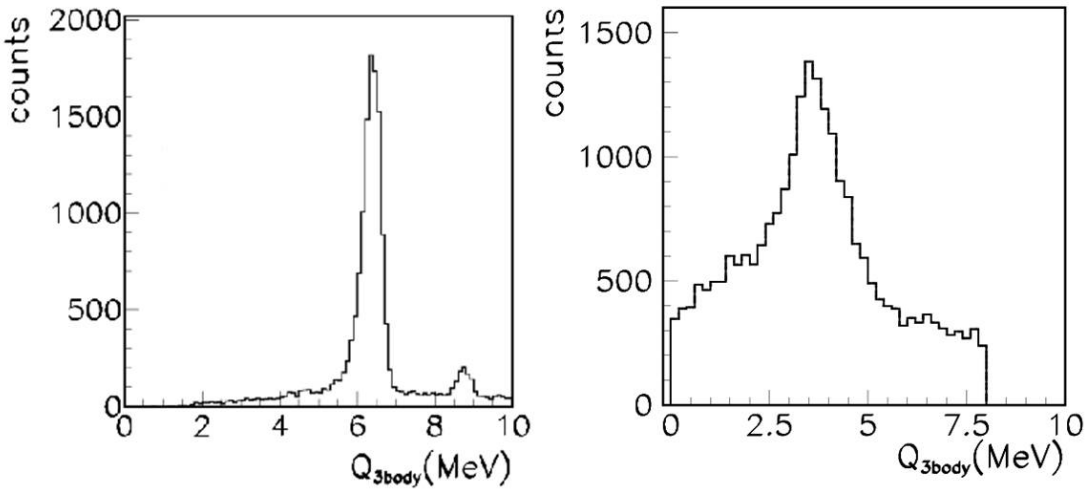

Figure 5.9: Experimental Q-value for the ^{2}H(^{11}B,α ^{8}Be)n reaction. A peak at 6.3 MeV is evident in the right panel in agreement with the theoretical value 6.36MeV for the ^{2}H(^{11}B,α_0 ^{8}Be)n reaction. In the left panel is evident a peak at 3.3 MeV in also agreement with the theoretical value 3.33MeV for ^{2}H(^{11}B,α_1 ^{8}Be)n reaction.

5.4 Selection of the Quasi-Free reaction mechanism

Once the reaction channel ^{2}H(^{11}B,α ^{8}Be)n is selected, the occurrence of the QF mechanism producing the outgoing particles: α,^{8}Be and neutron has to be investigated and its contribution to the total three-body cross section has to be disentangled from the ones of other reaction mechanisms (or instance Sequential Decay).

Next step in the data analysis is to identify if the SD contributions due to the two-step processes (sketched in figure 5.10) is present and establish whether the ^{12}C excited states are fed through a QF or SD process.

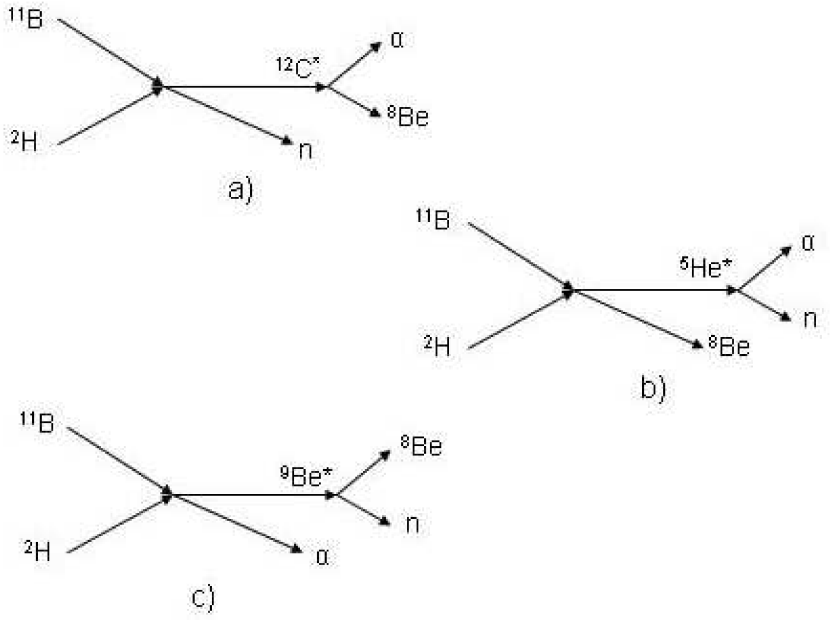

Figure 5.10: Possible sequential decays feeding the same three particles in the exit channel. a) ^{12}C intermediate states, b) ^{5}He intermediate state, c) ^{9}Be intermediate state.

5.4.1 Study of relative energy two dimensional plot

In order to study the SD processes which take place through the formation of the ^{9}Be and ^{5}He compound nuclei, the relative energies two dimensional spectra $E_{\alpha-n}$ vs. $E_{\alpha-Be}$ and E_{Be-n} vs. $E_{\alpha-Be}$ are drawn. The results are given in figure 5.11 for the α_0 channel and in figure 5.12 for the α_1 one.
The analysis of this plots allows to understand quite easily if peaks in the three-body cross section have to be attributed to the decay of ^{12}C, or to the SD of ^{5}He and ^{9}Be excited states. Indeed if horizontal loci show up, populating a region of constant $E_{\alpha-n}$ or constant $E_{^{8}Be-n}$ this means that an excited state of ^{5}He or ^{9}Be respectively has been populated in the process. Similarly if a locus is present at constant $E_{\alpha-^{8}Be}$ relative-energy, then an excited state of ^{12}C has been fed. The decay of ^{12}C compound system can take place both via a SD or a QF process and additional test are required. In the present case no levels shows up which can be attributed to the ^{5}He and ^{9}Be SD, since only vertical loci are apparent, corresponding to ^{12}C states.

Figure 5.11 show a very clear vertical locus in both upper and lower panel can be attributable to the 16.106 MeV ^{12}C level, corresponding in this case to an energy of about $E_{\alpha-Be}\approx$ 8.7 MeV. Much less defined loci coming from the 1.68 MeV, 2.43 MeV and 3.30 MeV states in ^{9}Be can also detected as horizontal loci in the top panel of Figure 5.11 or as oblique ones in the bottom of the same figure. Also an evidence of $^{5}He_{g.s}$ can be recognized. However, the decays from ^{5}He and ^{9}Be intermediate states leave the final neutron momentum larger than 80 MeV/c, so only the 16.106 MeV state of ^{12}C can contribute within the astrophysical region. Therefore, these events represent a "noise" for the next THM application and their contribution must be reduced as much as possible. For this reason only events for which E_{Be-n} >2 MeV and $E_{\alpha-n}$ > 1.5 MeV will be taken into account for the next steps of the data analysis, that proceeds in order to study only the 16.106 MeV ^{12}C excited state. In fact this level contribute strongly to the behavior of the S(E)-astrophysical factor and then a more detailed study is needed. In particular the energy region of interest can be determined following the definition:

$$E_{c.m} = E_{\alpha Be} - Q_{2body} = E_{\alpha Be} - 8.59 MeV. \tag{5.6}$$

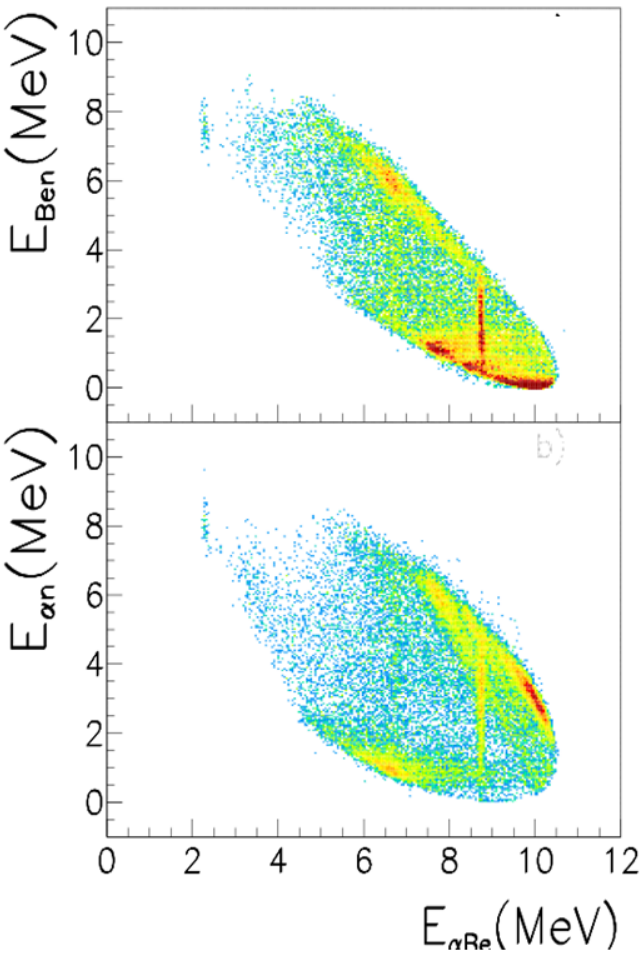

Figure 5.11: Bi-dimensional plot of $E_{\alpha n}$ and E_{Ben} relative energies as a function of $E_{\alpha Be}$. A clear vertical locus correspond to excited state of ^{12}C.

Since at about 8.7 MeV a strong level of ^{12}C is present, it is expected that this level corresponds to the 150 keV resonant contribution to the astrophysical S(E)-factor for the ^{11}B(p,α_0)^{8}Be reaction. Thus next step in analysis is to study the nature of ^{12}C state before extracting the astrophysical S(E)-factor. In Figure 5.12 the relative energy two-dimensional plot for the α_1 channel is shown, in this case there's no evidence of horizontal or vertical loci because the low statistical.

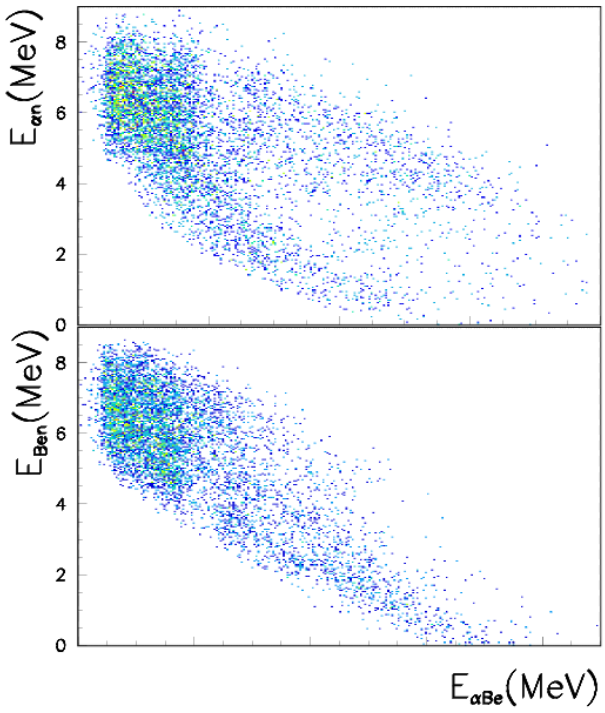

Figure 5.12: Bi-dimensional plot of $E_{\alpha n}$ and E_{Ben} relative energies as a function of $E_{\alpha Be}$.

5.4.2 Data as a function of the neutron momentum

A further test allowing to discriminate between SD and QF reaction mechanism is the study of the correlation plot of the $E_{\alpha-^8Be}$ relative energy and of the neutron momentum p_n. As already discussed, both simple PWIA approach and more advanced MPWBA technique reviewed in chapter 3 predict a clear connection between the three-body cross section and the spectator momentum through the momentum distribution of the undetected third particle in the exit channel.

In fact, in the QF hypothesis, the neutron should maintain in the exit channel the same impulse distribution for the p-n relative motion inside the deuteron that it had before the interaction with the impinging particle. Thus a necessary condition for the occurrence of the QF mechanism is the presence of such correlation between the coincidence yield for the ^{2}H(^{11}B,α^8Be)n three-body reaction and neutron momentum, which can be easily put in evidence by extracting the

$E_{\alpha-^8Be}$ vs. p_n correlation plot. Figure 5.13 shows the $E_{\alpha-^8Be}$ as a function of the neutron momentum p_n in a two-dimensional plot. The typical "butterfly" diagram for the $^{11}B(p,\alpha_0)^8Be$ reaction is shown in the left panel of figure 5.13.

The horizontal loci, that is the ones at fixed $E_{\alpha-^8Be}$ relative energy shows the main contribution of the already mentioned 16.106 MeV state of ^{12}C. This level is confined in the $|p_n|\leq 40$ MeV/c range corresponding to the QF region. In the right panel of the figure 5.13 the $E_{\alpha-^8Be}$ vs p_n two dimensional plot for the $^{11}B(p,\alpha_1)^8Be$ reaction is shown, in this case it is not visible any level and we can not have more information for what concerns this channel of reaction. From this point the data analysis was continued only for the α_0 channel. Anyway the result obtained for the $^{11}B(p,\alpha_0)^8Be$ might be not a sufficient condition, since the discussed correlation can be partially dependent on phase-space effects, regardless of its SD or QF origin. Thus, addition tests are required to establish the presence of the QF contribution. The study of the behavior of the coincidence yield as a function of the neutron momentum p_n, is an important test to evaluate the reaction mechanisms involved in the population of ^{12}C states. The main purpose of this test is to evaluate the modulation of the three-body cross section by the momentum distribution of p-n relative motion inside deuteron. The relative energy $E_{^{11}B-p}$ spectra, are reconstructed for different ranges of the neutron momentum p_n. The $E_{^{11}B-p}$ corresponds to the $E_{c.m.}$ variable defined in equation 5.6. In order to remove the pure kinematic effects due to the experimental phase-space selection the three-body cross section as a function of $E_{c.m.}$ is divided by the kinematic factor evaluated by means of a Monte Carlo calculation.

In this way it is possible to study the momentum dependence of the excitation function as it is shown in figure 5.14. Within 0Mev/c $\leq|p_n|\leq$20 MeV/c and 20Mev/c $\leq|p_n|\leq$40MeV/c momentum ranges, the coincidence yield appears to be quite high, in particular, close to the $E_{^{11}B-p}$ resonant window. Moving a bit further in momentum, the coincidence yield clearly decreases and becomes comparable as shown in Figure 5.14. These experimental data provide further evidence for a strong correlation between coincidence yield and neutron momentum p_n, a necessary condition for the dominance of the QF contribution in the region approaching zero neutron momentum. These experimental evidence allows

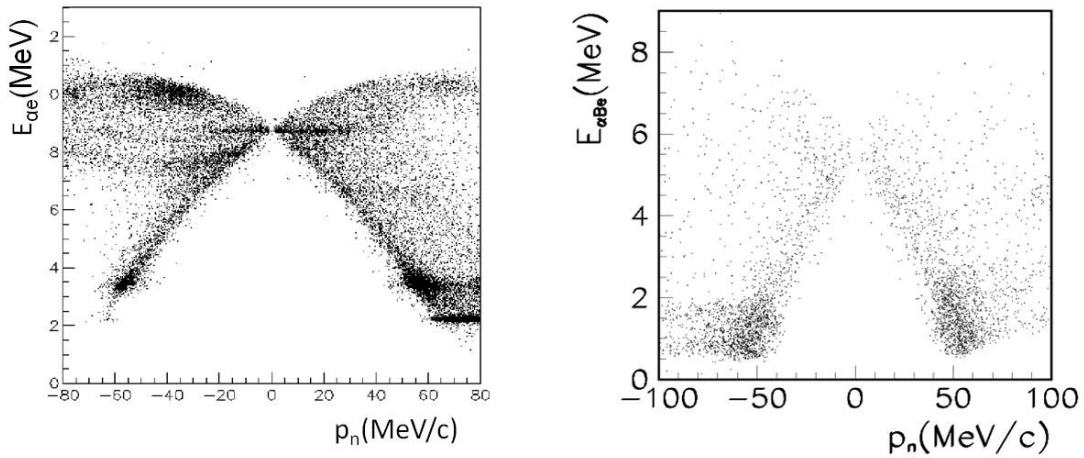

Figure 5.13: Relative energy $E_{\alpha-Be}$ as a function of the spectator momentum p_n. In the left panel the sharp line at 8.7 MeV in the region of low p_n is associated with the 16.106 MeV excited state of ^{12}C, while in the right panel is not evident any level.

then to progress further in the data analysis, in particular in the application of the THM to the selected data.

5.4.3 Experimental Momentum Distribution of the p-n Bound system

In the same way as for the ^{2}H(^{10}B,α ^{7}Be)n reaction, the extraction of the experimental momentum distribution represents a very sensitive test of the reaction mechanism. The experimental momentum distribution is extracted according to equation 4.8, selecting a small energy region $\Delta E \simeq$ 100 keV, where the differential two-body cross section can be regarded as almost constant within such a restricted relative energy range, the three-body coincidence yield correct for the phase-space factor will be proportional to the momentum distribution, applying the same procedure already seen for the ^{2}H(^{10}B,α ^{7}Be)n reaction. The experimental result is shown in Figure 5.15 where the error bars include only the statistical error. The extracted experimental momentum distribution was then compared with the theoretical one, given in terms of a Hulthén wave function in momentum space (see eq. 4.10).

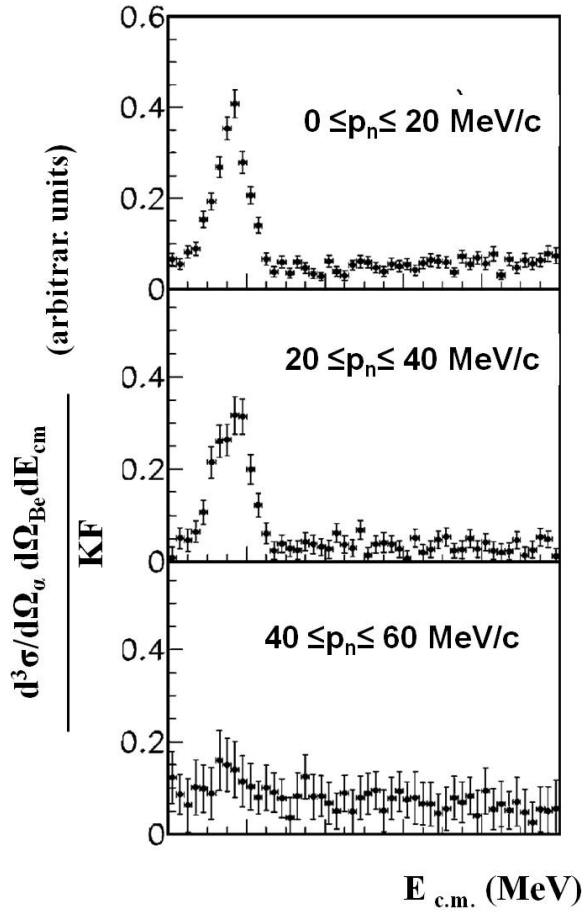

Figure 5.14: Three-body cross section of the ^{2}H(^{11}B,α_0 ^{8}Be)n reaction, divided by the kinematic factor KF. The results for different p_n ranges are reported.

The theoretical distribution was superimposed on the THM data, after being normalized to the experimental maximum. The good agreement between the experimental data and the theoretical Hulthé wave function represent the experimental evidence that the neutron acted as a "spectator" during the break-up occurred in the ^{2}H(^{11}B,α_0^{8}Be)n reaction.

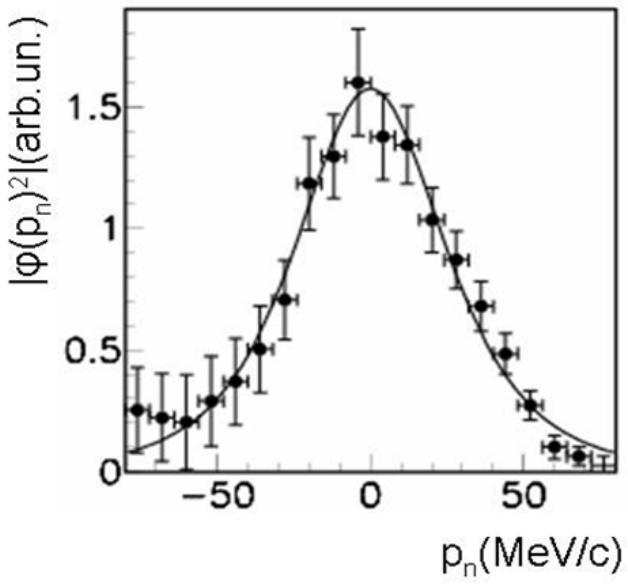

Figure 5.15: Experimental momentum distribution (full dots) compared with the theoretical momentum distribution given in terms of Hulthén function (full line).

5.5 Determination of the Astrophysical S(E)-factor.

After the selection of the reaction channel, and after checking the presence of the QF-mechanism on the same data, only the experimental data of the three-body ^{2}H(^{11}B,α_0 ^{8}Be)n channel corresponding to the range -30<p_n<30 MeV/c has been selected. A Monte Carlo simulation was then performed to extract the KF$|\Phi(\overrightarrow{p_n}|^2$ product where the geometrical efficiency of the experimental setup as well as detection threshold of the PSD's were taken into account. Following the PWIA prescription, as explained for the ^{10}B(p,α)^{7}Be analysis, the two-body cross section was derived by dividing the selected three-body coincidence yield by the result of Monte Carlo simulation. The experimental coincidence yield on the variable $E_{c.m}$=$E_{\alpha Be}$-8.59 (MeV) is shown in figure 5.16 where there is evidence of a well separated peak at about 150 keV. By using standard error propagation, it was also possible to estimate an average experimental resolution of about 40 keV's on the E_{cm} quantity. Because this experimental resolution the width of

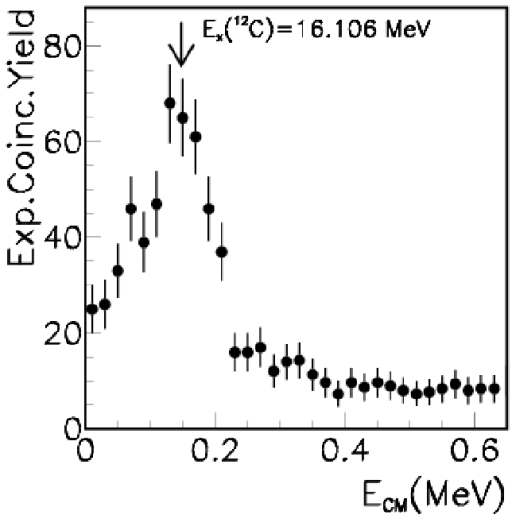

Figure 5.16: Experimental coincidence yield for the selected data as explained in the text. Is evident the peak at about 150 keV that correspond to the 16.106 MeV ^{12}C level.

the E_{cm}=150 keV level is about E_{cm}=100 keV that is larger if compared to the natural width Γ=5keV's [Ajezenberg-Selove (1988)]. As already explained, since this approach provides the off-energy-shell two-body cross section it is necessary to perform the appropriate validity test for the adopted IA.

5.5.1 Validity test: Angular distribution

In order to perform an appropriate validity tests on the deduced cross section for the adopted IA, the comparison between the indirectly and direct angular distribution has been performed [Becker *et al.* (1987)]. The emission angle of the alpha-particle in the α-^{8}Be center-of-mass system, can be calculated according to the relation [Jain *et al.* (1970):

$$\theta_{c.m.} = \arccos \frac{(\overrightarrow{v}_p - \overrightarrow{v}_t) \cdot (\overrightarrow{v}_C - \overrightarrow{v}_\alpha)}{|\overrightarrow{v}_p - \overrightarrow{v}_t||\overrightarrow{v}_C - \overrightarrow{v}_\alpha|} \tag{5.7}$$

where the vectors $\overrightarrow{v}_p$, $\overrightarrow{v}_t$, $\overrightarrow{v}_C$ and $\overrightarrow{v}_\alpha$ are the velocities of projectile, transferred proton, and the outgoing ^{8}Be and α particles, respectively. These quantities are

calculated from their corresponding momenta in the laboratory system, where the momentum of the transferred particle is equal and opposite to that of neutron when the quasi-free assumption is fulfilled. The present experiment allows to cover a center of mass angular ranges $\theta_{c.m.}$=120°-160°, $\theta_{c.m.}$=75°-120°, and $\theta_{c.m.}$=20°-60°. The angular distributions are extracted for three different energies, within the astrophysical relevant α-^{8}Be relative energy in steps of $\Delta E_{c.m.}$=200 keV.

The results are given in Figure 5.17 where the different energies are marked for each distribution. Normalization is performed over the whole angular region. In Figure 5.17 for each E_{cm} energy the angular distribution is compared with the direct data from Becker et al. 1987. The errors bars affecting THM data are given as the sum of the statistical and normalization errors, the normalization constants and their uncertainties being determined by adjusting the indirect data to the trend of the direct ones for each energy. The solid lines show the behavior of the direct angular distribution integrated in the same energy bins. A quite good agreement between the two trends shows up, confirming the validity of the PWIA in the present experimental conditions. Moreover the direct data present a strong contribution of second order polynomial in describing angular distribution that is correlated to the presence of an l=1 resonant contribution just in the region of about 150 keV in $E_{c.m.}$. From this evidence we have to consider in the further analysis the different non resonant l=0 and resonant l=1 contribution in order to extract the astrophysical S(E)-factor.

5.5.2 Validity test II: Excitation function

A second validity test, as well as for the previous analysis, is the study of the behavior of the indirect excitation function in order to check whether the off-energy-shell binary cross section integrated over the full $\theta_{c.m.}$ range is consistent with the direct data [Becker *et al.* (1987)]. The 'nuclear' differential two-body cross section of the^{11}B(p,α_0)^{8}Be reaction is reported in figure 5.18,

The 'nuclear' two-body cross section is expressed in arbitrary units since the Coulomb barrier suppression effect has be to introduced to the indirect data to

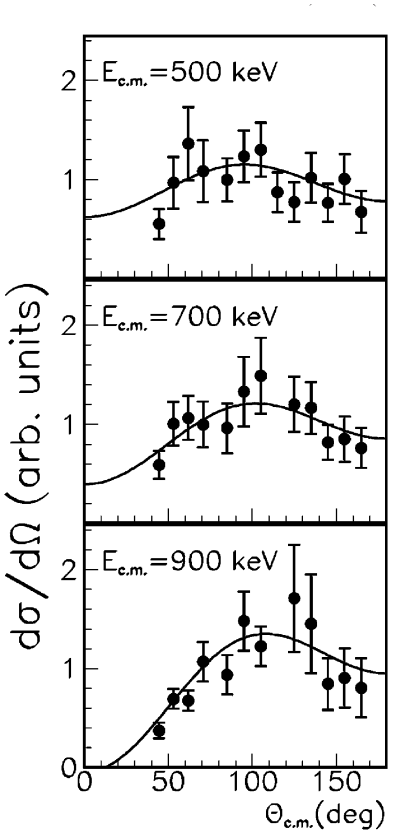

Figure 5.17: Indirect angular distribution for the ^{11}B(p,α)^{8}Be reaction(full dots) for different $E_{c.m.}$ energies (marked in each picture). The THM angular distribution are also compared with the direct one from [Becker *et al.* (1987)] (solid lines).

compare their trend to the direct one. At this point is necessary the normalization to direct data. In order to make this the effects of penetrability through the Coulomb barrier must be introduced. Moreover, in the actual case, the excitation function, expressed in terms of the "bare-nucleus" cross section ($d\sigma^N/d\Omega$) shows up a resonant l=1 contribution due to the 16.106 MeV of ^{12}C level superimposed on a non resonant l=0 contribution. In order to distinguish between the two partial waves contributing to the TH "bare-nucleus" cross section, a fit was performed for the data, by using the incoherent sum between a second order polynomial and a gaussian function. Once that the non-resonant l=0 contribution and resonant l=1 one were evaluated, the penetrability function was separately calculated for the two contribution using the usual definition, as described for the

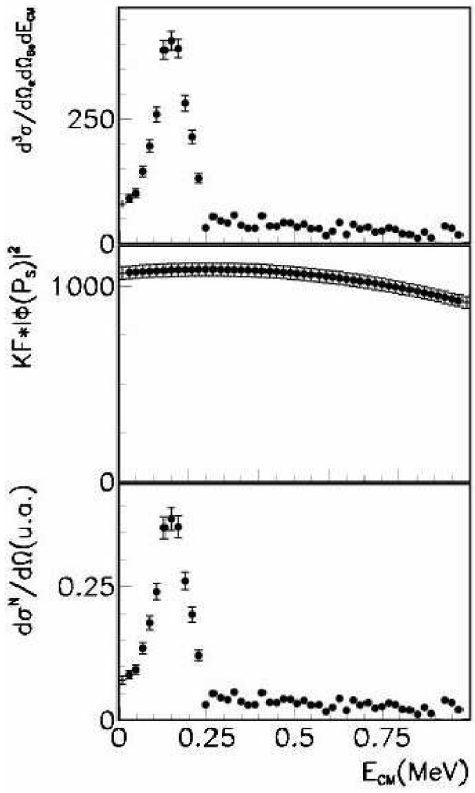

Figure 5.18: From three-body coincidence yield to the 2-body cross section. In the upper panel is reported the three-body coincidence yield that was divided for the KF|Φ p_n|^2 kinematic factor shows in the middle panel. The result two-body cross section in arbitrary units is shown in the bottom panel.

^{10}B(p,α)^{7}Be reaction:

$$P_l(k_{11B-p}R) = \frac{1}{F_l^2(k_{11B-p}R) + G_l^2(k_{11B-p}R)} \tag{5.8}$$

where F_l and G_l are the regular and irregular Coulomb wave function, k_{11B-p} and R the ^{11}B-p relative wave number and interaction radius respectively [Spitaleri *et al.* (2001)]. Assuming a dominant l=0 partial wave in the entrance channel of the ^{11}B-p binary reaction the two-body cross section was extracted and compared with direct data. The result is shown in Figure 5.19 where the TH data (full dots) were normalized in the region $E_{^{11}B-p}$ =800-900 keV to the direct data (open symbols).

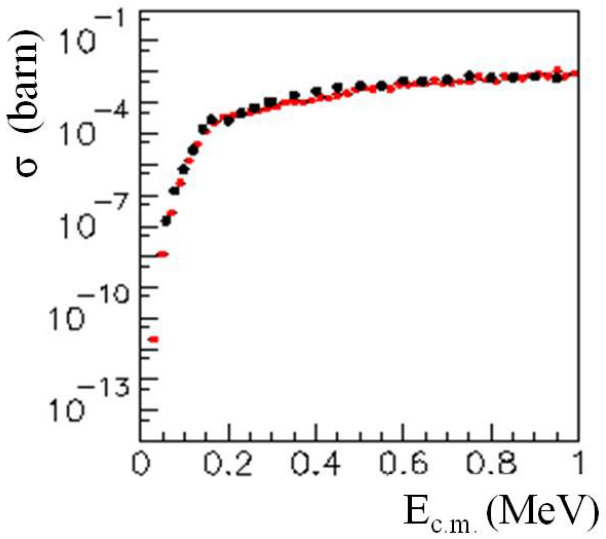

Figure 5.19: Comparison between the indirect excitation function (full dots) for the ^{11}B(p,α_0)^{8}Be reaction and the direct behavior (open symbols)[Becker *et al.* (1987)].

Good agreement between the data sets shows up, revealing that the assumption for a dominant l=0 partial wave is correct within the accuracy of the experimental information available. Moreover this good agreement represent a necessary condition for the further extraction of the astrophysical S(E)-factor.

5.5.3 S(E)-astrophysical factor

Next step of the THM investigation was the extraction of the astrophysical S(E)-factor. Before to extract the S(E)-factor we observed that our experimental resolution on the energy, $E_{c.m.}$ 40 keV, is quite larger if compared to that of about 5 keV reported by the direct measurements [Becker *et al.* (1987), Angulo *et al.* (1993)]. This means, that the direct and indirect data are not directly comparable. So, also in this case, a "Smearing out" of direct data was performed.

In particular, the experimental fit on direct data [Becker *et al.* (1987)] was described by:

$$S(\alpha_0, E)^{dir} = 2.1 - 1.26E - 0.14E^2 + \frac{0.69 \cdot 10^{-3}}{(E - 0.148)^2 + 7.13 \cdot 10^{-6}} \qquad (5.9)$$

where the energy E is expressed in MeV and S(α_0, E)^{dir} in MeV b. This formula described the sum of several gaussian functions, each of them having the correspondent standard deviation comparable with our experimental resolution. The smeared-out function describing the direct data [Becker *et al.* (1987)] can be expressed as:

$$S(\alpha_0, E)^{smear} = 2.1 - 1.37E - 0.14E^2 + 7.99 * \exp\left[-0.5\left(\frac{E - 0.148}{0.04}\right)^2\right] \quad (5.10)$$

The comparison between the behavior of direct data and their fit smearing out is reported in Figure 5.20. This function was used to extract the S(E)-factor through the THM allowing us a normalization to the l=0 as well l=1 contribution.

After the separation of the resonant and non-resonant contribution the total astrophysical factor was extracted as a sum between the two contributions after their normalization to the direct "smeared-out" data. The normalization was performed for non-resonant energy region between 400-600 keV, the associated errors were estimated at about 10%, whereas for l=1 the normalization to the area was chosen as normalization criterion with an error of about 5%. The extracted astrophysical factor is reported in Figure 5.21 with black points, while the histogram represent the smeared out function of the direct data, the error bars in this figure refers only the statistical one about 25% on the non-resonant part and about 10% close the 150 keV resonant level. In this S(E)-factor is evident the l=1 contribution and it is possible, thanks to the power of the method, to reach the region around the Gamow peak giving an experimental value at about 10 keV.

The experimental indirect data were then fitted using the analytic relation:

$$S(\alpha_0, E)^{TH} = 2.04 - 1.24E - 0.12E^2 + 7.36 * \exp\left[-0.5(\frac{E - 0.148}{0.044})^2\right] \quad (5.11)$$

The result is shown in figure 5.21 with solid line. Using this formula it is possible to obtain the value of S(0)=2.07 $\pm$0.29 (MeV b) for the zero energy bare nucleus where the total error takes into account the uncertainties on the normalization procedure and the statistical error on the experimental points. The value obtained through this procedure is in good agreement with the extrapolated one [Becker *et al.* (1987)].

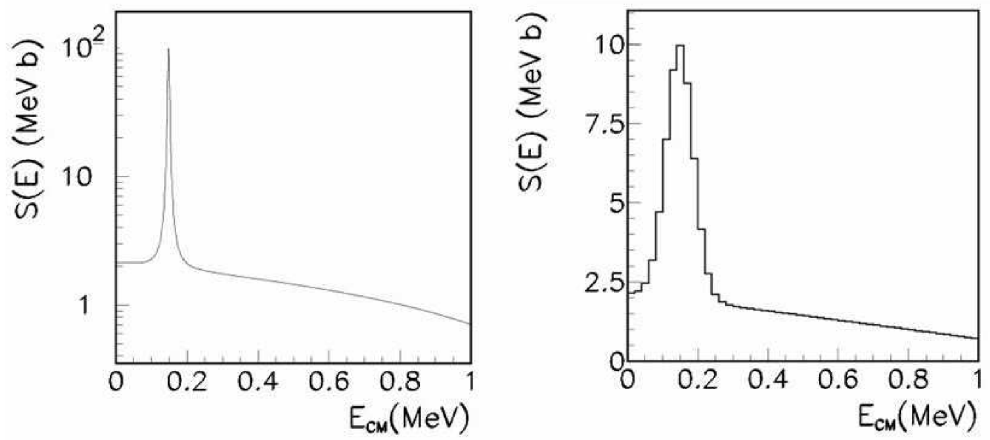

Figure 5.20: Left panel: fit on the direct data [Becker *et al.* (1987)] whit extrapolation down to zero. Right panel: smearing out of the direct data with our energy resolution of about 40 keV.

This value is in disagreement with the previous one [Spitaleri *et al.* (2004)] and this discrepancy mainly is due to the presence of sequential mechanism, i.e. contribution of ^{9}Be compound nucleus.

5.6 Electron screening potential

As explained in chapter 3 the presence of the electron screening effects prevents one to measure the bare nucleus cross-section in correspondence of the Gamow peak, which is necessary for the astrophysical application. Nuclear cross section measured in laboratory exhibit in fact an enhancement of their values through the factor

$$f_{enh} = \frac{\sigma_{sh}}{\sigma_b} \approx \exp(\pi\eta\frac{U_e}{E}) \tag{5.12}$$

where σ_{sh} is the shielded nuclear cross section measured in laboratory, σ_b is the bare-nucleus cross section of interest for astrophysical application and U_e is the electron screening potential in the laboratory. After the extraction of the astrophysical S(E)-factor it is possible to give an evaluation of the electron screening

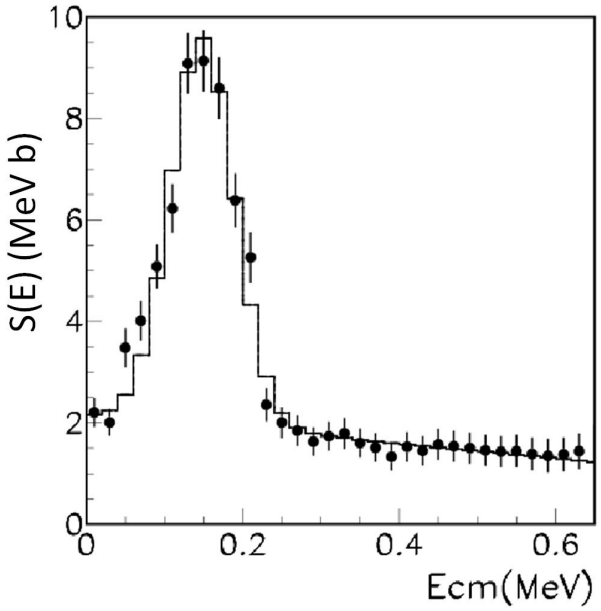

Figure 5.21: Astrophysical S(E)-factor extracted by means of THM for the ^{11}B(p,α_0)^{8}Be reaction (black point) compared to the smeared out function of direct data (histogram).

potential for the ^{11}B(p,α_0)^{8}Be reaction. In order to make the extraction of the electron screening U_e potential we used the direct data reported in [Angulo *et al.* (1993)] normalized to that [Becker *et al.* (1987)]. In Angulo *et al.* (1993) the data reported as a sum between both α_0 and α_1 contribution, being the former evaluated about 1/100 of the total S(E) factor. The U_e reported in Angulo *et al.* (1993) has been extracted by means of an extrapolation of the bare nucleus S(E)-factor. The obtained value was U_e=430±80 eV. In this work, the same direct data [Angulo *et al.* (1993)] have been fitted with:

$$S(E)_{sh} = S(E)_b * \exp(\pi\eta\frac{U_e}{E}) \tag{5.13}$$

where in this case, $S(E)_b$ is the experimental bare nucleus S(E)-factor given by the sum between non-resonant contribution extracted via THM and the resonant one reported in [Becker *et al.* (1987)]. Using this equation to fit the experimental data with U_e the only free parameter we obtained the value of $U_e{}^{THM}$ =502±140eV for the ^{11}B(p,α_0)^{8}Be reaction.

Chapter 6

Conclusions

In this thesis, the indirect study of ^{10}B(p,α)^{7}Be and ^{11}B(p,α)^{8}Be reactions have been reported. For each reaction the astrophysically relevant parameters, S_b(E)-factor and electron screening potential U_e were derived and compared with the ones from literature.

A particular interest was devoted to the study of the ^{10}B(p,α)^{7}Be reaction. From the study of ^{7}Be-α relative energy, information on the presence of excited states of ^{11}C has been obtained. In particular the E_x=8.701 MeV ^{11}C resonant level (J=5/2$^+$) has been showed up. This level lies in the Gamow peak region that is $E_{c.m.}$=10 keV. The cross section energy dependence of this reaction has been extracted via the THM and the 10 keV resonance has been experimentally reproduced, for the first time. The, experimental THM data were compared with the extrapolated S(E)-factor reported in literature [Angulo *et al.* (1993)]. This comparison confirmed (within experimental errors) the extrapolated S(E)-factor behavior [Angulo *et al.* (1993)], and we extracted the value of S(10 keV)=1378$\pm$207. Moreover, from comparison with direct data we obtained a value for the electron screening potential U_e=448$\pm$69.

Regarding the ^{11}B(p,α)^{8}Be reaction, the study was addressed by improving the condition of the previous measurements; so with the same procedure was obtained the value of a S(E)-factor, S(0)=2.07 $\pm$0.29 (MeV b) also in agreement (within experimental errors) with the extrapolated value given in literature [Becker *et al.* (1987)]. In this analysis, the α_1 channel was also reconstructed, but due to experimental conditions a full analysis as well as in the case of α_0 channel

was not possible.

A very interesting result, regards the measurement of electron screening potential for ^{10}B(p,α)^{7}Be and ^{11}B(p,α)^{8}Be reactions. The U_e value obtained in this thesis for both reactions are in agreement, according to the "isotopical independence" of the electron screening potential, which should be influenced only by the electrons number, even with different masses of the interacting particles. The error on the values of U_e turns out to be about 30%, so new measurements using 4π apparatus, would be appropriate to improve the statistical.

Acknowledgements

Retracing my way, I think and thank all those who at different times and in different ways, have offered me their help and assistance in carrying out this work.
First I would to thank my tutor Prof. Claudio Spitaleri, that since the time of graduation, conducted me in the nuclear astrophysics environment, with great helpfulness and infinite patience. A warm acknowledge to prof G.Giaquinta, for his valuable work as coordinators of PHD course.
Most of what i learned in these years is due especially to Dr. Stefano Romano, who has followed me step by step in this path, his support and his valuable teaching for me have been indispensable.
I also thank the member of the Asfin Group in Catania, and special thanks to Dr. Pizzone and Dr.La Cognata for the help and the time spent for me to the end. I want to thanks kindly Dr.Lamia and Dr.ssa Sergi for their availability and friendship, very important during all my work.
Lastly, I would like to thank my family for all their love, the encouragement and their supported me in all my pursuits.
Thank you Alessio, for always been there, for sharing with me all the moments that in these years I went through.

References

Ajezenberg-Selove, F. (1988). *Nucl.Phys.A*, **490**, 1. 123, 130, 131, 162

Alcaraz, J. *et al.* (2000). *Phys.Lett.B*, **490**, 27. 11

Aliotta, M. *et al.* (2001). *Nucl. Phys. A.*, **690**, 790. 70

Anders, E. & Grevesse, N. (1989). *Geochimica et cosmochimica acta*, **53**, 197. 24, 26, 36

Angulo, C. *et al.* (1993). *Z.Phys.A*, **345**, 231. ix, 104, 105, 106, 134, 137, 139, 140, 141, 143, 166, 169, 170

Arnould, M. & Norgaard, H. (1975). *A&A*, **42**, 55. 16

Asplud, M., Lambert, D.L., Nissen, P.E., Primas, F. & Smith, V. (1986). *Apj*, **644**, 229. 21

Assenbaum, H.J. (1987). *Z-Phys*, **327**, 461. 22, 67, 144

Bania, T.M., Rood, R.T. & Balser, D.S. (2002). *Nat*, **415**, 54. 6

Barnes, G., Charbonneau, P. & Macgregor, K.B. (1999). *APJ*, **511**, 466. 38

Baur, G. & Rebel, H. (1994). *J.Phys.G*, **20**, 1. viii, 77, 80

Baur, G. *et al.* (1986). *Nucl.Phys.A*, **458**, 188. viii, 79, 85

Becker, H.W. *et al.* (1987). *Z.Phys.*, **327**, 341. x, 143, 144, 147, 162, 163, 164, 166, 167, 168, 169, 170

Bodenheimer, P. (1965). *Apj*, **142**, 451. 42

Boesgaard, A.M. (1976). *Astron.Soc.of the Pacific*, **88**, 353. 35

Boesgaard, A.M. & King, J.R. (2002). *Apj*, **565**, 587. 23, 27, 28

Boesgaard, A.M. & Tripicco, M.J. (1986). *Apj*, **303**. 22, 26, 42

Boesgaard, A.M., Deliyannis, C.P., Stephens, A. & Lambert, D.L. (1998). *ApJ*, **492**, 727. 25, 26, 35, 43, 47, 50

Boesgaard, A.M., Deliyannis, C.P., King, J.R., Ryan, S.G., Vogt, S.S. & Beers, T.C. (1999). *ApJ*, **117**, 1549. 23, 24

Boesgaard, A.M., Stephens, A., King, J.R. & Deliyannis (2000). *Proc. SPIE*, **4005**, 142. 23, 24

Boesgaard, A.M., Deliyannis, C.P., King, J.R. & Stephens, A. (2001). *ApJ*, **553**, 754. 18, 23, 24, 33

Boesgaard, A.M., Armengaud, E. & King, J.R. (2003). *Apj*, **582**, 410. 29

Boesgaard, A.M., Armengaud, E. & King, J.R. (2004a). *Apj*, **605**. vii, 20, 23, 25, 26, 29, 30, 32, 33, 37, 39, 50

Boesgaard, A.M., Armengaud, E., King, J.R., Deliyannis, C.P. & Stephens, A. (2004b). *Apj*, **613**. vii, 31

Boesgaard, A.M., Deliyannis, C.P. & Steinhauer, A. (2005). *Apj*, **621**, 991. vii, 34

Bonifacio, P. & Molaro, P. (1997). *MNRAS*, **285**, 847. 21

Boothroyd, A.I., Sackmann, I.J. & Fowler, W.A. (1991). *Apj*, **377**, 318. 44

Bracci, L., Fiorentini, G., Melezhik, V.S., Mezzorani, G. & Quarati, P. (1990). *Nucl.Phys.A*, **513**, 316. 70

Burbridge, E.M., Burbridge, G.R., Fowlerand, W.A. & Hoyle, F. (1957). *Rev.Mod.Phys*, **29**, 547. vi, 1, 8

Calvi, G. *et al.* (1997). *Nucl.Phys.A*, **621**, 139. 85

Cameron, A.G. & Fowler, W.A. (1971). *Apj*, **164**, 111. 1

Castellani, V. (1981). *Introduzione all'astropisica nucleare*. Roma, newton compton edn. 40, 41

Chant, N.S. & Roos, P.G. (1977). *Phys, Rev.C*, **15**, 57. 88

Charbonnel, C. & Vauclair, S. (1998). *arXiv::asroph/9812255*, **v1**, 14. 47

Charbonnel, C., Vauclair, S. & Zahn, J. (1988). *Apj*, **334**, 746. 42, 48

Charbonnel, C., Vauclair, S. & Zahn, J. (1992). *A&A*, **255**, 191. 48

Charbonnel, C., Vauclair, S., Maeder, A., Meynet, G. & Shaller, G. (1994). *A&A*, **255**, 191. 48

Cherubini, S., Kondratyev, V.N., Lattuada, M., Spitaleri, C., Miljanic, D. & Zadro, M. (1996). *Astroph.J*, **457**, 855. viii, 85

Chew, G.F. & Wick, G.C. (1952). *Phys.ReV*, **85**, 636. 86

Chiosi, C. (2009). *AIP conference proceedings*, **1213**, 42. 4

Copi, C.J., Schramm, D.N. & Turner, M.S. (1995). *Science*, **627**, 192. 3

Croft, R.A.C., Weinberg, D.H., Bolte, M., Burles, S., Hernquisit, L., Katz, N. & Kirkman, a.T.D., Denis (2002). *Apj*, **581**, 20. 4

Cunha, K., Smith, V.V., Boesgaard, A.M. & Lamber, D.L. (2000). *Apj*, **530**, 939. 26

Cyburt, R.H. (2005). *Nucl.Phys.A*, **758**, 771. 5

D'Antona, F. & Ventura, P. (2010). *Proceedings IAU Symposium*, **268**. 16

D'Antona, F.D. & Matteucci, F. (1991). *A&A*, **248**, 62. 15

D'Antona, F.D. & Mazzitelli, I. (1982). *ApJ*, **260**, 722. 16

D'Antona, F.D. & Mazzitelli, I. (1984). *A&A*, **138**, 431. 42

Deliyannis, C.P. & Pinsonneault, M.H. (1993). *ASP Conf.Proc.40, Inside the Stars(IAU Colloq.137)*, **174**. 44, 45, 47

Deliyannis, C.P., Boesgaard, A.M. & King, J.R. (1995). *Apj*, **452**. vii, 25, 43

Deliyannis, C.P., Boesgaard, A.M., Stephens, A., King, J.R., Vogt, S.S. & Keane, M.J. (1998). *Apj*, **498**. 33, 39, 49

Domogatsky, G.V., Eramzhyan, R.A. & Nadyozhin, D.K. (1978). *Proc.Int.Conf.on Neutrino Physics and Neutrino Astrophysics*, **115**. 17

Duncan, D.K., Prima, F., Rebull, L.M., Boesgaard, A.M., Deliyannis, C.P., Hobbs, L.M., King, J.R. & Ryan, S.G. (1997). *Apj*, **488**, 388. 26

Duncan, D.K., Rebull, L.M., Prima, F., Boesgaard, A.M., , Deliyannis, C.P., Hobbs, L.M., King, J.R. & Ryan, S.G. (1998). *A&A*, **332**, 1017. 26

Englester, S. *et al.* (1992). *Z.Phys.A*, **342**, 471. 96, 98, 100, 102

Fields, B., Olive, K.A., Vangioni Flam, E. & Cass, M. (2000). *ApJ*, **540**, 930. 17

Gagliardi, C.A. *et al.* (1998). *Phys. RevC*, **59**, 1149. 82

Gamow, G. (1928). *Z. Phys.*, **51**, 204. 58

Garca Lopez, R.J. & Spruit, H.C. (1991). *Apj*, **377**, 268. 42, 47

Garca Lopez, R.J., Severino, G. & Gomez, M.T. (1995). *A&A*, **297**, 787. 44

Garca Lopez, R.J., Lambert, D.L., Edvardsson, B., Kiselman, D. & Rebolo, R. (1998). *Apj*, **500**, 241. 26

Gilmore, G., Gustafsonn, B., Edvardsson, B. & Nissen, P.E. (1992). *Nature*, **357**, 379. 23

Gnedin, N.Y. & Hamilton, A.J.S. (2002). *MNRAS*, **334**, 107. 4

Grevesse, N. & Sauval, A. (2001). *Encyclopedia of Astronomy and Astrophysics*. Institute of Phys.Publis. 9

Grevesse, N. & Sauval, A.J. (1998). *Sp.Sci.Rev.*, **85**, 168. 26

Hesse, V.F. (1936). *Unsolved Problems in Physics: Tasks for the Immediate Future in Cosmic Ray Studies*, **171**. 8

Iben, I.J. (1973). *ApJ*, **185**, 209. 16

Jain, M., Roos, P.G., Pugh, H.G. & Holgrem, H.D. (1970). *Nucl. Phys.A*, **153**, 49. 86, 88, 133, 134, 162

Jedamiz, K. & Rehm, J.B. (2001). *arxiv:astro-ph/010129217*. 23

Kiener, J. (2009). *AiP Conference Proceedings*, **1213**, 95. vi

Kirkman, D., Tytler, D., Suzuki, N., O'Meara & Lubin, D. (2003). *ApjS*, **149**, 1. 6

Kraft, R.P. (1967). *Apj*, **150**, 551. 48

La Cognata, M. *et al.* (2005). *Phys.ReV.C*, **72**, 065802. 89, 97, 99, 129, 135

La Cognata, M. *et al.* (2006). *Eur.Phys.J A*, **27**. 85, 99

La Cognata, M. *et al.* (2007). *PRC*, **76**, 065804. 92, 95

La Cognata, M. *et al.* (2008). *J.Phys.G:Nucl Part.Phys.*, **35**, 014014. 99

La Cognata, M. *et al.* (2010). *ApJ*, **708**, 796. 92

Lambert, D.L., Sheffer, Y., Federman, S.R. *et al.* (1998). *ApJ*, **494**, 614. 35

Lamia, L. *et al.* (2007). *Nucl.Phys.A*, **787**, 309. 99, 100, 105, 106

Lane, A.M. & Thomas, R.G. (1958). *Rev.Mod.Phys.*, **30**, 257. 91, 92

Lattuada, M., Pizzone, R.G., Typel, S., Figuera, P., Miljanic, D., Musumarra, A., Pellegriti, M.G., Rolfs, C. & Spitaleri, C. (2001). *ApJ*, **562**, 1076. 71, 89

Lemoine, M., Vangioni-Flam, E. & Cass, M. (1998). *Apj*, **499**, 735. 34

Mahaux, C. & Weidenmüller, H.A. (1969). *Shell Model approach to Nuclear Reactions*. 93

Malaney, R.A. & Mathews, G. (1993). *Phys.Rep.*, **229**, 147. vi, 3

Mazzitelli, I., D'Antona, F. & Ventura, P. (1999). *A&A*, **348**, 846. 16

Meneguzzi, M., Audouze, J. & Reeves, H. (1971). *A&A*, **15**, 337. 9, 12, 13

Menn, W. *et al.* (2000). *APJ*, **533**, 281. 11

Michaud, G. & Charbonneau, P. (1991). *Space Sci. Rv.*, **57**, 1. 42, 44, 46

Michaud, G. *et al.* (1986). *Apj*, **302**, 650. vii, 42, 46, 47

Mihalas, D. (1968). *Galactic Astronomy*. Freeman and Company. 19, 20

Mukhamedzanov, A. & Tribble, R.E. (1999). *Phy.Rev.C*, **59**, 1302. viii, 80, 81, 82

Mukhamedzanov, A. *et al.* (2005). *arxiv:nucl th/0509035*, 15. 81

Mukhamedzanov, A. *et al.* (2006). *Eur.Phys J.*, 205. 82

Mukhamedzanov, A. *et al.* (2008). *J.Phys.G.:Nucl.Part.Phys.*, **35**, 014016. 94

Musumarra, A. *et al.* (2001). *Phys.Rev.C*, **64**, 068801. 89, 96

Nagano, M. (2009). *New.J.Phys.*, **11**, 065002. 10

Olive, K.A., Prantoz, N., Scully, S. & Vangioni Flam, E. (1994). *ApJ*, **424**, 666. 17

Pearson, T.J. (2003). *Apj*, **591**, 596. 4

Peimbert, M., Luridiana, V. & Peimbert, A. (2007). *Apj*, **667**. 7

Percival, W.J. (2001). *MNRAS*, **327**, 1297. 4

Pinsonneault, M., Kawaler, S.D. & Demarque, P. (1989). *Apj*, **338**, 424. 48

Pinsonneault, M., Kawaler & Demarque, P. (1990). *ApjS*, **74**, 501. vii, 41, 42, 47, 48

Pinsonneault, M.H., Walker, T.P., Steigman, G. & Naranyan, V.K. (1999). *ApJ*, **527**, 180. 21

Pinsonneault, M.H., Steigman, G. & Walker, a.N.V.K., Tail Paol (2002). *ApJ*, **574**, 398. 21

Pizzone, R.G. *et al.* (2003). *Nucl.Phys.C*, **718**, 496. 96, 99, 100

Pizzone, R.G. *et al.* (2005). *A&A*, **438**, 779. 99, 100

Primas, F., Duncan, D.K., Peterson, R.C. & Thorburn, J.A. (1999). *A&A*, **343**, 545. 24, 26, 50

Primas, F., Molaro, P., Bonifacio, P. & Hill, V. (2000). *A&A*, **362**. 23, 24

Raiola, F. *et al.* (2001). *Eur.Phys.J.A*, **10**, 487. 72

Raiola, F. *et al.* (2004). *Eur.Phys.J.A*, **19**, 283. 74

Ramaty, R., Kozlovsky, B., Lingenfelter, R.E. & Reeves, H. (1997). *ApJ*, **488**, 730. 34

Ramaty, R., Scully, S.T., Lingenfelter, R.E. & Kozlovsky, B. (2000). *ApJ*, **534**, 747. 17, 23

Reeves, H. (1972). *Phys.Rev.D*, **6**, 3363. 5, 6, 7

Reeves, H. (1994). *Rev.Mod.Phys*, **66**, 193. 1

Reeves, H., Fowler, W. & Hoyle, F. (1970). *Nature*, **226**. vi, 8, 12, 13, 23

Richard, O., Michaud, G. & Richer, J. (2005). *Apj*, **619**, 538. 21

Richer, J. & Michaud, G. (1993). *Apj*, **416**, 312. 46, 48

Rinollo, a.o., Angelo (2005). *Nucl.Phys.A*, **758**, 146. 97, 99

Rolfs, C. & Rodney, W.S. (1988). *Cauldrons in the Cosmos*. The University of Chicago press. 12, 13, 44, 57, 60, 62, 64, 66, 68, 69, 73

Romano, D., Matteucci, F., Molaro, P. & Bonifacio, P. (1999). *A&A*, **352**, 117. 17, 19

Romano, D., Tosi, M., Matteucci, F. & Chiappini, C. (2003). *MNRAS*, **346**, 295. 6

Romano, S. & others. (2008). *J.Phys.G: Nucl. Part. Phys.,*, **35**, 014008. 85

Romano, S. *et al.* (2004). *Nucl.Phys.A*, **738**, 406. 99, 100

Romano, S. *et al.* (2006). *Eur.Phys.J*. 99, 100

Roos, P.G., Chant, N.S., Goldberg, D.A., Holdgren, H.D. & Woody, R. (1976). *Phys.ReV.C*, **15**, 69. 88

Ryan, S.G., Beers, T., Olive, K.A., Fields, B.D. & Norris, J.E. (2000). *Apj*, **530**. 8

Ryan, S.G., Kajino, T., Beers, T., Suzuki, T.K., Romano, D., Matteucci, F. & Rosolankova, K. (2001). *Apj*, **549**, 55. 19

Sackmann, I.J., Smith, R.L. & Despain, K.H. (1999). *ApJ*, **187**, 555. 16

Santos, N.C., Garca Lopez, R.J., Israelian, G., Mayor, M., Rebolo, R., Garcia-Gil, A., Perez, M.R. & Randich, S. (2002). *A&A*, **386**, 1028. 23, 24

Satchler, G.R. (1990). *Introduction to nuclear reaction*. II edition,ed. MacMillan. 63

Sattarov, A. *et al.* (1999). *Phys Rev*, 035801. 82

Scalo, J.M., Despain, K.H. & Ulrich, R.K. (1975). *APJ*, **196**, 805. 16

Schramm, D.N., Steigman, G. & Dearborn, D. (1990). *APJ*, **259**. vii, 42

Schroeder, U. *et al.* (1987). *Nucl.Phys A.*, **210**, 240. 82

Sergi, M.L. *et al.* (2010). *Phys.Rev.C*, **82**, 3. 99

Spergel, D.N. (2004). *ApjS*, **148**, 175. 4

Spitaleri, C., Aliotta, M., Cherubini, S., Lattuada, M., Milyanic, D., Romano, S., Soic, N., Zadro, M. & Zappal, R.A. (1999). *Phys Rev C*, **60**, 055802. viii, 85, 87, 88, 128, 138

Spitaleri, C., Typel, S., Pizzone, R.G. *et al.* (2001). *Phys. Rev. C*, **63**, 055801. viii, 85, 89, 107, 135, 165

Spitaleri, C. *et al.* (2004). *Phys Rev.C*, **69**, 055806. 88, 99, 100, 126, 128, 129, 135, 138, 144, 168

Spite, F. & M. Spite, M. (1982). *A& A*, **115**, 357. 7, 15, 20, 21

Spite, M. *et al.* (1996). **307**, 172. 21

Starrfield, S., Truran, J.W., Sparks, W.M. & Arnould, M. (1978). *Apj*, **222**, 735. 16

Stephens, C., Boesgaard, A.M., King, J. & Deliyannis, C.P. (1997). *Apj*, **491**, 339. vii, 23, 24, 25, 43, 45, 48, 50

Strieder, F. *et al.* (2001). *Naturwissenschaften*, **88**, 461. 144

Thorburn, J. & Beers, T.C. (1993). *ApJ*, **404**. 20, 21

Thorburn, J. *et al.* (1994). *ApJ*, **421**, 318. 20

Timmes, F.X., Woosley, S.E. & Weaver, T.A. (1995). *ApjS*, **98**, 617. 2

Tumino, A. *et al.* (2003). *Phys.Rev.C*, **67**, 065803. 85, 99, 100, 107, 135

Tumino, A. *et al.* (2005). *Eur.Phys.J*. 99, 100

Tumino, A. *et al.* (2006). *Eur.Phys.J*. 96, 97, 98, 99, 100

Tumino, A. *et al.* (2007). *Phys.Rev.Lett*, **98**, 252502. 99, 101, 103

Typel, S. & Baur, G. (2003). *Ann.Phys.*, **305**, 228. 89

Typel, S. & Wolter, H. (2000). *Few-Body Syst*, **29**, 7. 88, 90

Vauclair, S. (1988). *Apj*, **335**, 971. 42, 48

Vauclair, S. & Charbonnel, C. (1995). *A&A.*, **295**, 715. 21

Ventura, P., D'Antona, F. & Mazzitelli, I. (1999). *Astrophys.J.Lett*, **524**. 16

Wiescher, M. *et al.* (1983). *Phys.ReV. C*, **28**, 1431. 105, 136, 137

Woosley, S.E. (1990). *ApJ*, **356**, 272. 2, 15, 17

Woosley, S.E. & Weaver, T.A. (1995). *ApJS*, **101**, 181. 17

Xu, H.M., Gagliardi, C.A., Tribble, R.E., Mukhamendzhanov, A. & Timofeyuk, N.K. (1994). *Phys.Rev.Lett.*, **73**, 2027. 80

Youn, M., Chung, H.T., Kim, J.C. & Bhang, H.C. (1991). *Nucl.Phys.A*, **533**, 321. 137, 138

Zadro, M. *et al.* (1989). *Phys.ReV C*, **40**, 181. 96, 97, 98, 107, 108, 129, 145

Zahn, J.P. (1992). *A&A*, **265**, 115. 48